

# A Novel Z-Spectrum MRI For The Detection Of Brown And Browning Adipose Tissue

By

Alessandro M. Scotti

THESIS

Submitted as partial fulfilment of the requirements  
for the degree of Doctor of Philosophy in Bioengineering  
in the Graduate College of the  
University of Illinois at Chicago, 2021

Chicago, Illinois

## Defense Committee:

Prof. Thomas J. Royston, Chair, Bioengineering and Mechanical Engineering

Prof. Kejia Cai, Advisor, Bioengineering and Radiology

Prof. Chong Wee Liew, Physiology and Biophysics

Prof. Dieter Klatt, Bioengineering

Prof. Winnie Mar, Radiology

Prof. Weiguo Li, Research Resources Center and Bioengineering

To my wife, who will never read this

## CONTRIBUTION OF AUTHORS

Chapter 3 represents a published manuscript (Scotti A, Tain RW, Li W, Gil V, Liew CW, Cai K. Mapping brown adipose tissue based on fat water fraction provided by Z-spectral imaging. *J Magn Reson Imaging*. 2018 Jun;47(6):1527-1533.) for which I was the primary author and major driver of the research. The other authors assisted me in the data collection and discussion of the results. My research mentor, Dr. Cai, contributed to the design of the project and review of the manuscript.

Chapter 4 represents a published manuscript (Li L, Scotti A, Fang J, Yin L, Xiong T, He W, Qin Y, Liew C, Khayat N, Zhu W, Cai K. Characterization of brown adipose tissue (BAT) in polycystic ovary syndrome (PCOS) patients by Z-Spectral Imaging (ZSI). *Eur J Radiol*. 2020 Feb; 123:108777.) for which I was the second author and one of the principal driver of the research. I analyzed the data, generated the Figures 4.1, 4.2, 4.4 and played a large role in the writing of the manuscript along with the first author Li Li and my research mentor, Dr. Cai. My work was critical to the conclusions of this manuscript because I provided the technical expertise on the data processing and the interpretation of the results.

## TABLE OF CONTENTS

Contribution of Authors .....	iii
List of Figures .....	vii
List of Abbreviations .....	viii
Summary .....	ix
1. Introduction .....	1
1.1 Background and motivation.....	1
1.2 Hypothesis and dissertation objectives .....	2
Aim 1. ....	2
Aim 2. ....	3
1.3 Significance .....	4
1.4 Innovation .....	7
1.5 Dissertation outline.....	8
Bibliography .....	10
2. Advanced Magnetic Resonance Imaging .....	22
2.1 MRI in fat.....	22
2.1.1 Artifacts .....	23
2.1.2 Fat suppression .....	25
2.1.3 Selective excitation .....	27
2.1.4 Water-fat separation .....	29
2.3 MR thermometry .....	31
2.3.1 Relaxation times.....	31
2.3.2 Diffusion MRI .....	34
2.3.3 Proton resonance frequency shift (PRFS) .....	35
2.3.4 MR Thermometry in fat .....	37
2.4 MRI in brown adipose tissue.....	38
2.4.1 Water-fat composition.....	38
2.4.2 Microstructure .....	40
2.4.3 Perfusion .....	42
2.4.4 Thermogenesis.....	44
2.5 Z-Spectrum MR imaging.....	45
Bibliography .....	49

3.	Mapping Brown Adipose Tissue Based on Fat Water Fraction Provided by Z-Spectral Imaging.....	63
3.1	Background and Introduction .....	63
3.2	Materials and Methods.....	65
3.2.1	<i>Ex vivo</i> studies .....	65
3.2.2	<i>In vivo</i> mouse study .....	66
3.2.3	<i>In vivo</i> human study .....	66
3.2.4	Image processing .....	67
3.2.5	Statistical analysis .....	68
3.3	Results.....	68
3.4	Discussion.....	72
3.5	Summary .....	75
	Bibliography .....	77
4.	Characterization of brown adipose tissue (BAT) in polycystic ovary syndrome (PCOS) patients by Z-Spectrum Imaging (ZSI) .....	80
4.1	Introduction .....	80
4.2.	Materials and methods.....	81
4.2.1.	Subjects.....	81
4.2.2.	Imaging protocols .....	82
4.2.3	Image processing .....	83
4.2.4.	Statistical analysis .....	84
4.3	Results.....	84
4.3.1	The correlation between BAT <sub>f</sub> , FWF(BAT) and BMI.....	86
4.3.2.	Comparison of group BAT <sub>f</sub> and FWF(BAT).....	87
4.4	Discussion.....	89
4.5	Summary .....	91
	Bibliography .....	93
5.	Z-Spectrum Imaging can detect adipose tissue activation through changes in FWF .....	96
5.1	Background and introduction .....	96
5.2	Materials and methods.....	97
5.2.1	MRI protocol .....	97
5.2.2	Image processing .....	99
5.3	Results.....	99
5.4	Discussion.....	102

5.5 Summary .....	105
Bibliography .....	106
6. Z-spectrum imaging to measure temperature .....	111
6.1 Introduction .....	111
6.2 Materials and methods .....	112
6.2.1 Z-spectrum for temperature .....	112
6.2.2 Binomial preparation pulse .....	114
6.2.3 In vitro experiments .....	116
6.2.4 Image processing .....	117
6.3 Results .....	118
6.3.1 Excitation profile .....	118
6.3.2 Phantoms at varying temperature .....	119
6.4 Discussion .....	121
6.5 Summary .....	123
Bibliography .....	124
7. Z-spectrum measurement of temperature in vivo .....	127
7.1 Introduction .....	127
7.2 Materials and methods .....	128
7.3 Results .....	130
7.4 Discussion .....	133
7.5 Summary .....	136
Bibliography .....	137
8. Conclusion .....	139
8.1 Summary .....	139
8.2 Contributions to the field .....	141
8.3 Future works .....	142
Appendix .....	144
Vita .....	146

## LIST OF FIGURES

Figure 1-1 Types of adipose cells. ....	5
Figure 2-1 NMR spectrum of triglyceride. ....	22
Figure 2-2 Chemical shift artifact. ....	24
Figure 2-3 Signal evolution after an inversion pulse for different tissues. ....	27
Figure 2-4 Scheme of the basic water excitation sequence. ....	28
Figure 2-5 Z-spectrum MR imaging. ....	48
Figure 3-1 ZSI processing. ....	67
Figure 3-2 ZSI results from extracted mouse tissues. ....	69
Figure 3-3 FWF calibration in phantom containing a mix of peanut oil and water. ....	69
Figure 3-4 In vivo FWF heatmaps. ....	70
Figure 3-5 FWF in human subjects. ....	71
Figure 4-1 Z-Spectral imaging data. ....	85
Figure 4-2 FWF analysis. ....	86
Figure 4-3 Correlations between ZSI parameters and BMI. ....	87
Figure 4-4 FWF segmentation. ....	88
Figure 4-5 Comparisons of group averages. ....	88
Figure 5-1 Coronal view of mouse body. ....	98
Figure 5-2 FWF colormaps. ....	100
Figure 5-3 FWF trends. ....	101
Figure 5-4 Volume trends. ....	101
Figure 6-1 Z-spectra from brown adipose tissue at different temperatures. ....	113
Figure 6-2 Scheme of the magnetization vector traveling during the binomial pulse. ....	115
Figure 6-3 Scheme of the binomial-ZSI sequence. ....	116
Figure 6-4 Excitation profile of binomial ZSI. ....	118
Figure 6-5 Excitation profile of binomial ZSI with square pulses. ....	119
Figure 6-6 Signal modulation over frequency offsets at different temperatures. ....	119
Figure 6-7 Temperature change in PBS phantom as measured by binomial-ZSI. ....	120
Figure 6-8 Temperature changes in whipped cream. ....	120
Figure 6-9 Correlation between ZSI and GRE results. ....	121
Figure 7-2 Example of binomial Z-spectra. ....	130
Figure 7-1 Surface measurement from IR thermal camera. ....	130
Figure 7-3 ZSI temperature over time. ....	131
Figure 7-4 PRFS maps from first mouse. ....	131
Figure 7-6 PRFS maps from the third mouse. ....	132
Figure 7-5 PRFS maps from the second mouse. ....	132
Figure 7-7 Correlations between GRE and ZSI. ....	132
Figure 7-8 Comparison between ZSI and T1 mapping. ....	133

## LIST OF ABBREVIATIONS

ADC	Apparent Diffusion Coefficient
BAT	Brown Adipose Tissue
BOLD	Blood Oxygenation Level Dependent
CEST	Chemical Exchange Saturation Transfer
DWI	Diffusion-Weighted Imaging
EPI	Echo Planar Imaging
FOV	Field-of-View
FWF	Fat-Water Fraction
FSE	Fast Spin Echo
GRE	Gradient Recalled Echo
MRI	Magnetic Resonance Imaging
MT	Magnetization Transfer
NMR	Nuclear Magnetic Resonance
NOE	Nuclear Overhauser Enhancement
PET	Positron Emission Tomography
PRFS	Proton Resonance Frequency Shift
RF	Radio Frequency
SNR	Signal-to-Noise Ratio
TE	Echo Time
TI	Inversion Time
TR	Repetition Time
WAT	White Adipose Tissue
ZSI	Z-Spectrum Imaging

## SUMMARY

Brown adipose tissue (BAT) is one of the brightest hopes in the fight against the obesity epidemic. This peculiar subtype of fat tissue, in fact, when activated in response to cold exposure, breaks down triglycerides and glucose and dissipates the chemical energy into heat (“nonshivering thermogenesis”), therefore increasing energy expenditure and reducing the lipid buildup. Key to the understanding and management of BAT is the establishment of a noninvasive imaging method to unbiasedly detect and monitor brown and browning adipose tissue. The current imaging approaches are either invasive or lack a comprehensive capability to assess the structural and functional aspects of the tissue. Z-Spectrum MR Imaging (ZSI) can bridge this gap. In this dissertation, it is presented how ZSI can produce both structural and functional contrasts, which can be used to study brown and browning adipose tissue.

In the first Aim, it is shown how ZSI can measure fat water fraction and how such measurement can be used to characterize BAT. The ZSI technique, in fact, produces a spectrum from every image pixel, where the largest dips in signal reflect the direct saturation of water and fat protons. By fitting the Z-spectrum it is possible to extract the relative contribution to the overall signal, summarized in the fat water fraction. After calibrating the FWF metric with an oil and water mixture phantom, it was validated in specimens, mice and human subjects. FWF values clearly differentiated WAT, BAT, and lean tissues. FWF maps of human subjects showed the same FWF distribution as a commercial Dixon’s sequence, while displaying no fat-water swapping artifact in regions of high field inhomogeneity.

The technique was then tested in a clinically relevant scenario. It has been reported that polycystic ovary syndrome (PCOS) patients might have reduced BAT functionality. We therefore used ZSI to characterize brown adipose tissue in PCOS compared to healthy subjects. In summary, subjects with PCOS and higher BMI showed less area identified as BAT and increased FWF within such area, indicating relatively higher level of metabolically passive WAT infiltration in the depot and relatively reduced metabolism. This

result shows that ZSI can capture differences potentially instrumental to monitor treatment responses in PCOS therapies.

It was then demonstrated the efficacy of Z-spectrum MRI in detecting adipose tissue activation through changes in FWF. A transgenic mouse model, TripBr2-KO, was treated with an adrenergic drug to stimulate fat activation. Mice were studied for two weeks by ZSI and compared to saline-treated wild types. Results showed that FWF was significantly lower over time in the treated group compared to the controls, suggesting that lipid consumption, associated with adipose tissue activation, has occurred. The successful detection, confirmed by a reduction in the depot size, was found both in perirenal brown fat and in subcutaneous white fat, albeit following different temporal patterns, reflective of the different activation potential of the depots.

After demonstrating how the FWF contrast can characterize BAT mass and function, it was the aim in this thesis to show how ZSI can produce a marker of BAT very own thermogenesis. Here was then proposed a new sequence based on the ZSI platform, where the preparatory RF saturation pulse is substituted by a binomial pulse, the Jump-Return. The effect of the paired hard pulses is to refocus the saturated magnetization as a function of chemical shift. The resulting signal oscillates as a sine function of the offset. When the temperature changes, the proton resonance frequency shift effect (PRFS) assures a shift of the entire curve. The proof of concept was carried out in PBS solution exposed to hot air flow. Then, the technique was tested on a whipped cream phantom, used as a proxy for biological fatty tissue. The temperature measurement was successful and correlated well with the one from the electrode sensor probe inserted in the phantom. Being independent on phase artifacts and capable of fine thermal sensitivity, the technique is ideal for the study of thermogenesis.

Finally, the feasibility of the binomial-ZSI technique implementation *in vivo* was assessed. The protocol was tested in healthy mice undergoing thermal challenge under anesthesia. Hind legs muscles and inguinal

fat depots were imaged. Binomial-ZSI provided a reliable measurement of the temperature change across the field of view with high resolution and high sensitivity. Results were in agreement with the nominal temperature set on the scanner bore and with the temperature measured in muscles by standard MRI methods, in both muscle and fat.

These studies, taken together, show how Z-spectrum Imaging is capable of producing varied contrasts for a comprehensive characterization of brown and browning adipose tissue.

## 1. INTRODUCTION

### 1.1 Background and motivation

Brown adipose tissue (BAT) is one of the brightest hopes in the fight against the obesity epidemic. This peculiar subtype of fat tissue, in fact, when activated in response to cold exposure, breaks down triglycerides and glucose and dissipates the chemical energy into heat (“nonshivering thermogenesis”), therefore increasing energy expenditure and reducing the lipid buildup (1-5). Both preclinical and clinical studies have shown that BAT can protect against obesity, insulin resistance and other metabolic diseases (6-9). Moreover, it was discovered that cells in the conventional white adipose tissue (WAT) depots can also be converted into brown-like adipocytes and be activated, potentially extending the energy expenditure. The controlled stimulation of such “browning” process is now considered by many as one of the most promising strategies to treat obesity (10-16).

However, despite the early enthusiasm, a clear picture of brown fat potential has not yet been clearly delivered. It is true that many reviews hinted to a unified description, but these are chiefly focused on the cellular characteristics, while the complexity of the macroscopic phenotype remains. Different depots show different composition, activation susceptibility and timing: a one-fits-all description is insufficient (17-19). At the same time, the apparent complexity may have been accentuated by the variability in the strategies adopted for the investigation. Even after the community’s effort to standardize the approaches to study BAT, the fundamental limits of the conventional techniques hinder a conclusive analyses (20-35). What is missing and dearly needed is a noninvasive imaging method to unbiasedly detect and monitor brown and browning adipose tissue.

Currently,  $^{18}\text{F}$ -FDG PET/CT is the gold standard to detect BAT activity and Dixon MRI to measure its mass, based respectively on the measurement of high glucose uptake and low fat-water fraction (FWF).

However, not only they both carry physical and technical limitations, but also lack the power to combine the metabolic and the structural information: PET can only measure adipose tissue activity, and Dixon only BAT mass, thus they produce partial and often confounding results (18-19, 28, 36-43).

Z-Spectrum MR Imaging (ZSI) could bridge such gap. This technique, based on the acquisition of a set of MR images following a frequency-varying saturation pulse, is sensitive to the direct saturation of water and fat signals. The combination of these signals makes the FWF, which can be used to identify BAT mass at rest (44). Chronic changes in FWF can be used instead as markers of tissue activation. In addition to that, ZSI can be adapted to measure the temperature-dependent water frequency shift, triggered by the active thermogenic fat. We therefore aimed to show that ZSI can grasp both structural and functional signatures, that can then be used to detect brown and browning adipose tissue, with no radiation concerns, at high resolution and easy clinical implementation.

## 1.2 Hypothesis and dissertation objectives

We hypothesize that Z-Spectrum MR Imaging (ZSI) can bridge the imaging technical gap by measuring both structural and metabolic contrasts that can be then used to detect BAT and WAT browning.

We propose to test the hypothesis by completing two specific aims, directed at demonstrating the imaging contrasts that can be used to measure brown fat at rest (**Aim 1**) and after activation (**Aim 2**).

**Aim 1.** To demonstrate the capacity of ZSI to provide structural contrast to characterize BAT and WAT at rest.

**Sub-aim 1.1.** (Chapter 3) To introduce the biomarker FWF as extracted by the direct saturation of water and fat protons in ZSI data. The fat water fraction will be used to differentiate brown

and conventional white adipose tissues in phantoms, healthy mice and human subjects, based on their different cellular composition.

**Sub-aim 1.2.** (Chapter 4) The technique will then be tested in the clinical research context. ZSI will be applied to the characterization of BAT features in Polycystic Ovarian Syndrome (PCOS) patients. Parameters derived from the FWF will differentiate the patient cohort from healthy control group and correlate with BMI as a surrogate of fat content.

**Aim 2.** To demonstrate the capacity of ZSI to provide functional contrasts to measure adipose tissue activation and browning. Such contrasts consist in structural change in FWF and functional change in temperature.

**Sub-Aim 2.1** (Chapter 5) To detect fat activation by measuring changes in FWF. Detection of fat chronic activation will be tested on a mouse model treated daily with a  $\beta$ 3-adrenergic receptor agonist and imaged over time by ZSI. Differences in FWF compared to a control group will identify the structural signature of fat activation.

**Sub Aim 2.2** (Chapter 6) To develop temperature-sensitive ZSI aimed at detecting adipose tissue thermogenesis. ZSI will be modified to measure subtle frequency shifts caused by changes in local temperature. The technique's proof of concept will be carried out on phantom of fatty tissue exposed to varying temperature.

**Sub-Aim 2.3** (Chapter 7) To measure changes in temperature by ZSI *in vivo*. The validation of the technique will be carried out in the lean and fatty tissues of healthy mice exposed to heating challenges.

### 1.3 Significance

The focus of this dissertation is the development of a noninvasive radiological method to study fat.

With 2 billion people projected to be overweight by 2030 and a staggering 20% of the US annual medical expense dedicated to the obesity epidemic and its related disorders (45-47), the development of new diagnostic and therapeutic approaches for obesity and metabolic disease has become an “urgent priority” (48). Current treatments either require intensive lifestyle modifications, achieving only transient success (49), or are associated with side effects (50-51). Fortunately, there is something that can limit such a vast spreading of fat; another, unsuspected agent: fat itself.

A fat that burns fat. Brown adipose tissue is a fat type that can convert the chemical energy from the breakdown of triglycerides and glucose into heat (1-4). In other words, when activated by exposure to cold, BAT uses lipids and glucose as fuel to warm up the body (the nonshivering thermogenesis process) (6-8). A decade of research has revealed BAT’s potential clinical benefits: active BAT reduces lipid buildup and increases energy expenditure (6); it enhances glucose uptake and insulin signaling (7-8); it alleviates inflammation and oxidative stress (9-10). Even more fascinating is the discovery that conventional white adipose tissue depots can also manifest thermogenic activation: the *browning* of WAT (12-14). The discovery elicited the hope that browning of widespread WAT could severely affect energy balance in obese subjects (12-14).

However, the elusive nature and marked variability of adipose tissue activation hinder the assessment of browning’s potential (20-35). In fact, all studies of treatment feasibility and efficacy rely, first of all, on a solid and comprehensive method for brown fat *detection*. The goal of this study is therefore to provide a new mean to address the problem, that is, a diagnostic technique to identify and monitor brown and browning adipose tissue in vivo.

Currently,  $^{18}\text{F}$ -FDG PET/CT is the most-commonly used imaging method for BAT, thanks to its hallmark increase in glucose uptake when stimulated (17-18, 28, 36-42). For the same reason, however, PET is inherently sensitive to active tissue only: it cannot detect BAT at rest and might underestimate its total mass (11, 28, 41). Moreover, radiation exposure with PET/CT imaging does not allow for its use in longitudinal studies of treatment efficacy (24). On the other hand, MRI provides the flexibility, high resolution, and non-ionizing benefits that PET/CT is lacking. Dixon multi-echo MRI, in particular, has an established track record for the study of fat and can differentiate BAT from WAT based on the fat-water fraction (15, 19, 43), since brown adipocytes are more hydrated and have a reduced FWF than white cells.

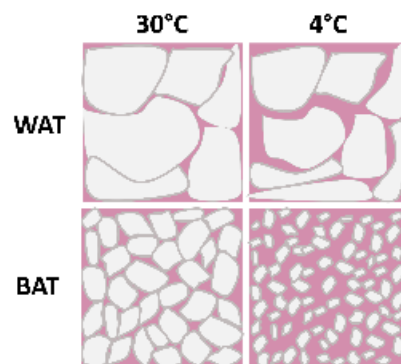


Figure 1-1 Types of adipose cells.

White adipocytes contain a single large lipid droplet and are mostly devoted to energy storage and endocrinal function. Brown cells are multilocular, with small lipid droplets and a high density of protein UCP1-positive large mitochondria immersed in the cytoplasm. When stimulated by cold or adrenergic drugs, BAT (and in some conditions, also WAT) is activated and consumes lipids and glucose to fuel the nonshivering thermogenesis.

Dixon MRI, however, suffers from phase-related artifacts that misrepresent the fat content. In addition, although indicative of BAT mass based on its cellular structure, it cannot directly measure metabolic activation. Indeed, both aforementioned techniques (and others, more advanced but less viable (52-56)) cannot provide both functional and structural information simultaneously, but rather only give partial evidences. This translates into identification mismatches and some relevant clinical gaps: is lipid content a predictor of thermogenesis? Do other factors (e.g. the depot sympathetic innervation) play a bigger role in activation (57-59)? Can the risk of obesity or the patient-specific resistance to treatment be assessed

on the basis of quantitative BAT biomarkers (18-19, 28, 39-40, 60)? These and other questions might remain unanswered without a comprehensive imaging method.

The ZSI technique consists on acquiring a set of MR images after applying a saturation RF pulse at different frequency offsets. The contrast induced in each image depends on the saturated offset, therefore a spectrum can be derived from the series, reflecting the most abundant species in the voxel (for most tissues, mainly water). Although widely used in some fields (e.g. CEST MRI (44, 61-68)), the technique has never been directed to fat imaging specifically. In this project, it is exploited the direct saturation of the protons from water and fat, proportional to their relative concentration, which is captured into the FWF as a marker of adipose content in the tissue (44). In addition, by exploiting the known effect of proton resonance frequency shifting (PRFS) (69-73) when the tissue gets warmer, a modified ZSI can also become sensitive to temperature. In other words, on one hand ZSI can detect the cellular structure of any types of fat at rest through the FWF, and on the other, changes induced by thermogenic activation can be seen through both structural (change in FWF) and metabolic (change in temperature) contrasts. These markers together may describe both mass and function, and may measure fat at rest as well as in the active state.

*We therefore aim at demonstrating the capacity of Z-spectrum MRI to reveal these two types of contrast.*

Successful accomplishment of the aims will launch ZSI as a high-resolution, non-radiative and endogenous technique for comprehensive adipose tissue imaging. With this tool, it will be possible to measure the fraction of activating fat depots and discern how patient-specific tissues respond to stimulation. Fat monitoring by ZSI will potentially guide the optimization of treatment dosage and timing, and the identification of agents (environmental, physiological (74-76), pharmaceutical (77-79)) that more efficiently and with fewer side effects produce a lasting clinical outcome. In conclusion, we expect that ZSI, by the combined structural and functional characterization of brown and browning adipose tissue, will significantly advance the clinical diagnosis and treatment of obesity and metabolic diseases.

## 1.4 Innovation

There are several innovations brought about by the development of ZSI in this project.

- 1) Firstly, ZSI is presented as a novel imaging framework where structural and metabolic contrasts can be obtained in the same session for a comprehensive BAT identification, unlike currently used techniques (28, 42). Once validated, the combined contrast will differentiate not only BAT from WAT, but also adipose tissue activation from the resting state.
- 2) The structural contrast is based on the combination of water ( $W$ ) and fat ( $F$ ) direct saturation as  $FWF=F/(F+W)$  (44). Notably, the signal from lipid resonances, historically treated as artifact in the field of CEST MRI (44, 68), is not removed, but rather exploited to produce the contrast.
- 3) The measurement of temperature, direct indicator of BAT thermogenesis, can be derived from the temperature-dependent shift of the water resonance. However, in order to detect subtle increases ( $<5^{\circ}\text{C}$ ), which are typically observed *in vivo*, a high spectral selectivity is required (70-73). By substituting the initial saturation RF pulse with a binomial  $1-\underline{1}$  pulse, (details in **Chapter 7**), the resulting signal will vary as a sine function of the frequency offset (80-83). The temperature will then be measured from the shift of the curve, and the fine spectral periodicity of the sine function will allow the measurement with high thermal sensitivity ( $<1^{\circ}\text{C}$ ).
- 4) Finally, the simultaneous presence of fat and water in the voxel produces an ambiguity in the phase component of the MRI signal, which can often lead to artifacts in MRI methods that conventionally depend on the phase information, either for the structural (Dixon) and the metabolic (PRFS) contrasts. ZSI relies solely on magnitude MR images and is therefore inherently immune to such artifacts.

## 1.5 Dissertation outline

In the first chapter, the research goal has been introduced. After describing the context of the clinical problem - the obesity epidemic - the target of the research efforts - the brown adipose tissue – has been presented. The research gap consists in the technical shortcomings of the current approaches for imaging brown and browning adipose tissue. The hypothesis of the dissertation is that a new technique, Z-spectrum MRI, can fill the gaps left by the current techniques, by providing diverse contrasts based on both mass and activity and thus a more comprehensive analysis of thermogenic fat. The objective is therefore to show how these contrasts can be obtained, and the specific research strategy follows.

In the second chapter, it is presented a review of the state of the art for those MRI methods concerning the aims of the dissertation. The goal is to set the background of the MRI research up to date, its accomplishment and where it falls short, so to illuminate the relevance of the innovations brought about in this work. The first part of the chapter will be focused on fat imaging, the second on MRI thermometry, the third more specifically on BAT imaging. At the end of the chapter, the Z-spectrum imaging technique is described in detail.

In the third chapter, it is shown how Z-spectrum MRI can measure fat water fraction to differentiate brown and white adipose tissue at rest. The proof of concept is presented, and the technique tested in *ex vivo* phantoms and healthy mice. The technique is then tested on subjects and a comparison to commercial Dixon sequence is offered.

In the fourth chapter, the results from the previous chapter are tested in a clinical research context. PCOS patients are studied by ZSI and the imaging features of BAT at rest are compared to a control group. The objective here is to show how FWF measured by ZSI can provide clinically relevant biomarkers in a metabolic disease.

In the fifth chapter, the measurement of FWF from ZSI is used no longer to assess BAT at rest, but its activation. A transgenic mouse model is chronically stimulated with an activating drug for two weeks and compared to a control group. The aim is to unveil changes in the FWF as markers of a prolonged thermogenic activation in brown and browning white adipose tissue depots.

In the sixth chapter, a modification is implemented on the ZSI technique, to make it sensitive to changes in temperature. The rationale is that by measuring temperature, a unique marker of thermogenesis, ZSI will be equipped for a comprehensive analysis of brown and browning fat. The theoretical framework for the MRI sequence is described and tested on liquid phantoms.

In the seventh chapter, the temperature-sensitive MRI is tested *in vivo*. An experiment is designed where thermal changes occur in the tissues of living mice, and ZSI is used to assess such changes and compare them to conventional measuring methods.

Finally, the last chapter provides a summary of the key results, the original contributions of the thesis, and possible future research directions.

## Bibliography

1. Tam CS, Lecoultré V, Ravussin E. Brown adipose tissue: mechanisms and potential therapeutic targets. *Circulation*. 2012;125(22):2782-91. doi: 10.1161/CIRCULATIONAHA.111.042929. PubMed PMID: 22665886.
2. Kang JG, Park CY. Anti-Obesity Drugs: A Review about Their Effects and Safety. *Diabetes Metab J*. 2012;36(1):13-25. doi: 10.4093/dmj.2012.36.1.13. PubMed PMID: 22363917; PMCID: PMC3283822.
3. Rodgers RJ, Tschöp MH, Wilding JP. Anti-obesity drugs: past, present and future. *Dis Model Mech*. 2012;5(5):621-6. doi: 10.1242/dmm.009621. PubMed PMID: 22915024; PMCID: PMC3424459.
4. Cypess AM, Lehman S, Williams G, Tal I, Rodman D, Goldfine AB, Kuo FC, Palmer EL, Tseng YH, Doria A, Kolodny GM, Kahn CR. Identification and importance of brown adipose tissue in adult humans. *N Engl J Med*. 2009;360(15):1509-17. doi: 10.1056/NEJMoa0810780. PubMed PMID: 19357406; PMCID: PMC2859951.
5. Oelkrug R, Polymeropoulos ET, Jastroch M. Brown adipose tissue: physiological function and evolutionary significance. *J Comp Physiol B*. 2015;185(6):587-606. doi: 10.1007/s00360-015-0907-7. PubMed PMID: 25966796.
6. Vargas-Castillo A, Fuentes-Romero R, Rodríguez-López LA, Torres N, Tovar AR. Understanding the Biology of Thermogenic Fat: Is Browning A New Approach to the Treatment of Obesity? *Arch Med Res*. 2017;48(5):401-13. doi: 10.1016/j.arcmed.2017.10.002. PubMed PMID: 29102386.
7. Kisanlahti A, Glumoff T. Browning of white fat: agents and implications for beige adipose tissue to type 2 diabetes. *J Physiol Biochem*. 2018. doi: 10.1007/s13105-018-0658-5. PubMed PMID: 30506389.
8. Carrière A, Jeanson Y, Berger-Muller S, André M, Chenouard V, Arnaud E, Barreau C, Walther R,

Galinier A, Wdziekonski B, Villageois P, Louche K, Collas P, Moro C, Dani C, Villarroya F, Casteilla L. Browning of white adipose cells by intermediate metabolites: an adaptive mechanism to alleviate redox pressure. *Diabetes*. 2014;63(10):3253-65. doi: 10.2337/db13-1885. PubMed PMID: 24789919.

9. van Dam AD, Boon MR, Berbee JFP, Rensen PCN, van Harmelen V. Targeting white, brown and perivascular adipose tissue in atherosclerosis development. *Eur J Pharmacol*. 2017;816:82-92. doi: 10.1016/j.ejphar.2017.03.051. PubMed PMID: 28347739.
10. Ishibashi J, Seale P. Medicine. Beige can be slimming. *Science*. 2010;328(5982):1113-4. doi: 10.1126/science.1190816. PubMed PMID: 20448151; PMCID: PMC2907667.
11. Ong FJ, Ahmed BA, Oreskovich SM, Blondin DP, Haq T, Konyer NB, Noseworthy MD, Haman F, Carpentier AC, Morrison KM, Steinberg GR. Recent advances in the detection of brown adipose tissue in adult humans: a review. *Clin Sci (Lond)*. 2018;132(10):1039-54. doi: 10.1042/CS20170276. PubMed PMID: 29802209.
12. Young P, Arch JR, Ashwell M. Brown adipose tissue in the parametrial fat pad of the mouse. *FEBS Lett*. 1984;167(1):10-4. PubMed PMID: 6698197.
13. Himms-Hagen J, Melnyk A, Zingaretti MC, Ceresi E, Barbatelli G, Cinti S. Multilocular fat cells in WAT of CL-316243-treated rats derive directly from white adipocytes. *Am J Physiol Cell Physiol*. 2000;279(3):C670-81. doi: 10.1152/ajpcell.2000.279.3.C670. PubMed PMID: 10942717.
14. Xue B, Coulter A, Rim JS, Koza RA, Kozak LP. Transcriptional synergy and the regulation of Ucp1 during brown adipocyte induction in white fat depots. *Mol Cell Biol*. 2005;25(18):8311-22. doi: 10.1128/MCB.25.18.8311-8322.2005. PubMed PMID: 16135818; PMCID: PMC1234324.
15. Chen YC, Cypess AM, Chen YC, Palmer M, Kolodny G, Kahn CR, Kwong KK. Measurement of human brown adipose tissue volume and activity using anatomic MR imaging and functional MR imaging. *J Nucl Med*. 2013;54(9):1584-7. doi: 10.2967/jnumed.112.117275. PubMed PMID: 23868958;

PMCID: PMC4167352.

16. Wu J, Bostrom P, Sparks LM, Ye L, Choi JH, Giang AH, Khandekar M, Virtanen KA, Nuutila P, Schaart G, Huang K, Tu H, van Marken Lichtenbelt WD, Hoeks J, Enerback S, Schrauwen P, Spiegelman BM. Beige adipocytes are a distinct type of thermogenic fat cell in mouse and human. *Cell*. 2012;150(2):366-76. doi: 10.1016/j.cell.2012.05.016. PubMed PMID: 22796012; PMCID: PMC3402601.
17. Martinez-Tellez B, Nahon KJ, Sanchez-Delgado G, Abreu-Vieira G, Llamas-Elvira JM, van Velden FHP, Pereira Arias-Bouda LM, Rensen PCN, Boon MR, Ruiz JR. The impact of using BARCIST 1.0 criteria on quantification of BAT volume and activity in three independent cohorts of adults. *Sci Rep*. 2018;8(1):8567. doi: 10.1038/s41598-018-26878-4. PubMed PMID: 29867076; PMCID: PMC5986766.
18. Fueger BJ, Czernin J, Hildebrandt I, Tran C, Halpern BS, Stout D, Phelps ME, Weber WA. Impact of Animal Handling on the Results of 18 F-FDG PET Studies in Mice. *The Journal of Nuclear Medicine*. 2006:999-1007.
19. Cypess AM, Haft CR, Laughlin MR, Hu HH. Brown Fat in Humans: Consensus Points and Experimental Guidelines. *Cell Metab*. 2015;20:408-15. doi: 10.1016/j.cmet.2014.07.025.Brown.
20. Petrovic N, Walden TB, Shabalina IG, Timmons JA, Cannon B, Nedergaard J. Chronic peroxisome proliferator-activated receptor gamma (PPARgamma) activation of epididymally derived white adipocyte cultures reveals a population of thermogenically competent, UCP1-containing adipocytes molecularly distinct from classic brown adipocytes. *J Biol Chem*. 2010;285(10):7153-64. doi: 10.1074/jbc.M109.053942. PubMed PMID: 20028987; PMCID: PMC2844165.
21. Xue R, Lynes MD, Dreyfuss JM, Shamsi F, Schulz TJ, Zhang H, Huang TL, Townsend KL, Li Y, Takahashi H, Weiner LS, White AP, Lynes MS, Rubin LL, Goodyear LJ, Cypess AM, Tseng YH. Clonal analyses and gene profiling identify genetic biomarkers of the thermogenic potential of human

- brown and white preadipocytes. *Nat Med.* 2015;21(7):760-8. doi: 10.1038/nm.3881. PubMed PMID: 26076036; PMCID: PMC4496292.
22. Shinoda K, Luijten IH, Hasegawa Y, Hong H, Sonne SB, Kim M, Xue R, Chondronikola M, Cypess AM, Tseng YH, Nedergaard J, Sidossis LS, Kajimura S. Genetic and functional characterization of clonally derived adult human brown adipocytes. *Nat Med.* 2015;21(4):389-94. doi: 10.1038/nm.3819. PubMed PMID: 25774848; PMCID: PMC4427356.
  23. Nagano G, Ohno H, Oki K, Kobuke K, Shiwa T, Yoneda M, Kohno N. Activation of classical brown adipocytes in the adult human perirenal depot is highly correlated with PRDM16-EHMT1 complex expression. *Plos One.* 2015;10(3):e0122584. doi: 10.1371/journal.pone.0122584. PubMed PMID: 25812118; PMCID: PMC4374757.
  24. Hamilton G, Smith DL, Jr., Bydder M, Nayak KS, Hu HH. MR properties of brown and white adipose tissues. *J Magn Reson Imaging.* 2011;34(2):468-73. doi: 10.1002/jmri.22623. PubMed PMID: 21780237; PMCID: PMC3146031.
  25. Chi J, Wu Z, Choi CHJ, Nguyen L, Teegene S, Ackerman SE, Crane A, Marchildon F, Tessier-Lavigne M, Cohen P. Three-Dimensional Adipose Tissue Imaging Reveals Regional Variation in Beige Fat Biogenesis and PRDM16-Dependent Sympathetic Neurite Density. *Cell Metab.* 2018;27(1):226-36 e3. doi: 10.1016/j.cmet.2017.12.011. PubMed PMID: 29320703.
  26. Jankovic A, Golic I, Markelic M, Stancic A, Otasevic V, Buzadzic B, Korac A, Korac B. Two key temporally distinguishable molecular and cellular components of white adipose tissue browning during cold acclimation. *J Physiol.* 2015;593(15):3267-80. doi: 10.1113/JP270805. PubMed PMID: 26096127; PMCID: PMC4553052.
  27. Leitner BP, Weiner LS, Desir M, Kahn PA, Selen DJ, Tsang C, Kolodny GM, Cypess AM. Kinetics of human brown adipose tissue activation and deactivation. *Int J Obes (Lond).* 2018. doi: 10.1038/s41366-018-0104-3. PubMed PMID: 29795459; PMCID: PMC6252171.

28. Gerngross C, Schretter J, Klingenspor M, Schwaiger M, Fromme T. Active Brown Fat During (18)F-FDG PET/CT Imaging Defines a Patient Group with Characteristic Traits and an Increased Probability of Brown Fat Redetection. *J Nucl Med.* 2017;58(7):1104-10. doi: 10.2967/jnumed.116.183988. PubMed PMID: 28104743.
29. Kalinovich AV, de Jong JM, Cannon B, Nedergaard J. UCP1 in adipose tissues: two steps to full browning. *Biochimie.* 2017;134:127-37. doi: 10.1016/j.biochi.2017.01.007. PubMed PMID: 28109720.
30. Walden TB, Hansen IR, Timmons JA, Cannon B, Nedergaard J. Recruited vs. nonrecruited molecular signatures of brown, "brite," and white adipose tissues. *Am J Physiol Endocrinol Metab.* 2012;302(1):E19-31. doi: 10.1152/ajpendo.00249.2011. PubMed PMID: 21828341.
31. Dicker A, Cannon B, Nedergaard J. Cold acclimation-recruited nonshivering thermogenesis: the Syrian hamster is not an exception. *Am J Physiol.* 1995;269(4 Pt 2):R767-74. doi: 10.1152/ajpregu.1995.269.4.R767. PubMed PMID: 7485591.
32. Ye L, Wu J, Cohen P, Kazak L, Khandekar MJ, Jedrychowski MP, Zeng X, Gygi SP, Spiegelman BM. Fat cells directly sense temperature to activate thermogenesis. *Proc Natl Acad Sci U S A.* 2013;110(30):12480-5. doi: 10.1073/pnas.1310261110. PubMed PMID: 23818608; PMCID: PMC3725077.
33. Sharp LZ, Shinoda K, Ohno H, Scheel DW, Tomoda E, Ruiz L, Hu H, Wang L, Pavlova Z, Gilsanz V, Kajimura S. Human BAT possesses molecular signatures that resemble beige/brite cells. *Plos One.* 2012;7(11):e49452. doi: 10.1371/journal.pone.0049452. PubMed PMID: 23166672; PMCID: PMC3500293.
34. Ohno H, Shinoda K, Spiegelman BM, Kajimura S. PPARgamma agonists induce a white-to-brown fat conversion through stabilization of PRDM16 protein. *Cell Metab.* 2012;15(3):395-404. doi: 10.1016/j.cmet.2012.01.019. PubMed PMID: 22405074; PMCID: PMC3410936.

35. Barbatelli G, Murano I, Madsen L, Hao Q, Jimenez M, Kristiansen K, Giacobino JP, De Matteis R, Cinti S. The emergence of cold-induced brown adipocytes in mouse white fat depots is determined predominantly by white to brown adipocyte transdifferentiation. *Am J Physiol Endocrinol Metab*. 2010;298(6):E1244-53. doi: 10.1152/ajpendo.00600.2009. PubMed PMID: 20354155.
36. Franz D, Karampinos DC, Rummeny EJ, Souvatzoglou M, Beer AJ, Nekolla SG, Schwaiger M, Eiber M. Discrimination Between Brown and White Adipose Tissue Using a 2-Point Dixon Water–Fat Separation Method in Simultaneous PET/MRI. *The Journal of Nuclear Medicine*. 2015;56:1742-8. doi: 10.2967/jnumed.115.160770.
37. McCallister A, Zhang L, Burant A, Katz L, Branca RT. A pilot study on the correlation between fat fraction values and glucose uptake values in supraclavicular fat by simultaneous PET/MRI. *Magnetic Resonance in Medicine*. 2017;00. doi: 10.1002/mrm.26589. PubMed PMID: 28112821.
38. Gifford A, Towse TF, Walker RC, Avison MJ, Welch EB, Gifford A, Tf T, Rc W, Mj A, Eb W. Characterizing active and inactive brown adipose tissue in adult humans using PET-CT and MR imaging. *Am J Physiol Endocrinol Metab*. 2016;i:95-104. doi: 10.1152/ajpendo.00482.2015.
39. Borga M, Virtanen KA, Romu T, Dahlqvist Leinhard OP, Anders, Nuutila P, Enerbäck S. Brown Adipose Tissue in Humans : Detection and Functional Analysis Using PET ( Positron Emission Tomography ), MRI ( Magnetic Resonance Imaging ), and DECT ( Dual Energy Computed Tomography ). *Methods in Enzymology*2014. p. 141-59.
40. Bahler L, Holleman F, Booij J, Hoekstra JB, Verberne HJ. Hot heads & cool bodies: The conundrums of human brown adipose tissue (BAT) activity research. *European Journal of Internal Medicine*. 2017;40:26-9. doi: 10.1016/j.ejim.2016.12.023. PubMed PMID: 28065662.
41. Chen YI, Cypess AM, Sass CA, Brownell AL, Jokivarsi KT, Kahn CR, Kwong KK. Anatomical and functional assessment of brown adipose tissue by magnetic resonance imaging. *Obesity (Silver Spring)*. 2012;20(7):1519-26. doi: 10.1038/oby.2012.22. PubMed PMID: 22343821; PMCID:

PMC4383098.

42. Cypess AM, Haft CR, Laughlin MR, Hu HH. Brown fat in humans: consensus points and experimental guidelines. *Cell Metab.* 2014;20(3):408-15. doi: 10.1016/j.cmet.2014.07.025. PubMed PMID: 25185947; PMCID: PMC4155326.
43. Hu HH, Perkins TG, Chia JM, Gilsanz V. Characterization of human brown adipose tissue by chemical-shift water-fat MRI. *AJR Am J Roentgenol.* 2013;200(1):177-83. doi: 10.2214/AJR.12.8996. PubMed PMID: 23255760; PMCID: PMC3563704.
44. Scotti A, Tain RW, Li W, Gil V, Liew CW, Cai K. Mapping brown adipose tissue based on fat water fraction provided by Z-spectral imaging. *J Magn Reson Imaging.* 2018;47(6):1527-33. doi: 10.1002/jmri.25890. PubMed PMID: 29148120; PMCID: PMC5957768.
45. Kahn BB, Flier JS. Obesity and insulin resistance. *J Clin Invest.* 2000;106(4):473-81. doi: 10.1172/JCI10842. PubMed PMID: 10953022; PMCID: PMC380258.
46. Rueggsegger GN, Booth FW. Running from Disease: Molecular Mechanisms Associating Dopamine and Leptin Signaling in the Brain with Physical Inactivity, Obesity, and Type 2 Diabetes. *Front Endocrinol (Lausanne).* 2017;8:109. doi: 10.3389/fendo.2017.00109. PubMed PMID: 28588553; PMCID: PMC5440472.
47. Cawley J, Meyerhoefer C. The medical care costs of obesity: an instrumental variables approach. *J Health Econ.* 2012;31(1):219-30. doi: 10.1016/j.jhealeco.2011.10.003. PubMed PMID: 22094013.
48. Sampath SC, Sampath SC, Bredella MA, Cypess AM, Torriani M. Imaging of Brown Adipose Tissue: State of the Art. *Radiology.* 2016;280(1):4-19. doi: 10.1148/radiol.2016150390. PubMed PMID: 27322970; PMCID: PMC4942993.
49. Cannon B, Nedergaard J. Brown adipose tissue: function and physiological significance. *Physiol Rev.* 2004;84(1):277-359. doi: 10.1152/physrev.00015.2003. PubMed PMID: 14715917.

50. Trayhurn P. Origins and early development of the concept that brown adipose tissue thermogenesis is linked to energy balance and obesity. *Biochimie*. 2016. doi: 10.1016/j.biochi.2016.09.007.
51. Klingenspor M. Cold-induced recruitment of brown adipose tissue thermogenesis. *Exp Physiol*. 2003;88(1):141-8. PubMed PMID: 12525862.
52. Cao P, Fan SJ, Wang AM, Xie VB, Qiao Z, Brittenham GM, Wu EX. Diffusion magnetic resonance monitors intramyocellular lipid droplet size in vivo. *Magn Reson Med*. 2015;73(1):59-69. doi: 10.1002/mrm.25116. PubMed PMID: 24469956.
53. Verma SK, Nagashima K, Yaligar J, Michael N, Lee SS, Xianfeng T, Gopalan V, Sadananthan SA, Anantharaj R, Velan SS. Differentiating brown and white adipose tissues by high-resolution diffusion NMR spectroscopy. *J Lipid Res*. 2017;58(1):289-98. doi: 10.1194/jlr.D072298. PubMed PMID: 27845688; PMCID: PMC5234707.
54. Branca RT, Zhang L, Warren WS, Auerbach E, Khanna A, Degan S, Ugurbil K, Maronpot R. In vivo noninvasive detection of Brown Adipose Tissue through intermolecular zero-quantum MRI. *Plos One*. 2013;8(9):e74206. doi: 10.1371/journal.pone.0074206. PubMed PMID: 24040203; PMCID: PMC3769256.
55. Branca RT, Warren WS. In vivo brown adipose tissue detection and characterization using water-lipid intermolecular zero-quantum coherences. *Magn Reson Med*. 2011;65(2):313-9. doi: 10.1002/mrm.22622. PubMed PMID: 20939093; PMCID: PMC3021650.
56. Branca RT, McCallister A, Yuan H, Aghajanian A, Faber JE, Weimer N, Buchanan R, Floyd CS, Antonacci M, Zhang L, Burant A. Accurate quantification of brown adipose tissue mass by xenon-enhanced computed tomography. *Proc Natl Acad Sci U S A*. 2018;115(1):174-9. doi: 10.1073/pnas.1714431115. PubMed PMID: 29255046; PMCID: PMC5776810.
57. Coolbaugh CL, Damon BM, Bush E, Welch B, Towse T. Cold exposure induces dynamic,

heterogeneous alterations in human brown adipose tissue lipid content. *Sci Rep.* 2019;9:13600. <https://doi.org/10.1038/s41598-019-49936-x>.

58. Song A, Dai W, Jang MJ, Medrano L, Li Z, Zhao H, Shao M, Tan J, Li A, Ning T, Miller MM, Armstrong B, Huss JM, Zhu Y, Liu Y, Gradinaru V, Wu X, Jiang L, Scherer PE, Wang QA. Low- and high-thermogenic brown adipocyte subpopulations coexist in murine adipose tissue. *J Clin Invest.* 2020;130(1):247–257. <https://doi.org/10.1172/JCI129167>.
59. He P, Hou B, Li Y, Xu C, Ma P, Lam SM, Gil V, Yang X, Yang X, Zhang L, Shui G, Song J, Qiang G, Liew CW, Du G. Lipid Profiling Reveals Browning Heterogeneity of White Adipose Tissue by B3-Adrenergic Stimulation. *Biomolecules* 2019, 9, 444; doi:10.3390/biom9090444.
60. Chen KY, Cypess AM, Laughlin MR, Haft CR, Hu HH, Bredella MA, Enerbäck S, Kinahan PE, Lichtenbelt WvM, Lin FI, Sunderland JJ, Virtanen KA, Wahl RL. Brown Adipose Reporting Criteria in Imaging STudies (BARCIST 1.0): Recommendations for Standardized FDG-PET/CT Experiments in Humans. *Cell Metabolism.* 2016;24:210-22. doi: 10.1016/j.cmet.2016.07.014.
61. Zaiss M, Bachert P. Chemical exchange saturation transfer (CEST) and MR Z-spectroscopy in vivo: a review of theoretical approaches and methods. *Phys Med Biol.* 2013;58:221-69. doi: 10.1088/0031-9155/58/22/R221. PubMed PMID: 24201125.
62. Wu B, Warnock G, Zaiss M, Lin C, Chen M, Zhou Z, Mu L, Nanz D, Tuura R, Delso G. An overview of CEST MRI for non-MR physicists. *EJNMMI physics.* 2016;3:19. doi: 10.1186/s40658-016-0155-2. PubMed PMID: 27562024.
63. Ward KM, Balaban RS. Determination of pH using water protons and Chemical Exchange Dependent Saturation Transfer (CEST). *Magnetic Resonance in Medicine.* 2000;44:799-802. doi: 10.1002/1522-2594(200011)44:5<799::AID-MRM18>3.0.CO;2-S. PubMed PMID: 11064415.
64. Ward KM, Aletras AH, Balaban RS. A new class of contrast agents for MRI based on proton chemical exchange dependent saturation transfer (CEST). *Journal of Magnetic Resonance.*

- 2000;143:79-87. doi: 10.1006/jmre.1999.1956. PubMed PMID: 10698648.
65. Vinogradov E, Sherry AD, Lenkinski RE. CEST: From basic principles to applications, challenges and opportunities. *Journal of Magnetic Resonance*. 2013;229:155-72. doi: 10.1016/j.jmr.2012.11.024. PubMed PMID: 23273841.
  66. Van Zijl PCM, Yadav NN. Chemical exchange saturation transfer (CEST): What is in a name and what isn't? *Magnetic Resonance in Medicine*. 2011;65:927-48. doi: 10.1002/mrm.22761. PubMed PMID: 21337419.
  67. Liu G, Song X, Chan K W Y, McMahon MT. Nuts and Bolts of CEST MR imaging. *NMR Biomed*. 2013;26:810828. doi: 10.1002/nbm.2899. PubMed PMID: 4144273.
  68. Cai K, Singh A, Poptani H, Li W, Yang S, Lu Y, Hariharan H, Zhou XJ, Reddy R. CEST signal at 2ppm (CEST@2ppm) from Z-spectral fitting correlates with creatine distribution in brain tumor. *NMR Biomed*. 2015;28(1):1-8. doi: 10.1002/nbm.3216. PubMed PMID: 25295758; PMCID: PMC4257884.
  69. Parker DL, Smith V, Sheldon P, Crooks LE, Fussell L. Temperature distribution measurements in two-dimensional NMR imaging. *Medical Physics* 1983;10:321–325.
  70. Dickinson RJ, Hall AS, Hind AJ, Young IR. Measurement of changes in tissue temperature using MR imaging. *Journal of Computer Assisted Tomography* 1986;10:468–472.
  71. Kuroda K, Miki Y, Nakagawa N, Tsutsumi S, Ishihara Y, Suzuki Y, Sato K. Non-invasive temperature measurement by means of NMR parameters—use of proton chemical shift with spectral estimation technique. *Medical and Biological Engineering Computation* 1991;29:902.
  72. Rieke V, Pauly KB. MR Thermometry. *JMRI* 2008 Feb;27(2):376-90. doi: 10.1002/jmri.21265.
  73. Odéen H, Parker D. Magnetic Resonance Thermometry and Its Biological Applications - Physical Principles and Practical Considerations. *Prog Nucl Magn Reson Spectrosc*. 2019 Feb;110:34-61. doi: 10.1016/j.pnmrs.2019.01.003. Epub 2019 Jan 31.

74. Fisher FM, Kleiner S, Douris N, Fox EC, Mepani RJ, Verdeguer F, Wu J, Kharitonov A, Flier JS, Maratos-Flier E, Spiegelman BM. FGF21 regulates PGC-1alpha and browning of white adipose tissues in adaptive thermogenesis. *Genes Dev.* 2012;26(3):271-81. doi: 10.1101/gad.177857.111. PubMed PMID: 22302939; PMCID: PMC3278894.
75. Bordicchia M, Liu D, Amri EZ, Ailhaud G, Dessi-Fulgheri P, Zhang C, Takahashi N, Sarzani R, Collins S. Cardiac natriuretic peptides act via p38 MAPK to induce the brown fat thermogenic program in mouse and human adipocytes. *J Clin Invest.* 2012;122(3):1022-36. doi: 10.1172/JCI59701. PubMed PMID: 22307324; PMCID: PMC3287224.
76. Shapira SN, Seale P. Transcriptional Control of Brown and Beige Fat Development and Function. *Obesity (Silver Spring).* 2019;27(1):13-21. doi: 10.1002/oby.22334. PubMed PMID: 30569639.
77. Baskin AS, Linderman JD, Brychta RJ, McGehee S, Anflick-Chames E, Cero C, Johnson JW, O'Mara AE, Fletcher LA, Leitner BP, Duckworth CJ, Huang S, Cai H, Garraffo HM, Millo CM, Dieckmann W, Tolstikov V, Chen EY, Gao F, Narain NR, Kiebish MA, Walter PJ, Herscovitch P, Chen KY, Cypess AM. Regulation of Human Adipose Tissue Activation, Gallbladder Size, and Bile Acid Metabolism by a beta3-Adrenergic Receptor Agonist. *Diabetes.* 2018;67(10):2113-25. doi: 10.2337/db18-0462. PubMed PMID: 29980535; PMCID: PMC6152342.
78. Collins S, Cao W, Robidoux J. Learning new tricks from old dogs: beta-adrenergic receptors teach new lessons on firing up adipose tissue metabolism. *Mol Endocrinol.* 2004;18(9):2123-31. doi: 10.1210/me.2004-0193. PubMed PMID: 15243132.
79. Whittle AJ, Lopez M, Vidal-Puig A. Using brown adipose tissue to treat obesity - the central issue. *Trends Mol Med.* 2011;17(8):405-11. doi: 10.1016/j.molmed.2011.04.001. PubMed PMID: 21602104.
80. Plateau P, Gueron M. Exchangeable proton NMR without baseline distortion, using new strong pulse sequences. *J Am Chem Soc* 1982; 104: 7310-7311.

81. Hore PJ. Solvent suppression in Fourier transform nuclear magnetic resonance. *J Magn Reson* 1983; 55: 283– 300.
82. Harms SE, Flamig DP, Hesley KL, Evans WP 3rd, Cheek JH, Peters GN, Knox SM, Savino DA, Netto GJ, Wells RB, et al. Fat-suppressed three-dimensional MR imaging of the breast. *Radiographics*. 1993 Mar;13(2):247-67. doi: 10.1148/radiographics.13.2.8460218.
83. Thomasson D, Purdy D, Finn JP. Phase-modulated binomial RF pulses for fast spectrally-selective musculoskeletal imaging. *Magn Reson Med*. 1996 Apr;35(4):563-8. doi: 10.1002/mrm.1910350416.

## 2. ADVANCED MAGNETIC RESONANCE IMAGING

### 2.1 MRI in fat

Magnetic resonance gives its superb radiographic efficacy to the high abundance of water molecules inside biological tissues. Its physical mechanism in fact relies on the capacity of the atomic nuclei to interact coherently with external magnetic fields, in a way ultimately described by the resonance equation (1). The different physical and chemical environments surrounding the nuclei lead to tissue-specific qualities, including the precession frequencies, the relaxation times, flow and diffusion properties, chemical exchange, all of which ultimately conspire to form the contrast in the image. The hydrogen nucleus in the water molecules is therefore the main agent involved in the signal production, but by no means the only one. When considering biological tissue, a range of other molecules is constantly present in different quantities. While large rigid structures like proteins contribute limitedly due to their short  $T_2$  and high complexity, a relevant contribution to the signal can arise from fat (1-3). In the human body, the main source is the protons residing on the chains of triglycerides, and additional smaller sources are free fatty acids and oils, all of which manifest in MR as multiple distinguished resonances, depending on the chemical structure and the surrounding microenvironment.

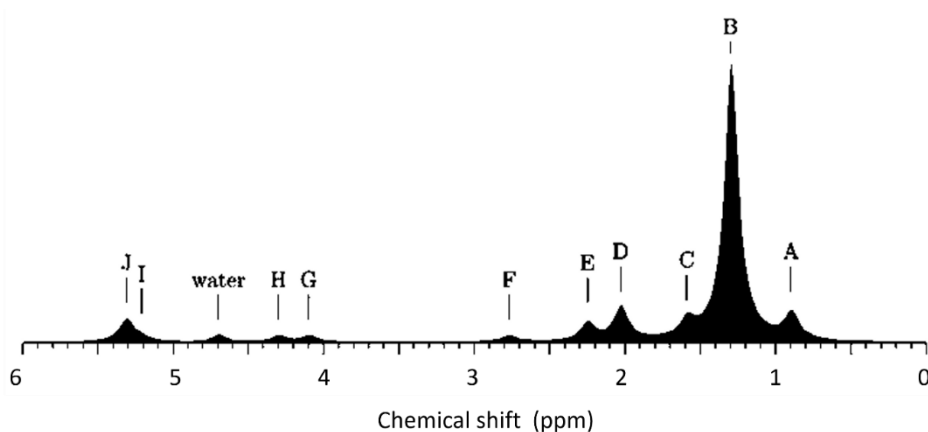


Figure 2-1 NMR spectrum of triglyceride.

Ten peaks are visible, with the main methylene peak resonating at -3.5 ppm from water, here shown conventionally at 4.7 ppm.

As is visible in Figure 2.1, the spectral profile of triglycerides spans over a range of frequencies, the prevalent being the methylene peak resonating around -3.5 ppm from the water resonance. Now, it is not uncommon in MR Imaging experiments to use receiver spectral width on the order of hundreds of KHz, which means that whatever resonates within such range, will pool into the signal, together with the water protons. At the receiver's end, there's no telling what the chemical source is and fat signal is indistinguishable from the one of water. This translates into misassignment or misplacement of signal, corrupting the final image with severe artifacts (2-5).

### 2.1.1 Artifacts

The signal from fat on conventional sequences appears brighter than water due to shorter  $T_1$ , which causes fast recovery, and to breaking of J-coupling, that cause hyperintensity in fast spin echo sequences (3-4). While the higher signal can be effectively used to localize lipid depositions characteristic in many diseases, it can also compromise the contrast in the image and the correct determination of anatomy and tissue properties.

In addition to that, by resonating at a slightly different frequency, fat protons can be misread as water's and give rise to artifacts during the image formation. In fact, during the spatial encoding priming, the effect of the gradients is to have each location experiencing a slightly different  $B_0$  field, which will cause protons to resonate at a Larmor frequency  $\omega = \gamma B$ . But other factors in the chemical and physical microenvironment, like the electronic shielding, also affect the local field. The resulting field experienced by fat protons is lower than the one experienced by water protons in the same location. Or, if we look it in another way, the fat protons will resemble water protons experiencing a lower gradient field, that is, protons located at a different position. In this way, it's impossible to know *a priori* what

species is generating the signal and from where (5-6). The result is a corruption called the chemical shift artifact and is shown in the scheme in Figure 2.2.

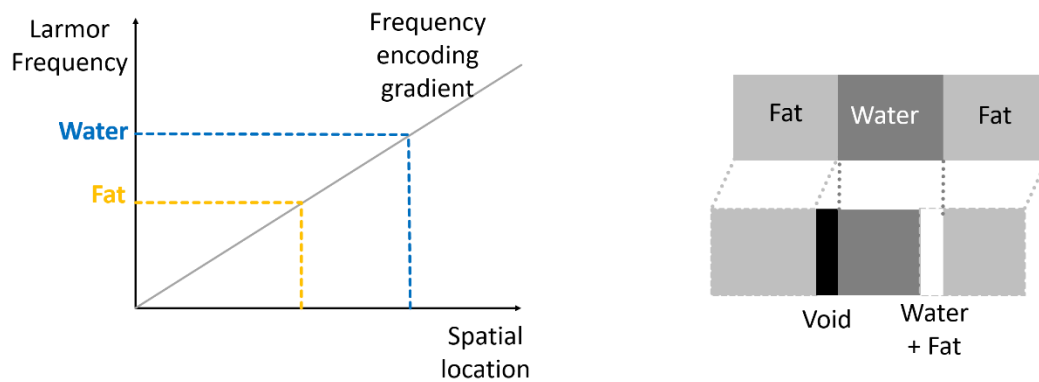


Figure 2-2 Chemical shift artifact.

By having a lower resonance frequency than water, fat can be erroneously mapped in a different position during the frequency encoding. As a result, dark and bright bands are produced at the interfaces of bordering tissues.

The artifact arises at the interface between tissues: void and bright bands will show up in the image, depending on the direction of the gradient and if fat signal is erroneously reconstructed in the same voxel where water produces signal. The extent of the artifact can be computed from the receiver bandwidth and the size of the frequency-encoding direction sampling. For instance, given a receiver bandwidth of 100 kHz and 128 pixels in the frequency encoding direction, the pixel will cover a bandwidth of  $100,000/128 = 781$  Hz. Knowing that the fat-water chemical shift difference at 9.4 T is about 1400 Hz, the extent of the artifact will be  $(1400 \text{ Hz}) \div (781 \text{ Hz/pixel}) = 1.8$  pixels. Thus, shrinking the bandwidth will increase the artifact. Generally thus high bandwidth are used when dealing with fatty tissues, at the cost of a slightly decreased signal to noise ratio (3-4, 7). The chemical-shift artifact usually appears in the frequency encoding direction, with the exception of more sophisticated acquisition schemes like the EPI, where it appears in the phase-encoding direction. This happens because the phase difference in EPI is not refocused at every echo, as in the spin echo sequences, therefore fat and water will remain mismatched in both frequency and phase. It is also worth noting that chemical shift artifacts can also appear in the slice direction, since the encoding is performed through a frequency gradient as

well. Chemical-shift artifacts in the slice direction may appear as bright or dark areas around some structures or as subtle degradation of image quality (3-4).

A second type of chemical shift artifact arises as a black contour around structures bordering with fat tissue. The dark signal is the result of destructive interference between water and fat, when both species are present in the voxel at the same time. Due to their different frequency, they evolve in the rotating frame at different speed and, at any given time the echo is sampled, that is, at any TE, they accrue different amount of phase. Over time, they will cyclically go in and out of phase with respect to each other. The final signal is going to be given by the vectorial sum of the two signals, from the maximum brightness when they are in-phase, to the minimum when they are perfectly out of phase and cancel each other. For an experiment ran at a 9.4 T field, this occurs at  $TE = (2n + 1)/1400Hz$  with  $n=1, 2, \dots$  etc. This artifact is clearly occurring in GRE sequences, but it is not present in spin echo sequences, since the  $180^\circ$  refocusing pulse brings back to phase all the pools at the center of the echo (2, 4). Given the occurrences just described, fat has historically been considered a nuisance in the way of a pristine MRI signal and several strategies to remove or isolate its signal have been developed.

### 2.1.2 Fat suppression

A first approach is to minimize the available fat magnetization before it can contribute to the signal formation. This can be performed by saturating the fat protons right before acquiring the image. The most widely used sequence to do this is the CHESS (chemical shift selective saturation), which is a simple module composed of a  $90^\circ$  pulse followed by a spoiler gradient (8-9). The key to the technique is that the pulse is applied at a narrow spectral window around the fat methylene resonance, so that only fat spins are affected. Fat magnetization is first tilted to the transverse plane, and here its phase is dispersed by the spoiler gradient. The only magnetization left in the longitudinal plane is now water's, which will be immediately imaged, before the  $T_1$  relaxation of fat can bring part of the signal back. The

CHESS technique gives its success to its simplicity and versatility, but suffers from  $B_0$  and  $B_1$  dependency.

An inhomogeneous static field will result in the saturating pulse affecting other resonances and an imperfect exciting field will deliver suboptimal saturation in some part of the field of view. The technique benefits from high field scanners, where the separation between water and fat peaks is more marked and frequency selection more at reach (8-9).

An alternative method exploits the difference in relaxation times between the species. It is the case of the STIR, or Short inversion Time Inversion Recovery (10-11). As the name suggests, it is based on the inversion recovery sequence. A  $180^\circ$  pulse non selectively inverts the spins in the voxel. After some time, the magnetization will have recovered enough to cross the null point. At that moment, the readout module is applied. The key in this method is to carefully select the waiting time  $TI$  in order to match the time it takes the fat magnetization to cross the zero point. The resulting image formed immediately after will have thus no contributions from fat. A great advantage of this technique is that it is insensitive to  $B_0$  and  $B_1$  inhomogeneity and can be generally adapted before any readout sequence. The flip side consists in long time and low SNR. In fact, due to its shorter  $T_1$ , fat will reach the crossing point while water is still at the early phase of recovery and will provide just a little magnetization to the image (10-11). It is important to stress that the inversion pulse and subsequent recovery of longitudinal magnetization alters the image contrast, introducing a heavy  $T_1$  weighting, and is therefore not recommended when studying  $T_1$ -shortening contrast agents.

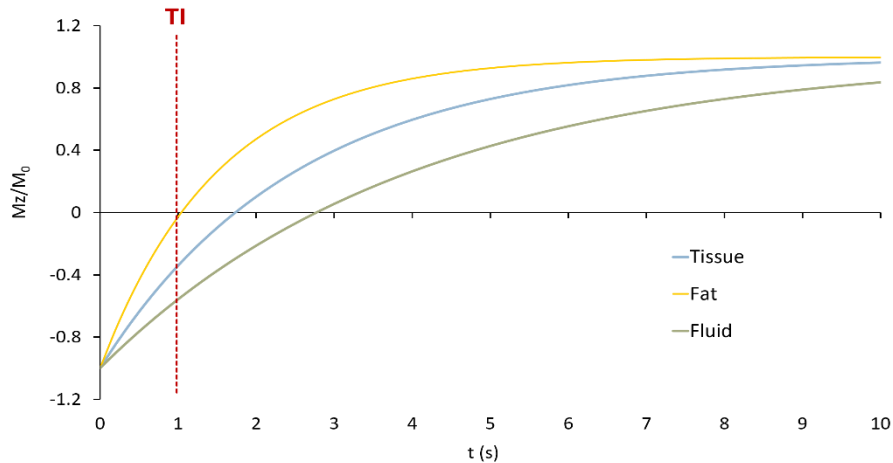


Figure 2-3 Signal evolution after an inversion pulse for different tissues.  
The STIR sequences performs fat suppression by choosing the inversion time  $TI$  equal to the nulling time of fat.

The two techniques described so far can be combined into the SPIR (Spectral Presaturation with Inversion Recovery) (12-13). Here, a spectrally selective pulse inverts the fat resonance and the magnetization of water is probed at the time  $TI$  when fat is null. This will lead to higher SNR than the parent sequence STIR, but will add the sensitivity to the fields typical of spectrally selective sequences. A variant that exploits adiabatic RF pulses for the presaturation, the SPAIR sequence, can reduce the dependency on  $B_1$  homogeneity (14).

### 2.1.3 Selective excitation

So far we've seen methods to suppress the fat signal. A different strategy is to not excite it at all, by exciting only the water signal. This can be carried out through a combination of spatial and spectral selection, so that, given a selected section, only one species is involved in the image formation. In order

to perform this selection, a category of pulse schemes, the binomial pulses, can be used (15). The most basic example is the 1-1 scheme, shown in Figure 2.4.

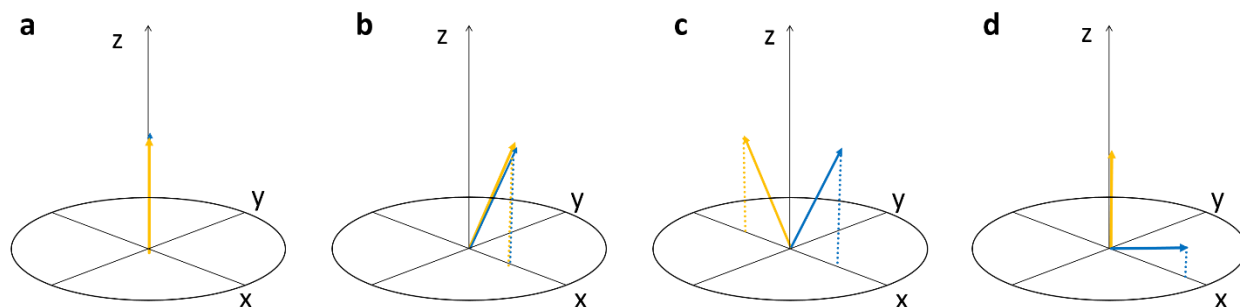


Figure 2-4 Scheme of the basic water excitation sequence.

a) At equilibrium, both fat (yellow) and water (blue) are in phase. b) After a first RF pulse is applied, the two components tilt of a flip angle specified. c) After some given time, fat will have accrued  $180^\circ$  of phase relative to water. d) After a second RF pulse is applied, fat is returned to the z-axis, while water is further tilted and will produce signal.

An RF pulse is initially applied nonselectively, irradiating both water and fat. As soon as the RF is turned off, the fat and water begin to lose phase coherence. When fat is precessing  $180^\circ$  out of phase to water, the RF pulse is applied again. The fat is at this point flipped back to the longitudinal axis and will not produce any signal, while the water experiences another excitation that is summed to the previous one.

The waiting time for the out of phase condition can be computed as  $\tau = 1/2\Delta f$  where  $\Delta f$  is the chemical shift difference between water and fat. The technique is relatively fast because there is no need for a spoiler gradient (16). It has a relatively high SNR and is insensitive to  $B_1$  heterogeneity. At higher fields, water excitation benefits from the wider spectral resolvability and shorter times between consecutive RF pulses; however, the shorter spacing implicates shorter RF pulses and stronger gradients, increasing SAR (17-18). It is also possible to use strategies with varying number of pulses and phases, with the sensitivity to  $B_0$  heterogeneities generally decreasing with sequence complexity (17). A variation of this concept is the basis for the sequence developed in Chapter 6 and 7.

#### 2.1.4 Water-fat separation

Further methods to address the simultaneous presence of fat and water in the same voxel are the chemical shift encoded methods. Of these, the Dixon technique is the most successful. Originally introduced in 1984 (19), the Dixon technique is now a powerhouse brand that include many sequence variants and is the most widely adopted noninvasive method for fat-water separation.

Since water and fat spins possess different precessing rates, their magnetization vectors rotate with respect to each other alternating in phase and out of phase states. When the spins are in phase, the total signal is proportional to their sum; when the spins are out of phase, at the opposite, the signal is proportional to the difference. In a gradient echo sequence, the appropriate choice of  $TE$  will determine the status of the relative spins phase, depending on the chemical shift. In the simplest case, the sequence consists of two repetitions at different  $TE$ s. The  $TE$  can be chosen precisely matching the in and out of phase conditions, and from a linear combination of them it's possible to derive images of pure water or pure fat, according to:

$$W = \frac{IP + OP}{2}, \quad F = \frac{IP - OP}{2} \quad (1)$$

The two-point Dixon is fast and easily implementable, but it is strongly affected by  $B_0$  inhomogeneity, as even a small shift in the fat resonance will cause an imperfect selection of the relative phase conditions (19-20). By adding more acquisitions at different  $TE$ s, the sequence gains resistance to inhomogeneity. There are now two-, three- and multi-points commercial sequences set up in scanners from all vendors for clinical routine. The key for the best results is the choice of the right  $TE$ s. In general, the longer the  $TE$ , the more robust is the fat/water separation, because the phase accrued is higher. But longer  $TE$  images suffer from low SNR and takes longer time to acquire, therefore a tradeoff must be reached. In reality, the signal behavior over time is more complex and needs more nuanced modeling.

A more realistic description of the fat profile would include multiple resonances, each one with a different chemical shift and prevalence. A general spectrum for triglycerides is shown in Figure 2.1.

The total MR signal at time  $t$  is given by:

$$S(t) = \left( W + \sum_m^N \alpha_m e^{i2\pi\Delta f_m t} \right) e^{i2\pi\varphi t} e^{-\frac{t}{T_2}} \quad (2)$$

where the coefficients  $\alpha_m$  represent the relative amplitude of the fat components and  $\Delta f_m$  their chemical shift with respect to water. The second exponential describes the phase shift due to the local magnetic field and the last exponential takes into account the relaxation. At any given  $TE$ , the signal will be a combination of all  $N$  components at a different phase. In this form, the dependency on  $B_0$  is rendered explicit. The signal models developed on this basis are mainly characterized by the number of free parameters. In general, having additional free parameters offers more degrees of freedom and allows for more accurate modeling, but also requires more samples for a more robust fit (21-22). Taking into account transverse relaxation, in particular, improves the modeling substantially with a broader range of  $TE$ s.

The most common artifacts encountered in Dixon methods are a local swapping of water and fat signal or a bleeding between two neighboring regions. The first is characterized by an abrupt transition between areas with correct and areas with incorrect assignment to water and fat signal, the second is visible as a smooth transition in signal intensity (23). In order to minimize the occurrence of these artifacts, more sophisticated reconstruction algorithms have been designed (24-25). Instead of a direct calculation of water and fat signal, Dixon methods now typically perform the separation in three steps. First, they calculate the solution for each component in the voxel, starting with an arbitrary initial value for the field  $\varphi$ . The error from this solution is then used to estimate the error on the field phase. The solution is computed again after correcting the field map and the process repeated until the field error is

below a chosen threshold. Finally, after smoothing the map, since field variation are not expected to be abrupt but continuous, the solution for water and each fat component are recalculated with the final field map. This reconstruction, that can exploit both magnitude and complex data, has proven to greatly minimize the insurgence of artifacts in tissues, even in the presence of high field inhomogeneity. Nevertheless, it is still possible that the minimization descent in the algorithm encounters local minima for the field map, producing incorrect assignment of fat and water. To overcome this occurrence, several phase regularization methods implemented into the reconstruction, like the smoothing requirements mentioned above, have been proposed (26). Building on this seminal sequences, a number of other modifications and refinement have also been brought to light (4, 27-34).

## 2.3 MR thermometry

The measurement of temperature in biological tissue is one of the most fascinating and challenging tasks for radiological techniques.

Most proton magnetic resonance parameters are temperature dependent: the resonance frequency or chemical shift, relaxation times (35-40), proton density or thermal equilibrium magnetization (41-42), and the diffusion coefficient (43-44). While the latter four parameters are interdependent, since they are obtained from the signal amplitude, the chemical shift can be derived just from the proton frequency and not from the other factors.

### 2.3.1 Relaxation times

The derivation of the analytic expression for relaxation times in the tissue from the known theory of relaxation is a hard task. Nevertheless, a working approximation sees the time  $T_1$  expressed in terms of the correlation time  $\tau_c$ , (45-46) according to:

$$\frac{1}{T_1} = \frac{2\gamma^2 B_{loc}^2}{3} \frac{\tau_c}{1 + \omega_0^2 \tau_c^2} \quad (3)$$

where  $\gamma$  is the gyromagnetic ratio,  $\omega_0$  the resonance frequency and  $B_{loc}$  the local field. This can be further reduced to:

$$\frac{1}{T_1} \propto \tau_c \quad (4)$$

From this, knowing that  $\tau_c$  is also inversely proportional to the temperature, we infer that  $T_1$  is directly proportional to temperature. This relationship has been described by:

$$T = \frac{T_1(T) - T_1(T_{ref})}{m_1} + T_{ref} \quad (5)$$

where  $m_1$  is a coefficient that varies for tissues with different macromolecular content and microstructure. For each different tissue, a different coefficient  $m_1$  has to be derived.  $T_1$  scales steeply with temperature, in fact it has been estimated that 1–3% changes can be detected per each degree Celsius in water, and even higher values in fat tissues (47-52).

Unfortunately, conventional  $T_1$  measurement sequences like inversion recovery cannot be used in applications like ablative procedures, which are usually very fast. Quicker methods have been used, like dual-TR spin echo and sequences with variable flip angle (53-54). In the latter, two or more magnitude images acquired at different flip-angles are acquired and the  $T_1$  maps determined by a linearization of the signal equation. The method is generally not sensitive to  $B_1$  field inhomogeneities but is sensitive to error in flip angle estimation. In order to avoid the long flip angles mapping procedures, a study proposed to combine the method with a fast EPI readout, and greatly accelerated the sequence (50-51, 55). Changes in  $T_1$  with temperature are reversible as long as temperature changes are contained, up to a temperature of 43 °C, in both water- and fat-based tissues.

The transverse relaxation time can also be used to study temperature. The local magnetic field varies in time due to the random thermal motions of the molecules, which results in variations in the spins' frequency, and finally in an irreversible dephasing among the spins. The relaxation is again connected to the correlation time:

$$\frac{1}{T_2} = \gamma^2 B_{loc}^2 (\tau_c + \frac{\tau_c}{1 + \omega_0^2 \tau_c^2}) \quad (6)$$

In free water, where spins are moving fast and are not restricted,  $\tau_c$  will be short and the compartment will therefore have longer  $T_2$  values than other areas where the motion of the water molecules is restricted and the molecules move slower (49). The measurement of temperature through a series of  $T_2$  maps relies again on a calibration factor and reference values:

$$T = \frac{T_2(T) - T_2(T_{ref})}{m_2} + T_{ref} \quad (7)$$

In the study on bovine fat mentioned earlier, it has been shown that different proton pools have different temperature coefficients  $m_2$ , varying few percent points from  $\text{CH}_2$  to  $\text{CH}_3$  (49).  $T_2$  rises linearly with absolute temperature in the physiological range, and in a window of changes on the order of 5–7 ms/°C (52, 57-58). Given the variability in the coefficients, in mixed areas, where water and fat have different  $m_2$ , and their relative abundance and distribution is unknown, it is not possible to measure the change in  $T_2$  accurately. As for the pulse sequences,  $T_2$ -based approaches are either based on long multiple echoes from spin echo sequences (52), or sequences that combine two-echoes with FSE readouts, which deliver an image in 15 s (57-58).  $T_2$ -based thermometry is still a very open research area and a promising one, considering its high temperature sensitivity, especially compared to the longitudinal relaxation time.

### 2.3.2 Diffusion MRI

Molecular diffusion depends on temperature according to the Stokes-Einstein formula:

$$D \approx e^{-E_a(D)/kT} \quad (8)$$

where  $D$  is the diffusion coefficient,  $T$  is the absolute tissue temperature,  $E_a$  is the activation energy for translational molecular diffusion and  $k$  is the Boltzmann constant (59-60). Temperature changes will result in viscosity and diffusion changes which can be estimated by:

$$\Delta T = T - T_{ref} = \frac{kT_{ref}^2}{E_a(D)} \frac{D - D_{ref}}{D_{ref}} \quad (9)$$

where  $D_{ref}$  is the diffusion constant measured at a reference temperature  $T_{ref}$ . In this formula  $E_a$  is considered constant on the assumption that the temperature dependence of the activation energy is small, and that also the change in temperature is small compared to the reference:  $\Delta T \ll T_{ref}$ . The sensitivity of diffusion *in vivo* to temperature changes has been shown to be relatively high. Given an activation energy of 0.2 eV at 20 °C (60), the sensitivity can reach the range of 2.0–2.5 % per degree Celsius (61-62). However, practical difficulties in its application have hindered the spread of temperature measurements using the diffusion method. In particular, the high sensitivity to both physiological and bulk patient motion have severe impact on the results (63). Physiological factors can also corrupt the temperature measurement. For instance, cell swelling in ischemia can result in diffusion increases in the same way as temperature changes (64). Also, when temperature gradients are present in the same voxel, the water resonance frequency shifts, that in turn will disperse the spin phases, which can be misinterpreted as a change due to diffusion. The effect can even be heightened by the long  $TE$  values that are adopted in diffusion imaging. It is possible to avoid this effect altogether by using spin echo pulse sequences. Despite these challenges, diffusion weighted imaging has been used consistently to monitor relative temperature change (62-66).

### 2.3.3 Proton resonance frequency shift (PRFS)

The resonance frequency of water protons in biological tissue is determined by two opposed forces: the external static magnetic field  $B_0$  and the currents induced in the electron cloud shielding the nuclei.

When the temperature rises, the increased motion of water molecules leads to the stretching of the hydrogen bonds, eventually breaking them. The unbound electrons are then freer to move and exert a stronger current in the electron cloud, therefore increasing the shielding effect from the external magnetic field on the nuclei, resulting in a lower proton resonance frequency.

A simple model can describe the thermal frequency shift. The resonance frequency is a function of the magnetic flux density  $B_0$ , the volume susceptibility  $\chi$  and electronic shielding with constant  $\sigma$ :

$$\omega(T) = \gamma B_0 (1 - \sigma(T) + \chi(T)) \quad (10)$$

It is possible to monitor changes in temperature by tracking the change in frequency respect to a reference condition:

$$\Delta\omega = \omega - \omega_r = \gamma B_0 (\sigma_r - \sigma(T) + \chi(T) - \chi_r) \quad (11)$$

Since in water the susceptibility is expected to change little with temperature, we can neglect for now the susceptibility terms and we see that the chemical shift is solely dependent on the difference in shielding. When temperature changes, the water shielding scales linearly, (6-7, 21, 67):

$$\Delta\sigma_W = \alpha\Delta T \quad (12)$$

and the chemical shift will scale accordingly:

$$\Delta\omega = \gamma B_0 (\Delta\sigma_W) = \gamma B_0 (\alpha\Delta T) \quad (13)$$

where the coefficient  $\alpha$  has been found conveniently stable across many tissues, around  $-0.01 \text{ ppm}/^\circ\text{C}$ . From the chemical shift, the change in temperature can thus be quantified and, short of a constant offset, also the absolute temperature.

Magnetic resonance spectroscopy techniques can measure the chemical shifts. In this technique, an internal resonance is selected to reference all the spectrum. Conventionally, N-acetyl aspartate is used in the brain, since its frequency isn't prone to shift. In breast experiments, lipid resonances have been used (68) and other nuclei with different resonances have been from time to time been proposed (69-70). However, the relatively long data acquisition time, the low spatial resolution and coverage make MRS quite impractical in the study of biological tissues.

After several studies proved its concept, instead, the phase mapping method grew up to be the most widely accepted for monitoring tissue temperature changes during thermal therapies (71-74). The PRF change is obtained from the voxelwise signal phase difference from gradient echo sequences at two different temperature stages (75-76):

$$\Delta T = \frac{\Delta\omega}{\alpha} = \frac{\Delta\varphi}{\gamma B_0 \alpha TE} \quad (14)$$

where  $\Delta\varphi$  is the phase difference and  $TE$  is the echo time of the acquisition.

To achieve the optimal precision in PRF shift thermometry, the phase difference signal to noise ratio should be maximized. If the tissue variables are assumed to be relatively constant during the acquisition, the signal intensity will only depend on the imaging parameters. In a GRE sequence, the phase accrues linearly with time until the signal sampling at  $TE$ , so:

$$SNR_{\Delta\varphi} \propto TE e^{-\frac{TE}{T_2^*}} \quad (15)$$

where we can see that the optimal condition is a tradeoff between long  $TE$  for larger phase accrual and short  $TE$  for minor signal loss.

Despite being the popular choice for the assessment of temperature in medical research, phase mapping is not free from many confounding factor that can corrupt the measurement. The phase difference changes with the magnetic field (77), tissue susceptibility (78), and motion (71, 79). Also, when other signals, from different pools like fat, are present in the voxel, they prevent the accurate calculation of the phase change in the water signal (80). Either these non-water signals are used as internal reference, or they surely should be suppressed. In addition, a temperature-dependent change in the susceptibility gradient between watery and fatty bordering tissues can corrupt irreversibly the temperature estimation (81).

#### 2.3.4 MR Thermometry in fat

Thermometry based on PRFS in non-watery tissues, such as in fat depots, is not widespread due to the minimal shift in the protons in fatty acids, which do not have hydrogen bonding (82). Alternatively, techniques using  $T_1$ -weighted or proton density images has been implemented (83). Methods exploiting the  $T_2$  relaxation time has been applied on swine and humans, requiring a previous signal calibration through *ex vivo* tissues (51-52). In a study on bovine fat tissue *in vitro*, the relaxation times of the major fat spectral components (methylene and terminal methyl) showed a linear correlation with temperature, albeit with different coefficients in the two components (69). Interestingly, in this study, the coefficients were similar in different specimens, therefore indicating that fat temperature could be quantified if the different components are successfully isolated.

Sequences combining variable flip angles and multiple  $TE$ s have been used to quantify the  $T_1$ -related coefficients in lipids and the frequency of water in a mixed tissue, although a formal optimization of the technique parameters is lacking (70, 84). Another technique combining PRF and  $T_1$  was proposed to

assess changes in temperature in watery and fatty tissues. The method was based on the Dixon sequence and detected signals without differentiating the chemical shift components of fat. The approach was successful and was extended to quasireal-time 3D fat and water temperature imaging during human breast tissue HIFU. The implementation, however, is not straightforward and requires a dedicated system (85-86).

## 2.4 MRI in brown adipose tissue

Several of the aforementioned techniques have been used for the study of brown and browning adipose tissue.

### 2.4.1 Water-fat composition

The protocols most often used to assess BAT morphology and to differentiate BAT from WAT are based on the quantification of water and fat relative content. In fact, BAT is more hydrated and has a reduced fat content, thus quantification of water–fat composition can be used to differentiate it from WAT.

Single-voxel proton MRS or chemical shift encoding-based water–fat MRI are the two main approaches used for this purpose. Single-voxel proton MRS can be used to quantify water and fat content within a large voxel, by resolving the different peaks and thus measuring fatty acid composition (87). MRS acquisitions, however, requires long  $TR$  to minimize  $T_1$  weighting effects, and an acquisition with multiple  $TEs$  to correct for  $T_2$  weighting effects. These long acquisition times, together with voxel misregistration due to the sensitivity to physiological motion and strong susceptibility gradients in the tissue, cause severe spectral line broadening, which ultimately hinders the correct quantification of water and fat spin components in the tissue.

Chemical shift encoding methods have become probably the most widely used for BAT detection. These techniques can quantify the lipid content, or proton density fat fraction (PDFF), defined as the proportion of mobile proton density in tissue attributable to fat (88). PDFF has been measured with excellent linearity, accuracy, and precision across different field strengths and MR manufacturers and applied for the study of liver and other organs (89-90). The technique usually combines a multi-echo gradient echo acquisition with a reconstruction strategy to separate water and fat. The measurement also takes into account some confounding factors, like  $T_1$  bias (92-93), the presence of multiple fat peaks,  $T_2^*$  decay and some phase error effects (94-95). However, there is no systematic analysis on the effect of these confounding factors for BAT. Thus, the current approaches rely on methodologies developed in the study of other tissues (1, 91). Usually complex-based methods are preferred over magnitude-based methods, thanks to their reduced sensitivity to signal model mismatches, even though they bring about a stronger chance of phase corruption (96-98). The presence of inhomogeneous time-varying magnetic field gradients can produce an incorrect field map estimation which results in the infamous water– fat swaps in the reconstruction. There is an abundance of field mapping techniques addressing such errors, by imposing a smoothness constraint on the field map estimation or by applying an *a priori* known magnetic field inhomogeneity, but a definitive solution has not been established (100-101).

A clear identification of BAT based on MRI fat fraction measurements alone is still challenging. In fact, BAT lipid content strongly depends on many physiological processes, factors like age, BMI, thermal living conditions, diet, and the variable response to acute and chronic exposure to cold or adrenergic stimulation (102-104). Furthermore, contrary to rodents, which have a large and homogeneous BAT depot such as the iBAT depot, humans have few small depots highly sparse in their composition. The greater BAT heterogeneity found in adult humans that, unlike mice, do not live under constant thermal stress, is probably the main reason for the conflicting results found in activation studies.

## 2.4.2 Microstructure

Multiple previous works have shown that BAT has shorter  $T_2^*$  than WAT, both in mice and in humans (105-108). The shorter  $T_2^*$  of BAT is due to its abundance of iron-rich mitochondria, which give to this tissue its characteristic brown color. Most of studies on the accuracy and precision of  $T_2^*$  mapping have been carried out in aqueous tissues, and little is known about the performance of  $T_2^*$  mapping in fatty tissues. A recent study showed that using a 20-multiecho gradient echo acquisition delivered a markedly decreased range of  $T_2^*$  value and standard deviation in supraclavicular and gluteal adipose tissue when compared to a shorter protocol with 6 echoes (109). This effect pointed out the variability of the results from different acquisition protocols, and the sensitivity of adipose tissue  $T_2^*$  quantification on the underlying fatty acid composition (109).

Another technique that has been proposed to detect BAT is based on intermolecular multiple quantum coherences (iMQCs) between water and fat spins. iMQCs between  $^1\text{H}$  spins residing in the molecules can be made observable by using a combination of pulses and gradients that regulate the longitudinal magnetization by breaking its spatial isotropy, and regaining the effect of long-range dipolar field interaction between those spins that interact at a given correlation distance (110-111). The long range dipolar field will cause antiphase magnetization originating from iMQCs to evolve in an observable signal. The choice of a correlation distance in the scale of the cellular size can cause the longitudinal magnetization from water and fat spins that are only a few micrometers apart create the signal, while at the same time suppressing the iMQC signal between spins that are farther from each other, which likely reside in different tissues. The great novelty of this method is the ability to probe the tissue at the cellular level, a scale that is currently inaccessible by clinical MR techniques. The protocol was applied *in vivo* to map BAT distribution in mice and rats (112-113). Since the iMQC signal intensity scales as the square of magnetization density and thus as the square of the magnetic field strength, application in clinic scanners are still limited. Also, at 3 T, the time needed to the dipolar field to refocus the signal

originating from iMQCs is several hundreds of milliseconds— much longer than the characteristic transverse relaxation times of BAT, thus further limiting the detectable signal.

Diffusion-weighted imaging can also probe tissue at the microscopic level and it's been used for the assessment of BAT microstructure. However, no significant difference was found between an obese and a healthy subjects group in the only study that assessed its water diffusion. The finding of a slightly more restricted water in the obese BAT was explained by a reduced extracellular space due to the larger adipocytes (108). DW-MRS, the combination of diffusion weighting and spectroscopy, enables one to assess the diffusion properties of both water and lipid signals, without the need for fat suppression. Through it, by applying high b-value gradients at variable diffusion times, one can detect differences in cell size (114-115). The high b-values are required because fat diffuses 100 times slower than water. A lower ADC was found in the WAT samples of rats on a high fat diet compared to those on a normal chow diet. Again, the lower ADC was linked to longer fatty acid chain lengths and more saturated fatty acids in the triglycerides. Consistently, the smaller radii found for the BAT of chow diet rats agreed with the histological findings. *In vivo*, lipid droplet size measurements in organs like leg bone marrow have also been demonstrated (114-115). However, spin dephasing due to intra-voxel motion can result in confounding signal attenuation, which in turn leads to an overestimation of fat diffusion properties (116-117). In another study in the human supraclavicular fossa, the impact of motion was reduced by referencing water to the fat peaks before fitting the ADC value (118). In this preliminary study, a more restricted diffusion behavior of the water signal in brown fat was found, which stands in contrast to the findings of the study using DWI (108, 119). Further measurements validated by histological assessment of the tissue are yet needed for a better modeling of the DW-MRS signal in BAT.

### 2.4.3 Perfusion

The sympathetic nervous system stimulation key to BAT activation typically is accompanied by an increase in tissue perfusion (120-121). In fact, during stimulation of thermogenesis, BAT vessels and capillaries are dilated to increase blood flow, while arterial–arterial shunts are used to divert blood from conventional WAT. A study using Dynamic Contrast Enhanced (DCE) MRI on the iBAT depot in rats assessed the blood flow after activation with adrenaline and found it higher than in a control group (122). Similarly, another study found three times higher uptake of contrast agent in cold-exposed rats compared to a thermoneutral control group (123). Another, more quantitative study correlated the uptake kinetics of DCE-MRI with fat content (124). The study showed an increase in tissue perfusion in both iBAT and inguinal beige fat after activation, together with a decrease in fat fraction. No study has yet used DCE-MRI in humans to study BAT. An alternative to  $T_1$ -shortening gadolinium-based contrast agents, like the one used in DCE-MRI, are superparamagnetic iron oxide nanoparticles, that shorten  $T_1$ ,  $T_2$ , and  $T_2^*$ . Monocrystalline iron oxide nanoparticles have been used to study BAT perfusion in rats after injection of a  $\beta_3$ -adrenergic receptor agonist through the change in the signal intensity in  $T_2$ -weighted images. However, a low accuracy was reported for this method (125). Alternatively, radioactively labeled superparamagnetic iron oxide nanoparticles (Triglyceride-Rich Lipoprotein (TRL)-59FESPIOs) have been tested, by embedding them into a lipoprotein layer to study the uptake of the nanoparticles by different organs, such as the liver, blood, muscle, and BAT. Cold-exposed mice showed a significant decrease of  $T_2^*$  in BAT compared to the control group, showing how lipid uptake can be an optimal target for the study of BAT metabolism (126). The BOLD effect linked to natural perfusion has been also exploited. In rodents undergoing noradrenergic stimulation, activation led to a decrease in blood oxygenation level and thus to a drop in  $T_2^*$ , and to a consequent reduction in MR signal intensity, clearly observed near the Sulzer's vein (127). In humans, whether the MR signal increases or decreases upon activation is still unclear. The same mechanism in fact leads to a change in susceptibility, which can adversary

confound the results. Specifically, a strong shift toward higher magnetic susceptibility gradients was detected during BAT activation in a mouse model after injection of a  $\beta$ 3-agonist (127).

**Table 1.** Summary of the main MR-based techniques for the study of BAT.

Technique	Information provided	Specific to BAT	Sensitive to $\Delta B_0$	Advantages	Disadvantages
<b>Chem shift encoded</b>	Fat fraction	No	Yes	High SNR, resolution; fast acquisition.	Phase artifacts
<b>T<sub>2</sub><sup>*</sup>/QSM</b>	Iron content; Perfusion	No	Yes	Fast acquisition	Low SNR, many confounding effects
<b>DCE; SPIOs</b>	Perfusion	No/Yes	Yes	High SNR	Contrast agent
<b>DW MRS</b>	Diffusion; lipid droplet size	Yes	No	Probes both water and fat; micro scale	Requires large b-values; motion; contradicting results
<b>iMQC</b>	Intracellular water-fat correlation	Yes	Yes	Micro scale; no partial volume	Low SNR, resolution; complex sequence;
<b>iZQC</b>	correlation distance/chemical shift	Yes	Yes	Micro scale; no partial volume; temperature measurement	Low SNR, resolution; complex sequence; confounded by fat distribution
<b>Xe-MRI</b>	Xe deposit in fat; chemical shift	Yes	No	Background-free; potentially both mass and activity information.	Low SNR; resolution; contrast agent; special instruments

Finally, Hyperpolarized xenon gas-enhanced MRI, a technique widely used to detect lung ventilation function in humans, has also been used to detect BAT, both in rodents and in humans (128-129). Because of the high solubility of xenon in lipids, the gas can accumulate in fat-rich tissues, like BAT, at a rate that is directly proportional to tissue perfusion and blood flow. As a result, changes in BAT blood flow can be detected as an increase in the lipid peak in Xenon MRI, after administration of the gas to the patient (129).

Notwithstanding all these methods for the study of perfusion in BAT, however, a recent study showed that increased blood flow to BAT was observed in mice regardless of the amount of thermogenic activation (128-129). Therefore, it is worth noting that measurements of changes in BAT perfusion represent a promising way to probe BAT stimulation but do not reflect thermogenic response (130).

#### 2.4.4 Thermogenesis

BAT temperature measurements represent the most direct and accurate way to detect BAT metabolic activity, which is defined by oxidation of fatty acids in order to generate heat (131). Yet, so far, non-invasive monitoring of thermogenic activity in rodents has been assessed almost entirely indirectly, by either measuring the resting energy expenditure with indirect calorimetry, by point-source temperature measurements, or by estimating the ability of animals to defend the core body temperature when exposed to cold challenge. Skin temperature measurements by infrared thermography are also used to detect BAT activation (132-133). However, these measurements are not very specific as they are influenced by other physiological responses, and suffer from a low penetration capability.

MRI has a long tradition of thermometric use. In fact, many MR parameters can be exploited for the measurement, as described in the previous paragraph. In the majority of the applications, the temperature-induced proton resonance frequency shift of water is the preferred probe (126).

Unfortunately, the technique suffer from some limitations in practice. On a standard 3T MRI system, for example, the temperature-induced shift of the water resonance resonance is only about 1 Hz/°C, compared to the much higher shift caused by varying susceptibility gradients, magnetic field drift or motion artifacts, that range in 10–50 Hz. As mentioned before, the resonance frequency of lipid protons can sometimes be used to correct for macroscopic field inhomogeneity and motion (83). But care must be taken when the intra-voxel distribution of water and fat spins and the geometry of the distribution causes large difference in the local field experienced by the two chemically different spins, which result in severe temperature errors of a few degrees Celsius (134). Therefore, even though it is still possible to use PRFS for temperature monitoring in rodents, where BAT temperature can increase by more than 5°C (135), it can be a hard task to measure the smaller temperature increase (1–2°C) expected in human BAT during cold exposure.

A fascinating possibility would be the use of iMQC to remove the effect of magnetic field inhomogeneity and motion at the microscopic level. One particular type of iMQC signal, the intermolecular zero quantum coherence (iZQC), evolves as the difference in frequency between water and fat protons, resulting in removal of some inhomogeneous broadening at the microscopic level, and possibly enabling absolute temperature measurements in the tissue (136). In practice, this is precluded by the much higher sensitivity of the water–fat iZQC frequency to the spatial distribution of water and fat tissue at the microscopic level (137).

Finally, the use of hyperpolarized  $^{129}\text{Xe}$  gas for MR thermometry measurements was demonstrated feasible in fatty tissues (188). The key to this method is the much higher temperature sensitivity ( $-0.2$  ppm/ $^{\circ}\text{C}$ ) of the chemical shift of xenon dissolved in fat, compared to the sensitivity of conventional  $^1\text{H}$  MRI ( $-0.01$  ppm/ $^{\circ}\text{C}$ ). This methodology was demonstrated in both rodents and humans (128-129, 138), and the ability to directly measure absolute temperature in fat tissues was also demonstrated (128). In fact, this can be done by using the lipid resonance, which is coupled with the dissolved xenon, as an internal reference to remove the effect of magnetic susceptibility gradients. This methodology is to date the only MR-based approach that delivered reliable results, but requires injection of contrast agent and a dedicated instrumentation and analysis, not currently available at most laboratories.

## 2.5 Z-Spectrum MR imaging

This dissertation focuses on the implementation of Z-spectrum MR imaging in the study of fat. In the following, the basic principles of the technique and the relevance of its use in medical research are covered.

The technique aims to show the evolution of the longitudinal magnetization (the z-magnetization) as a function of the frequency offset. Since the water is by far the dominant molecular species present in the tissue, it is customary to reference the spectrum to the water resonance, as opposed to what happens in conventional NMR, where water resonates at 4.7 ppm referenced to tetramethylsilane (TMS,  $\text{Si}(\text{CH}_3)_4$ ).

At the beginning of the century, the Z-spectrum MRI found great relevance in the study of tissue metabolism thanks to the introduction of the CEST effect in the MRI arena. Chemical exchange saturation transfer (CEST) is the mechanism through which metabolites that exchange protons with the bulk water can produce a visible MRI signal (139). The sequence makes use of a long saturation pulse irradiated at the resonance frequency of a given metabolite. The protons just saturated by the RF will depart from the molecule and attach themselves to the water molecules surrounding the metabolite, which also will have donated a proton in the exchange. This chemical process is continuous and sustained throughout the duration of the long RF pulse. So, over time, protons saturated at the metabolite's offset will accumulate into the water pool. The net effect will be a reduction in the signal of water, of an amount proportional to the concentration of the saturated metabolite and of its chemical exchange rate. By virtue of this accumulation, the MR signal from this metabolite is amplified hundreds-fold compared to conventional MR Spectroscopy (140-141). The acquisition returns a stack of images with the contrast in each image depending on the saturated frequency offset. For each pixel, it is possible to generate a spectrum, the Z-spectrum. The calculation of the CEST effect is commonly performed by evaluating the difference between the amount of saturation transferred, that is, the reduction of the water signal at a specific offset, and a reference value, usually the offset at the symmetric side of the water resonance:  $(S_{-\omega} - S_{\omega}) / S_{-\omega}$  (142).

CEST effects from amine, amide, sulfhydryl, and hydroxyl protons, each one with a specific resonance frequency range and associated with important endogenous metabolites, have been shown to provide

metabolic images of many healthy and pathological tissues, including brain (143-144), muscle (145-148), and cartilage (149), among others. ZSI images can reach high spatial resolution (down to 0.1/0.01 mm<sup>2</sup> in clinical/preclinical MRI) and can typically be acquired within 5 or 10 min, depending on the protocol.

Now, the contrast mechanism produced by the presaturation is not restricted to CEST effects. In fact, the largest signal decrease in the Z-spectrum is due to those spins directly irradiated in the water pool, which are subsequently imaged, producing close to null signal. This is the direct saturation of water and can span over a wide range of frequencies, depending on the  $T_2$  of water, the homogeneity of the field and the intensity of the RF field applied. Other contrasts generated by the saturation pulse are the magnetization transfer from semisolid structures like macromolecules, which, having very short  $T_2$ , presents with a very large linewidth (142); and the Nuclear Overhauser Enhancement effect, produced by the dipolar interaction from the metabolites, subsequently relayed to water through a CEST-like mechanism (140-142). All these different physical phenomena are encompassed in the structure of the Z-spectrum and can be highlighted or minimized by an accurate choice of the RF parameters or post processing strategies (140-142). The asymmetry analysis mentioned earlier, for example, has been introduced precisely with the intention of minimizing the impact of the large water direct saturation. But given the presence of many other contributors to the spectrum, alternatives processing methods have been proposed and among these, the most popular is surely the use of fitting models for the entire Z-spectrum. Here we use a model consisting of the sum of multiple Lorentzian curves, each one representing the MR signal of a single component:

$$S(\omega) = 1 - \sum_m^N L_m(\alpha, \gamma, \omega), \quad L_m(\alpha, \gamma, \omega) = \frac{\alpha}{1 + 4 \frac{(\omega - \omega_0)^2}{\gamma^2}} \quad (16)$$

Where  $\alpha$ ,  $\gamma$ ,  $\omega$  represents the amplitude, linewidth and frequency offset for each peak, respectively. By fitting the Z-spectrum to this model, it is possible to extract information about the precise resonance frequency of each component, and its concentration, proportional to the amplitude of the curve.

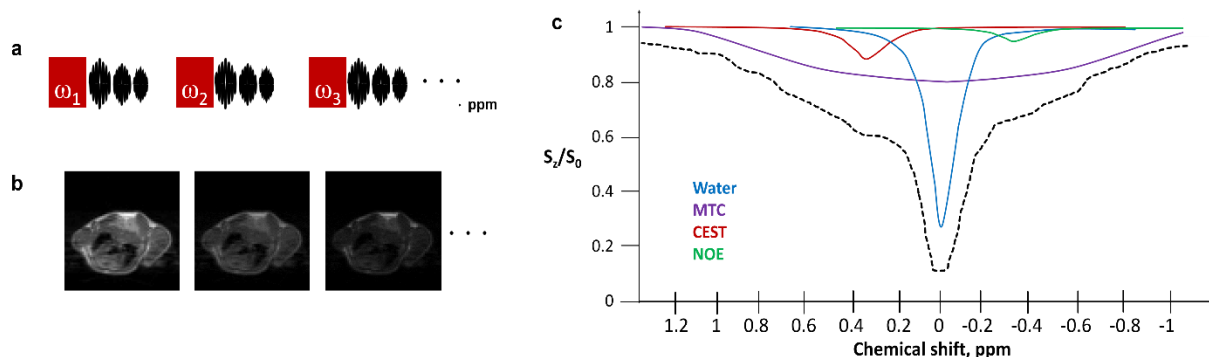


Figure 2-5 Z-spectrum MR imaging.

a) A series of saturation pulses are swept at different offsets and followed by image collection. b) Each image in the series shows a different contrast, depending on the saturated offset. c) In every pixel, the signal varies as a function of frequency. The Z-spectrum can be fitted to extract the isolated contribution from multiple proton pools.

In this context, this technique has hardly ever been implemented in adipose tissue, since the fat spins resonating close to water produce important direct saturation peaks themselves. It is clear that if the prevalence of such peaks is of the same order of the water one, it is almost impossible to obtain uncorrupted CEST measurement, especially through the asymmetry analysis, and so several strategies has been designed to remove them (150-151).

In this dissertation, the lipid signal will not be regarded as an artifact, but rather will be exploited and its direct saturation will be used in the production of biomarkers to study brown and browning adipose tissue.

## Bibliography

1. Ren J, Dimitrov I, Sherry AD, Malloy CR. Composition of adipose tissue and marrow fat in humans by  $^1\text{H}$  NMR at 7 Tesla. *J Lipid Res* 2008; 49:2055-2062.
2. Outwater EK, Blasbalg R, Siegelman ES, Vala M. Detection of lipid in abdominal tissues with opposed-phase gradient-echo images at 1.5T: techniques and diagnostic importance. *Radiographics* 1998; 18:1465-80.
3. Bley TA, Wieben O, François CJ, et al. Fat and water magnetic resonance imaging. *J Magn Reson Imaging* 2010; 31:4-18.
4. Del Grande F, Santini F, Herzka DA, et al. Fat-suppression techniques for 3-T MR imaging of the musculoskeletal system. *RadioGraphics* 2014; 34:217-233.
5. Dixon WT. Simple proton spectroscopic imaging. *Radiology* 1984; 153:189-194.
6. Glover G. Multipoint Dixon technique for water and fat proton and susceptibility imaging, *J Magn Reson Imaging* 1991;1:521-530.
7. Ma J. Dixon techniques for water and fat imaging. *J Magn Reson Imaging* 2008; 28:543-558.
8. Haase A, Frahm J, Hänicke W, Matthaei D.  $^1\text{H}$  NMR chemical shift selective (CHESS) imaging. *Phys Med Biol* 1985;30(4):341–344.12.
9. Keller PJ, Hunter WW Jr, Schmalbrock P. Multi-section fat-water imaging with chemical shift selective presaturation. *Radiology* 1987;164(2):539–541.
10. Bydder GM, Pennock JM, Steiner RE, Khenia S, Payne JA, Young IR. The short TI inversion recovery sequence: an approach to MR imaging of the abdomen. *Magn Reson Imaging* 1985;3(3):251–254.10.
11. Bydder GM, Young IR. Clinical use of the partial saturation and saturation recovery sequences in MR imaging. *J Comput Assist Tomogr* 1985;9(6): 1020–1032.
12. Bernstein MA, King KF, Zhou XJ. Basic pulse sequences. In: *Handbook of MRI pulse sequences*. Burlington, Mass: Elsevier, 2004; 622–624.17.
13. Krinsky G, Rofsky NM, Weinreb JC. Nonspecificity of short inversion time inversion recovery (STIR) as a technique of fat suppression: pitfalls in image interpretation. *AJR Am J Roentgenol* 1996;166(3): 523–526.18.
14. Bernstein MA, King KF, Zhou XJ. Adiabatic radio-frequency pulses. In: *Handbook of MRI pulse sequences*. Burlington, Mass: Elsevier, 2004; 190–198.

15. Meyer CH, Pauly JM, Macovski A, Nishimura DG. Simultaneous spatial and spectral selective excitation. *Magn Reson Med* 1990; 15: 287– 304.
16. Cameron I. Techniques of Fat Suppression.  
[http://cds.ismrm.org/protected/09MProceedings/files/Tues%20C36\\_01%20Cameron.pdf](http://cds.ismrm.org/protected/09MProceedings/files/Tues%20C36_01%20Cameron.pdf).  
Accessed April 29, 2013
17. Bernstein MA, King KF, Zhou XJ. Spatial radio-frequency pulses. In: Handbook of MRI pulse sequences. Burlington, Mass: Elsevier, 2004; 153–163.
18. Bley TA, Wieben O, François CJ, Brittain JH, Reeder SB. Fat and water magnetic resonance imaging. *J Magn Reson Imaging* 2010;31(1):4–18.
19. Dixon WT. Simple proton spectroscopic imaging. *Radiology* 1984;153(1):189–194.
20. Sepponen RE, Sipponen JT, Tanttu JI. A method for chemical shift imaging: demonstration of bone marrow involvement with proton chemical shift imaging. *J Comput Assist Tomogr* 1984;8:585–587.
21. Hernando D, Liang ZP, Kellman P. Chemical shift-based water/fat separation: a comparison of signal models. *Magn Reson Med* 2010;64:811–822.
22. Bydder M, Yokoo T, Hamilton G, et al. Relaxation effects in the quantification of fat using gradient echo imaging. *Magn Reson Imaging* 2008;26:347–359.
23. Eggers H, Bornert P. Chemical Shift Encoding-Based Water–Fat Separation Methods. *JMRI* 40:251–268 (2014).
24. Reeder S, Wen Z, Yu H, Pineda AR, Gold GE, Markl M, Pelc NJ. Multicoil Dixon Chemical Species Separation With an Iterative Least-Squares Estimation Method. *Mag Res Med* 51:35– 45 (2004).
25. Reeder SB, Pineda AR, Wen Z, Shimakawa A, Yu H, Brittain JH, Gold GE, Beaulieu CH, Pelc NJ. Iterative Decomposition of Water and Fat With Echo Asymmetry and Least-Squares Estimation (IDEAL): Application With Fast Spin-Echo Imaging. *Mag Res Med* 54:636 –644 (2005).
26. Pineda AR, Reeder SB, Wen Z, Pelc NJ. Cramer–Rao Bounds for Three-Point Decomposition of Water and Fat. *54:625– 635* (2005).
27. Yu H, Reeder SB, Shimakawa A, Brittain JH, Pelc NJ. Field Map Estimation with a Region Growing Scheme for Iterative 3-Point Water-Fat Decomposition. *Mag Res Med* 54:1032–1039 (2005).
28. Cui C, Shah A, Wu X, Jacob M. A rapid 3D fat-water decomposition method using globally optimal surface estimation (R-GOOSE). *Magn Reson Med*. 2018 Apr;79(4):2401-2407. doi: 10.1002/mrm.26843. Epub 2017 Jul 20. PMID: 28726301; PMCID: PMC5817637.

29. Diefenbach MN, Liu C, Karampinos DC. Generalized parameter estimation in multi-echo gradient-echo-based chemical species separation. *Quant Imaging Med Surg*. 2020 Mar;10(3):554-567. doi: 10.21037/qims.2020.02.07. PMID: 32269917; PMCID: PMC7136725.
30. Zhao F, Nielsen JF, Noll DC. Four dimensional spectral-spatial fat saturation pulse design. *Magn Reson Med*. 2014 Dec;72(6):1637-47. doi: 10.1002/mrm.25076. Epub 2013 Dec 17. PMID: 24347327; PMCID: PMC4061276.
31. Yuan J, Madore B, Panych LP. Fat-water selective excitation in balanced steady-state free precession using short spatial-spectral RF pulses. *J Magn Reson*. 2011 Feb;208(2):219-24. doi: 10.1016/j.jmr.2010.11.005. Epub 2010 Dec 4. PMID: 21134770; PMCID: PMC3034310.
32. Yuan J, Madore B, Panych LP. Spatially varying fat-water excitation using short 2DRF pulses. *Magn Reson Med*. 2010;63(4):1092-1097. doi:10.1002/mrm.22223
33. Hernando D, Kellman P, Haldar JP, Liang ZP. Robust water/fat separation in the presence of large field inhomogeneities using a graph cut algorithm. *Magn Reson Med*. 2010 Jan;63(1):79-90. doi: 10.1002/mrm.22177. PMID: 19859956; PMCID: PMC3414226.
34. Jafari R, Spincemaille P, Zhang J, Nguyen TD, Luo X, Cho J, Margolis D, Prince MR, Wang Y. Deep neural network for water/fat separation: Supervised training, unsupervised training, and no training. *Magn Reson Med*. 2021 Apr;85(4):2263-2277. doi: 10.1002/mrm.28546. Epub 2020 Oct 26. PMID: 33107127; PMCID: PMC7809709.
35. Grissom WA, Kerr AB, Holbrook AB, Pauly JM, Butts-Pauly K, Maximum linear-phase spectral-spatial radiofrequency pulses for fat-suppressed proton resonance frequency-shift MR thermometry, *Magn. Reson. Med* 62 (2009) 1242–1250, 10.1002/mrm.22118.
36. Yuan J, Mei CS, Madore B, McDannold NJ, Panych LP, Fast fat-suppressed reduced field-of-view temperature mapping using 2DRF excitation pulses, *J. Magn. Reson* 210 (2011) 38–43, 10.1016/j.jmr.2011.02.004.
37. Hofstetter LW, Yeo DTB, Dixon WT, Kempf JG, Davis CE, Foo TK, Fat-referenced MR thermometry in the breast and prostate using IDEAL, *J. Magn. Reson. Imaging* 36 (2012) 722– 732
38. Diakite M, Odéen H, Todd N, Payne A, Parker DL, Toward real-time temperature monitoring in fat and aqueous tissue during magnetic resonance-guided high-intensity focused ultrasound using a three-dimensional proton resonance frequency T1 method, *Magn. Reson. Med* 72 (2014) 178– 187, 10.1002/mrm.24900.

39. Hofstetter LW, Yeo DTB, Dixon WT, Marinelli L, Foo TK, Referenced MR thermometry using three-echo phase-based fat water separation method, *Magn. Reson. Imaging* 49 (2018) 86–93, 10.1016/j.mri.2018.01.002.
40. Shmatukha AV, Harvey PR, Bakker CJG, Correction of proton resonance frequency shift temperature maps for magnetic field disturbances using fat signal, *J. Magn. Reson. Imaging* 25 (2007) 579–587, 10.1002/jmri.20835.
41. Baron P, Deckers R, Bouwman JG, Bakker CJG, de Greef M, Viergever MA, Moonen CTW, Bartels LW, Influence of water and fat heterogeneity on fat-referenced MR thermometry, *Magn. Reson. Med* 75 (2016) 1187–1197, 10.1002/mrm.25727.
42. Soher BJ, Wyatt C, Reeder SB, MacFall JR, Noninvasive temperature mapping with MRI using chemical shift water-fat separation, *Magn. Reson. Med* 63 (2010) 1238–1246, 10.1002/mrm.22310.
43. Streicher MN, Schäfer A, Müller D, Kögler C, Reimer E, Dhital B, Trampel R, Rivera D, Pampel A, Ivanov D, Turner R, Frequency-selective asymmetric spin-echo EPI with parallel imaging for fast internally referenced MR Thermometry, in: *Int. Soc. Magn. Reson. Med*, 2011, p. 529.
44. Cheng C, Zou C, Wan Q, Qiao Y, Pan M, Tie C, Liang D, Zheng H, Liu X, Dual-step iterative temperature estimation method for accurate and precise fat-referenced PRFS temperature imaging, *Magn. Reson. Med* (2018) 1–13, 10.1002/mrm.27396.
45. Parker DL, Smith V, Sheldon P, Crooks LE, Fussell L, Temperature distribution measurements in two-dimensional NMR imaging, *Med. Phys* 10 (1983) 321–325.
46. Bloembergen N, Purcell EM, Pound RV, Relaxation effects in nuclear magnetic resonance absorption, *Phys. Rev* 73 (1948) 679–712.
47. Lewa CJ, Majewska Z, Temperature relationships of proton spin-lattice relaxation time T1 in biological tissues, *Bull. Cancer* 67 (1980) 525–530.
48. Diakite M, Odéen H, Todd N, Payne A, Parker DL, Toward real-time temperature monitoring in fat and aqueous tissue during magnetic resonance-guided high-intensity focused ultrasound using a three-dimensional proton resonance frequency T1 method, *Magn. Reson. Med* 72 (2014) 178–187, 10.1002/mrm.24900.
49. Kuroda KK, Iwabuchi TI, Obara MO, Honda MH, Temperature dependence of relaxation times in proton components of fatty acids, *Magn. Reson. Med. Sci* 10 (2011) 177–183.
50. Hey S, de Smet M, Stehning C, Grull H, Keupp J, Moonen CTW, Ries M, Grull H, Keupp J, Moonen CTW, Ries M, Simultaneous T1 measurements and proton resonance frequency shift based

thermometry using variable flip angles, *Magn. Reson. Med* 67 (2012) 457–463, 10.1002/mrm.22987.

51. Todd N, Diakite M, Payne A, Parker DL, Hybrid proton resonance frequency/T1 technique for simultaneous temperature monitoring in adipose and aqueous tissues, *Magn. Reson. Med* 69 (2013) 62–70.
52. Baron P, Deckers R, Knuttel FM, Bartels LW, T1 and T2 temperature dependence of female human breast adipose tissue at 1.5 T: groundwork for monitoring thermal therapies in the breast, *NMR Biomed* (2015), 10.1002/nbm.3410.
53. Fram EK, Herfkens RJ, Johnson GA, Glover GH, Karis JP, Shimakawa A, Perkins TG, Pelc NJ, Rapid calculation of T1 using variable flip angle gradient refocused imaging, *Magn. Reson. Imaging* 5 (1987) 201–208.
54. Deoni SCL, Peters TM, Rutt BK, High-resolution T1 and T2 mapping of the brain in a clinically acceptable time with DESPOT1 and DESPOT2, *Magn. Reson. Med* 53 (2005) 237–241, 10.1002/mrm.20314.
55. Todd N, Diakite M, Payne A, Parker DL, In vivo evaluation of multi-echo hybrid PRF/T1 approach for temperature monitoring during breast MR-guided focused ultrasound surgery treatments, *Magn. Reson. Med* 72 (2014) 793–799.
56. Parker DL, Applications of NMR imaging in hyperthermia: an evaluation of the potential for localized tissue heating and noninvasive temperature monitoring, *IEEE Trans. Biomed. Eng* 31 (1984) 161–167.
57. Baron P, Ries M, Deckers R, de Greef M, Tanttu J, Köhler M, Viergever MA, Moonen CTW, Bartels LW, Kohler M, Viergever MA, Moonen CTW, Bartels LW, In vivo T2 -based MR thermometry in adipose tissue layers for high-intensity focused ultrasound near-field monitoring, *Magn. Reson. Med* 72 (2014) 1057–1064, 10.1002/mrm.25025.
58. Ozhinsky E, Kohi MP, Ghanouni P, Rieke V, T2-based temperature monitoring in abdominal fat during MR-guided focused ultrasound treatment of patients with uterine fibroids, *J. Ther. Ultrasound* 3 (2015) 1–10, 10.1186/s40349-015-0036-5.
59. Le Bihan D, Delannoy J, Levin RL, Temperature mapping with MR imaging of molecular diffusion: application to hyperthermia, *Radiology* 171 (1989) 853–857, 10.1148/radiology. 171.3.2717764.
60. Simpson JH, Carr HY, Diffusion and nuclear spin relaxation in water, *Phys. Rev* 116 (1958) 131–150, 10.16251/j.cnki.1009-2307.2011.04.021.

61. Delannoy J, Chen CN, Turner R, Levin RL, Delannoy J, Chen CN, Turner R, Levin RL, Le Bihan D, Noninvasive temperature imaging using diffusion MRI, *Magn. Reson. Med* 19 (1991) 333–339. .
62. Il'yasov KA, Hennig J, Single-shot diffusion-weighted RARE sequence: application for temperature monitoring during hyperthermia session, *J. Magn. Reson. Imaging* 8 (1998) 1296–1305, 10.1002/jmri.1880080617.
63. Bernstein MA, King KF, Zhou XJ, *Handbook of MRI Pulse Sequences*, Elsevier, London, 2004.
64. Moseley ME, Cohen Y, Mintorovitch J, Chileuitt L, Shimizu H, Kucharczyk J, Wendland MF, Early detection of regional cerebral ischemia in cats: comparison of diffusion- and T2-weighted MRI and spectroscopy, *Magn. Reson. Med* 14 (1990) 330–346.
65. Zhang Y, Samulski TV, Joines WT, Mattiello J, Levin RL, LeBihan D, On the accuracy of noninvasive thermometry using molecular diffusion magnetic resonance imaging, *Int. J. Hyperth* 8 (1992) 263–274.
66. De Poorter J, Dewagter C, Dedeene Y, Thomsen C, Stahlberg F, Achten E, The proton-resonancefrequency-shift method compared with molecular diffusion for quantitative measurement of twodimensional time-dependent temperature distribution in a phantom, *J. Magn. Reson. Ser. B* 103 (1994) 234–241.
67. Stollberger, R., et al., Temperature monitoring of interstitial thermal tissue coagulation using MR phase images. *J Magn Reson Imaging*, 1998. 8(1): p. 188-96.
68. Weisskoff RM, Kiihne S, MRI susceptometry-image-based measurement of absolute susceptibility of MR contrast agents and human blood, *Magn. Reson. Med* 24 (1992) 375–383.
69. Vallo S, Eichler K, Kelly K, Schulz B, Bartsch G, Haferkamp A, Vogl TJ, Zangos S, MR-guided laser-induced thermotherapy in ex vivo porcine kidney: comparison of four different imaging sequences, *Lasers Surg. Med* 46 (2014) 558–562, 10.1002/lsm.22262.
70. Stafford RJ, Hazle JD, Glover GH, Monitoring of high-intensity focused ultrasound-induced temperature changes in vitro using an interleaved spiral acquisition, *Magn. Reson. Med* 43 (2000) 909–912.
71. Zou C, Shen H, He M, Tie C, Chung Y-C, Liu X, A fast referenceless PRFS-based MR thermometry by phase finite difference, *Phys. Med. Biol* 58 (2013) 5735–5751, 10.1088/0031-9155/58/16/5735.
72. Zou C, Tie C, Pan M, Wan Q, Liang C, Liu X, Chung Y-C, Referenceless MR thermometry—a comparison of five methods, *Phys. Med. Biol* 62 (2017) 1–16, 10.1088/1361-6560/62/1/1.

73. Gellermann J, Wlodarczyk W, Hildebrandt B, Ganter H, Nicolau A, Rau B, Tilly W, Fa H, Nadobny J, Felix R, Wust P, Noninvasive magnetic resonance thermography of recurrent rectal carcinoma in a 1.5 Tesla hybrid system rectal carcinoma in a 1.5 Tesla hybrid system, *Cancer Res* 65 (2005) 5872–5880, 10.1158/0008-5472.CAN-04-3952.
74. Kuroda K, Oshio K, Chung a.H., Hynynen K, Jolesz F.a., Temperature mapping using the water proton chemical shift: a chemical shift selective phase mapping method, *Magn. Reson. Med* 38 (1997) 845–851, 10.1002/mrm.1910380523.
75. Svedin BT, Dillon CR, Parker DL, Effect of k-space-weighted image contrast and ultrasound focus size on the accuracy of proton resonance frequency thermometry, *Magn. Reson. Med* 81 (2019) 247–257, 10.1002/mrm.27383.
76. McDannold N, Tempny C, Jolesz F, Hynynen K, Evaluation of referenceless thermometry in MRI-guided focused ultrasound surgery of uterine fibroids, *J. Magn. Reson. Imaging* 28 (2008) 1026–1032, 10.1002/jmri.21506.
77. Salomir R, Viallon M, Kickhefel A, Roland J, Morel DR, Petrusca L, Auboiroux V, Goget T, Terraz S, Becker CD, Gross P, Reference-free PRFS MR-thermometry using near-harmonic 2-D reconstruction of the background phase, *IEEE Trans. Med. Imaging* 31 (2012) 287–301, 10.1109/TMI.2011.2168421.
78. Svedin BT, Payne A, Parker DL, Respiration artifact correction in three-dimensional proton resonance frequency MR thermometry using phase navigators, *Magn. Reson. Med* 76 (2016) 206–213, 10.1002/mrm.25860.
79. Dadakova T, Gellermann J, Voigt O, Korvink JG, Pavlina JM, Hennig J, Bock M, Fast PRF-based MR thermometry using double-echo EPI: in vivo comparison in a clinical hyperthermia setting, *Magn. Reson. Mater. Phys., Biol. Med* 28 (2015) 305–314, 10.1007/s10334-014-0467-y.
80. Gellermann J, Wlodarczyk W, Feussner A, Föhling H, Nadobny J, Hildebrandt B, Felix R, Wust P, Methods and potentials of magnetic resonance imaging for monitoring radiofrequency hyperthermia in a hybrid system, *Int. J. Hyperth* 21 (2005) 497–513, 10.1080/02656730500070102.
81. Weidensteiner C, Keroui N, Quesson B, Denis de Senneville B, Trillaud H, Moonen CTW, Stability of real-time MR temperature mapping in healthy and diseased human liver, *J. Magn. Reson. Imaging* 19 (2004) 438–446.
82. Weisskoff RM, Kiihne S, MRI susceptometry-image-based measurement of absolute susceptibility of MR contrast agents and human blood, *Magn. Reson. Med* 24 (1992) 375–383.

83. Soher BJ, Wyatt C, Reeder SB, MacFall JR, Noninvasive temperature mapping with MRI using chemical shift water-fat separation, *Magn. Reson. Med* 63 (2010) 1238–1246, 10.1002/mrm.22310.
84. Diakite M, Payne A, Todd N, Parker DL, Irreversible change in the T1 temperature dependence with thermal dose using the proton resonance frequency-T1 technique, *Magn. Reson. Med* 69 (2013) 1122–1130.
85. Gupta RK, A new look at the method of variable nutation angle for the measurement of spinlattice relaxation times using fourier transform NMR, *J. Magn. Reson* 25 (1977) 231–235, 10.1016/0022-2364(77)90138-X.
86. Fram EK, Herfkens RJ, Johnson GA, Glover GH, Karis JP, Shimakawa A, Perkins TG, Pelc NJ, Rapid calculation of T1 using variable flip angle gradient refocused imaging, *Magn. Reson. Imaging* 5 (1987) 201–208.
87. Hamilton G, Smith DL, Jr., Bydder M, Nayak KS, Hu HH. MR properties of brown and white adipose tissues. *J Magn Reson Imaging*. (2011) 34:468– 73. doi: 10.1002/jmri.22623.
88. Reeder SB, Hu HH, Sirlin CB. Proton density fat-fraction: a standardized MR-based biomarker of tissue fat concentration. *J Magn Reson Imaging*. (2012) 36:1011–4. doi: 10.1002/jmri.23741.
89. Yokoo T, Serai SD, Pirasteh A, Bashir MR, Hamilton G, Hernando D, et al. Linearity, bias, and precision of hepatic proton density fat fraction measurements by using MR imaging: a meta-analysis. *Radiology*. (2018) 286:486–98. doi: 10.1148/radiol.2017170550
90. Karampinos DC, Ruschke S, Dieckmeyer M, Diefenbach M, Franz D, Gersing AS, et al. Quantitative MRI and spectroscopy of bone marrow. *J Magn Reson Imaging*. (2018) 47:332–53. doi: 10.1002/jmri.25769.
91. Hamilton G, Schlein AN, Middleton MS, Hooker CA, Wolfson T, Gamst AC, et al. In vivo triglyceride composition of abdominal adipose tissue measured by (1) H MRS at 3T. *J Magn Reson Imaging*. (2017) 45:1455– 63. doi: 10.1002/jmri.25453
92. Karampinos DC, Yu H, Shimakawa A, Link TM, Majumdar S. T(1)- corrected fat quantification using chemical shift-based water/fat separation: application to skeletal muscle. *Magn Reson Med*. (2011) 66:1312– 26. doi: 10.1002/mrm.22925
93. Liu CY, McKenzie CA, Yu H, Brittain JH, Reeder SB. Fat quantification with IDEAL gradient echo imaging: correction of bias from T(1) and noise. *Magn Reson Med*. (2007) 58:354–64. doi: 10.1002/mrm.21301

94. Ruschke S, Eggers H, Kooijman H, Diefenbach MN, Baum T, Haase A, et al. Correction of phase errors in quantitative water-fat imaging using a monopolar time-interleaved multi-echo gradient echo sequence. *Magn Reson Med.* (2017) 78:984–96. doi: 10.1002/mrm.26485
95. Yu H, Shimakawa A, McKenzie CA, Lu W, Reeder SB, Hinks RS, et al. Phase and amplitude correction for multi-echo water-fat separation with bipolar acquisitions. *J Magn Reson Imaging.* (2010) 31:1264– 71. doi: 10.1002/jmri.22111
96. Wang X, Hernando D, Reeder SB. Sensitivity of chemical shift-encoded fat quantification to calibration of fat MR spectrum. *Magn Reson Med.* (2016) 75:845–51. doi: 10.1002/mrm.25681
97. Hernando D, Sharma SD, Kramer H, Reeder SB. On the confounding effect of temperature on chemical shift-encoded fat quantification. *Magn Reson Med.* (2014) 72:464–70. doi: 10.1002/mrm.24951
98. McCallister D, Zhang L, Burant A, Katz L, Branca RT. Effect of microscopic susceptibility gradients on chemical-shift-based fat fraction quantification in supraclavicular fat. *J Magn Reson Imaging.* (2019) 49:141– 51. doi: 10.1002/jmri.26219
99. Hernando D, Kellman P, Haldar JP, Liang ZP. Robust water/fat separation in the presence of large field inhomogeneities using a graph cut algorithm. *Magn Reson Med.* (2010) 63:79–90. doi: 10.1002/mrm.22177.
100. Diefenbach MN, Ruschke S, Eggers H, Meineke J, Rummeny EJ, Karampinos DC. Improving chemical shift encoding-based water-fat separation based on a detailed consideration of magnetic field contributions. *Magn Reson Med.* (2018) 80:990–1004. doi: 10.1002/mrm.27097
101. Sharma SD, Artz NS, Hernando D, Horng DE, Reeder SB. Improving chemical shift encoded water-fat separation using object-based information of the magnetic field inhomogeneity. *Magn Reson Med.* (2015) 73:597– 604. doi: 10.1002/mrm.25163
102. Feldmann HM, Golozoubova V, Cannon B, Nedergaard J. UCP1 ablation induces obesity and abolishes diet-induced thermogenesis in mice exempt from thermal stress by living at thermoneutrality. *Cell Metab.* (2009) 9:203– 9. doi: 10.1016/j.cmet.2008.12.014
103. Cinti S. The adipose organ at a glance. *Dis Model Mech.* (2012) 5:588– 94. doi: 10.1242/dmm.009662
104. de Jong JMA, Sun W, Pires ND, Frontini A, Balaz M, Jespersen NZ, et al. Human brown adipose tissue is phenocopied by classical brown adipose tissue in physiologically humanized mice. *Nat Metab.* (2019) 1:830– 43. doi: 10.1038/s42255-019-0101-4

105. Hu HH, Yin L, Aggabao PC, Perkins TG, Chia JM, Gilsanz V. Comparison of brown and white adipose tissues in infants and children with chemicalshift-encoded water-fat MRI. *J Magn Reson Imaging*. (2013) 38:885– 96. doi: 10.1002/jmri.24053
106. Gifford A, Towse TF, Walker RC, Avison MJ, Welch EB. Characterizing active and inactive brown adipose tissue in adult humans using PETCT and MR imaging. *Am J Physiol Endocrinol Metab*. (2016) 311:E95– 104. doi: 10.1152/ajpendo.00482.2015
107. Lundstrom E, Strand R, Johansson L, Bergsten P, Ahlstrom H, Kullberg J. Magnetic resonance imaging cooling-reheating protocol indicates decreased fat fraction via lipid consumption in suspected brown adipose tissue. *PLoS ONE*. (2015) 10:e0126705. doi: 10.1371/journal.pone.0126705
108. Deng J, Neff LM, Rubert NC, Zhang B, Shore RM, Samet JD, et al. MRI characterization of brown adipose tissue under thermal challenges in normal weight, overweight, and obese young men. *J Magn Reson Imaging*. (2018) 47:936–47. doi: 10.1002/jmri.25836
109. Franz D, Diefenbach MN, Treibel F, Weidlich D, Syvari J, Ruschke S, et al. Differentiating supraclavicular from gluteal adipose tissue based on simultaneous PDFF and T2 \* mapping using a 20- echo gradient-echo acquisition. *J Magn Reson Imaging*. (2019) 50:424–34. doi: 10.1002/jmri.26661
110. Warren WS, Lee S, Richter W, Vathiyam S. Correcting the classical dipolar demagnetizing field in solution NMR. *Chem Phys Lett*. (1995) 247:207– 14. doi: 10.1016/0009-2614(95)01184-5
111. Levitt MH. Demagnetization field effects in two-dimensional solution NMR. *Concept Magn Reson*. (1996) 8:77– 103. doi: 10.1002/(SICI)1099-0534(1996)8:2<77::AIDCMR1>3.0.CO;2-
112. Bao J, Cui X, Cai S, Zhong J, Cai C, Chen Z. Brown adipose tissue mapping in rats with combined intermolecular double-quantum coherence and Dixon water-fat MRI. *NMR Biomed*. (2013) 26:1663–71. doi: 10.1002/nbm. 3000
113. Branca RT, Zhang L, Warren WS, Auerbach E, Khanna A, Degan S, et al. In vivo noninvasive detection of brown adipose tissue through intermolecular zero-quantum MRI. *PLoS ONE*. (2013) 8:e74206. doi: 10.1371/journal.pone.0074206
114. Verma SK, Nagashima K, Yaligar J, Michael N, Lee SS, Xianfeng T, et al. Differentiating brown and white adipose tissues by high-resolution diffusion NMR spectroscopy. *J Lipid Res*. (2017) 58:289–98. doi: 10.1194/jlr. D072298

115. Weidlich D, Honecker J, Gmach O, Wu M, Burgkart R, Ruschke S, et al. Measuring large lipid droplet sizes by probing restricted lipid diffusion effects with diffusion-weighted MRS at 3T. *Magn Reson Med.* (2019) 81:3427– 39. doi: 10.1002/mrm.27651
116. Weidlich D, Zamskiy M, Maeder M, Ruschke S, Marburg S, Karampinos DC. Reduction of vibration-induced signal loss by matching mechanical vibrational states: application in high b-value diffusion-weighted MRS. *Magn Reson Med.* (2019) 84:39–51. doi: 10.1002/mrm.28128
117. Weidlich D, Hock A, Ruschke S, Franz D, Hauner H, Rummeny EJ, et al., Improving the quality of DW spectra in the supraclavicular fossa with a navigator-gated and cardiac-triggered flow-compensated diffusion-weighted STEAM MRS acquisition. In: *Proceedings of 25th Int Society for Magnetic Resonance in Medicine.* Honolulu, HI (2017).
118. Wu M, Weidlich D, Ruschke S, Franz D, Karampinos DC. On the technical challenges of diffusion-weighted mr spectroscopy for water ADC quantification in human supraclavicular fat. In: *Proceedings of the 27th Int Society for Magnetic Resonance in Medicine.* Montréal, QC (2019)
119. Wu M, Held C, Patzelt L, Weidlich D, Ruschke S, Mengel L, et al. Brown adipose tissue water ADC quantification with Diffusion-Weighted MR Spectroscopy in the human supraclavicular fat. In: *ISMRM Workshop on MRI of Obesity & Metabolic Disorders.* Singapore (2019)
120. Muzik O, Mangner TJ, Granneman JG. Assessment of oxidative metabolism in brown fat using PET imaging. *Front Endocrinol.* (2012) 3:15. doi: 10.3389/fendo.2012.00015
121. Muzik O, Mangner TJ, Leonard WR, Kumar A, Janisse J, Granneman JG. 15O PET measurement of blood flow and oxygen consumption in cold-activated human brown fat. *J Nucl Med.* (2013) 54:523– 31. doi: 10.2967/jnumed.112.111336
122. Sbarbati A, Cavallini I, Marzola P, Nicolato E, Osculati F. Contrast-enhanced MRI of brown adipose tissue after pharmacological stimulation. *Magn Reson Med.* (2006) 55:715–8. doi: 10.1002/mrm.20851
123. Yaligar J, Verma SK, Gopalan V, Rengaraj A, Xianfeng T, Velan SS, editors. Evaluation of the vascular perfusion in activated brown adipose tissue by dynamic contrast enhanced MR imaging. In: *Proceedings of 25th Int Society for Magnetic Resonance in Medicine.* Honolulu, HI (2017).

124. Yaligar J, Verma SK, Gopalan V, Anantharaj R, Thu Le GT, Kaur K, et al. Dynamic contrast-enhanced MRI of brown and beige adipose tissues. *Magn Reson Med.* (2019) 84:384–95. doi: 10.1002/mrm.28118
125. Chen YI, Cypess AM, Sass CA, Brownell AL, Jokivarsi KT, Kahn CR, et al. Anatomical and functional assessment of brown adipose tissue by magnetic resonance imaging. *Obesity (Silver Spring).* (2012) 20:1519– 26. doi: 10.1038/oby.2012.22
126. Jung CS, Heine M, Freund B, Reimer R, Koziol EJ, Kaul MG, et al. Quantitative activity measurements of brown adipose tissue at 7 T magnetic resonance imaging after application of triglyceriderich lipoprotein 59Fe-superparamagnetic iron oxide nanoparticle: intravenous versus intraperitoneal approach. *Invest Radiol.* (2016) 51:194–202. doi: 10.1097/RLI.0000000000000235
127. Khanna A, Branca RT. Detecting brown adipose tissue activity with BOLD MRI in mice. *Magn Reson Med.* (2012) 68:1285–90. doi: 10.1002/mrm.24118
128. Antonacci MA, McHugh C, Kelley M, McCallister A, Degan S, Branca RT. Direct detection of brown adipose tissue thermogenesis in UCP1– /– mice by hyperpolarized <sup>129</sup>Xe MR thermometry. *Sci Rep.* (2019) 9:14865. doi: 10.1038/s41598-019-51483-4
129. Branca RT, He T, Zhang L, Floyd CS, Freeman M, White C, et al. Detection of brown adipose tissue and thermogenic activity in mice by hyperpolarized xenon MRI. *Proc Natl Acad Sci USA.* (2014) 111:18001– 6. doi: 10.1073/pnas.1403697111
130. Abreu-Vieira G, Hagberg CE, Spalding KL, Cannon B, Nedergaard J. Adrenergically stimulated blood flow in brown adipose tissue is not dependent on thermogenesis. *Am J Physiol Endocrinol Metab.* (2015) 308:E822–9. doi: 10.1152/ajpendo.00494.2014
131. Cannon B, Nedergaard J. Brown adipose tissue: function and physiological significance. *Physiol Rev.* (2004) 84:277– 359. doi: 10.1152/physrev.00015.2003
132. Sun L, Verma S, Michael N, Chan SP, Yan J, Sadananthan SA, et al. Brown adipose tissue: multimodality evaluation by PET, MRI, infrared thermography, and whole-body calorimetry (TACTICAL-II). *Obesity.* (2019) 27:1434–42. doi: 10.1002/oby.22560
133. Law J, Chalmers J, Morris DE, Robinson L, Budge H, Symonds ME. The use of infrared thermography in the measurement and characterization of brown adipose tissue activation. *Temperature (Austin).* (2018) 5:147– 61. doi: 10.1080/23328940.2017.1397085
134. Sprinkhuizen SM, Konings MK, van der Bom MJ, Viergever MA, Bakker CJ, Bartels LW. Temperature-induced tissue susceptibility changes lead to significant temperature errors in

- PRFS-based MR thermometry during thermal interventions. *Magn Reson Med.* (2010) 64:1360–72. doi: 10.1002/mrm.22531
135. Cheng C, Zou C, Wan Q, Qiao Y, Tie C, Pan M, et al. Magnetic resonance temperature imaging in activated brown adipose tissue of rat. In: *Proceedings of 27th Int Society for Magnetic Resonance in Medicine*. Montréal, QC (2019).
  136. Galiana G, Branca RT, Jenista ER, Warren WS. Accurate temperature imaging based on intermolecular coherences in magnetic resonance. *Science.* (2008) 322:421–4. doi: 10.1126/science.1163242
  137. Zhang L, McCallister A, Koshlap KM, Branca RT. Correlation distance dependence of the resonance frequency of intermolecular zero quantum coherences and its implication for MR thermometry. *Magn Reson Med.* (2018) 79:1429–38. doi: 10.1002/mrm.26801
  138. Zhang L, Burant A, McCallister A, Zhao V, Koshlap KM, Degan S, et al. Accurate MR thermometry by hyperpolarized (<sup>129</sup>Xe). *Magn Reson Med.* (2017) 78:1070–9. doi: 10.1002/mrm.26506
  139. Ward KM, Balaban RS. Determination of pH using water protons and Chemical Exchange Dependent Saturation Transfer (CEST). *Magnetic Resonance in Medicine.* 2000;44:799-802. doi: 10.1002/1522-2594(200011)44:5<799::AID-MRM18>3.0.CO;2-S. PubMed PMID: 11064415
  140. Vinogradov, E., A.D. Sherry, and R.E. Lenkinski, CEST: From basic principles to applications, challenges and opportunities. *Journal of Magnetic Resonance*, 2013. 229: p. 155-172.
  141. Van Zijl, P.C.M. and N.N. Yadav, Chemical exchange saturation transfer (CEST): What is in a name and what isn't? *Magnetic Resonance in Medicine*, 2011. 65: p. 927-948.
  142. Zaiss, M. and P. Bachert, Chemical exchange saturation transfer (CEST) and MR Z-spectroscopy in vivo: a review of theoretical approaches and methods. *Phys. Med. Biol.*, 2013. 58: p. 221-269.
  143. Zhou, J., et al., Amide proton transfer (APT) contrast for imaging of brain tumors. *Magn Reson Med*, 2003. 50(6): p. 1120-6.
  144. Cai, K., et al., Magnetic resonance imaging of glutamate. *Nat Med*, 2012. 18(2): p. 302-6.
  145. Cai, K., et al., Creatine CEST MRI for Differentiating Gliomas with Different Degrees of Aggressiveness. *Mol Imaging Biol*, 2017. 19(2): p. 225-232.

146. Cai, K., et al., CEST signal at 2ppm (CEST@2ppm) from Z-spectral fitting correlates with creatine distribution in brain tumor. *NMR Biomed*, 2015. 28(1): p. 1-8.
147. Haris, M., et al., A technique for in vivo mapping of myocardial creatine kinase metabolism. *Nat Med*, 2014. 20(2): p. 209-14.
148. Kogan, F., et al., Method for high-resolution imaging of creatine in vivo using chemical exchange saturation transfer. *Magn Reson Med*, 2014. 71(1): p. 164-72.
149. Ling, W., et al., Assessment of glycosaminoglycan concentration in vivo by chemical exchange-dependent saturation transfer (gagCEST). *Proc Natl Acad Sci U S A*, 2008. 105(7): p. 2266-70.
150. Sun, P.Z., et al., Suppression of lipid artifacts in amide proton transfer imaging. *Magn Reson Med*, 2005. 54(1): p. 222-5.
151. Dula, A.N., et al., Amide proton transfer imaging of the breast at 3 T: establishing reproducibility and possible feasibility assessing chemotherapy response. *Magn Reson Med*, 2013. 70(1): p. 216-24.

### 3. MAPPING BROWN ADIPOSE TISSUE BASED ON FAT WATER FRACTION PROVIDED BY Z-SPECTRAL IMAGING

(Previously published as Scotti A, Tain RW, Li W, Gil V, Liew CW, Cai K. Mapping brown adipose tissue based on fat water fraction provided by Z-spectral imaging. J Magn Reson Imaging. 2018 Jun;47(6):1527-1533.)

#### 3.1 Background and Introduction

Over the recent years the study of fat has attracted increasing interest of clinicians and researchers as it grew from being considered a simple energy storage tissue to a much more faceted organ secreting hormones involved in critical functions, from metabolism regulation to motivation and depression(1,2). In particular, the last ten years have seen the resurgence of the interest in brown adipose tissue (BAT). This peculiar kind of fat has a great significance in whole-body energy balance, given to its property of converting triglycerides and glucose into heat, through the non-shivering thermogenesis process(3–6). Moreover, BAT has a great biological relevance in metabolic diseases and has been shown to be reduced in obesity and insulin resistance subjects(7–10). Localization and quantification of BAT reservoirs is therefore key to study the disrupted metabolic homeostasis and investigate potential treatment strategies.

Currently,  $^{18}\text{F}$ FDG-PET/CT is the standard method to detect BAT activation by measuring the increased glucose uptake due to BAT metabolism. However, it has been shown that  $^{18}\text{F}$ -FDG uptake can be fully maintained even when oxygen consumption and BAT thermogenesis are diminished, suggesting that increased BAT  $^{18}\text{F}$ -FDG uptake can occur independently of thermal function (11). Also, PET radiation exposure limits its application to longitudinal studies necessary for treatment assessment, and can only detect active BAT function, while it is unusable for measuring the resting-state BAT mass (12).

Conventional and novel MRI-based techniques have been used as well, in particular to target the structural difference in relative water and lipid content between brown and white adipose tissues (WAT). The latter in fact is characterized by large lipid droplets taking up most of the intracellular space, while BAT shares the space between smaller lipid droplets and other organelles immersed in the cytoplasm(12–14). The cell structural difference leads to a different balance of fat and water within the cells, providing a marker for MRI.

Dixon multiecho MRI has an established track record in the study of fat and can differentiate white and brown adipose reservoirs, providing a measure of the relative amount of fat contained in the tissue, i.e. fat-water fraction(14,15). However, despite the valuable contribution of reconstruction algorithm like IDEAL (Iterative Decomposition of water and fat with Echo Asymmetry and Least square estimation), the technique still has some pitfalls, like the ever-present sensitivity to phase wrapping and  $B_0$  field inhomogeneity artifacts(16–19). On the other hand, innovative and promising approaches under development, such as multiple quantum coherence(20) and hyperpolarized Xe gas imaging(21), face challenges in signal to noise ratio and the requirement of exogenous contrast agents and/or special instruments that are not readily available in most of the clinical scanners.

Z-Spectrum Imaging (ZSI), based on the acquisition of multiple images following a saturation pulse swept over a short range of frequencies(22,23), shows both water and fat dips due to the direct saturation at their resonance frequencies. With these signals, fat-water fraction may be quantified and used to differentiate BAT from WAT and lean tissues. This technique is intrinsically immune from phase heterogeneity given that information on water and fat resonance and  $\Delta B_0$  can all be determined from the Z-Spectrum. In this study, we aimed to address the efficacy of ZSI in fat-water fraction quantification and therefore BAT detection.

## 3.2 Materials and Methods

The procedure was first tested on *ex vivo* tissue samples and calibrated on phantoms with known mixture of oil and water. It was then applied *in vivo* on healthy mice and finally translated to human subjects. All animals and human studies were performed according to protocols approved by the Institutional Animal Care and Use Committee and Institutional Review Board. Signed informed consent was obtained by all volunteers.

### 3.2.1 *Ex vivo* studies

Specimens of fat and lean tissues were extracted from 3 healthy C57BL/6 mice (male, 7 weeks old). Lean muscle tissue from the flank, WAT from the visceral area and BAT from the interscapular depot were resected from freshly deceased animals and pressed into separate NMR tubes (5 mm in diameter, New Era Enterprises, Inc., Vineland, NJ, USA). For calibration purpose, a cylinder phantom (1cm diameter) was prepared containing water and peanut oil, chosen to mimic human triglycerides(24,25). In order to provide different fat / water ratios, the imaging slice (2.5 mm thick) was placed at an angle (56° was found to be optimal for this set up) crossing the oil-water interface such as to have a linear gradient of fat-water fraction in the image plane. The actual fat-water fraction was estimated geometrically from the sagittal T<sub>2</sub> images as the fraction of oil volume covered within the slice depth at any position, resulting in partial volumes overlap of oil and water.

MRI was carried out at an Agilent Varian 9.4T preclinical scanner with a 39 mm proton volume coil. A CEST sequence was used to acquire Z-Spectra with a square saturation pulse of 3.5  $\mu$ T for 1s and frequency offsets ranging from -5 to 5 ppm at intervals of 0.25 ppm, together with  $\pm 10$ ,  $\pm 20$ ,  $\pm 100$  ppm offsets. The saturation pulse was followed by single-slice fast spin echo (FSE) readout with parameters: FOV = 40 x 40 mm<sup>2</sup>, matrix size = 128 x 128, echo train length (ETL) = 16, effective TE = 4.9 ms, T<sub>1</sub> delay time, i.e. the time between successive repetitions = 3 s. The acquisition time for the entire Z-Spectrum

was about 26 min. A WATER Saturation Shift Referencing (WASSR) scheme was adopted for correction of  $B_0$  inhomogeneity as previously reported(26). The sequence had a low-power pulse of 0.4  $\mu$ T for 200 ms and frequency range from -1 to +1 ppm and same readout parameters as the Z-Spectrum Imaging.

### 3.2.2 *In vivo* mouse study

Four C57BL/6 male mice, 7 weeks old, were used in this study. As a general procedure for all the mice, anesthesia was induced by 2 % isoflurane, later maintained at 1–1.5 % in 100 %  $O_2$  via a nose cone with spontaneous respiration throughout the experiment. A rectal probe was used to monitor the body temperature, which was maintained at  $33 \pm 0.5$  °C via regulating the warm air flow into the scanner bore. Temperature and respiration rate were monitored using an MRI- compatible physiological monitoring system (Model 1025, SA Instruments Inc., Stony Brook, NY, USA). The interscapular region containing the largest known BAT depot in mice was placed in the center of the RF coil. First and second order shimming was performed in this area prior to the acquisition.  $T_2$ -weighted images of the region were obtained for anatomical reference. Single slice Z-Spectrum was acquired through the center regions of interscapular BAT depot using the same protocol as in the *ex vivo* studies.

### 3.2.3 *In vivo* human study

The ZSI concept was then tested on healthy human subjects ( $n=5$ , male, age 30-40, BMI 21-27) at a clinical 3T MRI scanner (GE750, GE Healthcare, Waukesha, WI) with a 32 channels cardiac coil. The saturation pulse consisted of a train of 10 Hanning windowed saturation pulses 98 ms long with a 2 ms inter-pulse delay, resulting in a excitation of 3.5  $\mu$ T for 1 s. Saturation was followed by a single shot FLASH readout with centric phase encoding order with parameters: slice thickness = 10 mm, flip angle =  $10^\circ$ , shot TR = 6 s, TE = 3.2 ms, field of view =  $48 \times 48$  cm<sup>2</sup>, matrix size =  $128 \times 128$ , and in-plane resolution =  $3.75 \times 3.75$  mm<sup>2</sup>. CEST images were collected at 16 frequencies, specifically from -4.75 to 4.75 ppm with 0.64 ppm intervals and a 100 ppm image for referencing. The acquisition time for

collecting the partial Z-Spectrum was about 3.5 min. In addition, a Dixon 6-points sequence with IDEAL reconstruction was acquired in the same session to quantify the fat fraction distribution. The sequence is the GE commercial version (IDEAL IQ), with a model including 6 fat peaks and 6 echoes:  $TE_1 = 1.3$  ms,  $\Delta TE = 2.0$  ms,  $TR = 7.3$  s, matrix size =  $256 \times 256$  (27,28).

### 3.2.4 Image processing

To separately quantify the direct saturation of fat and water and the semi-solid MT effect, Z-Spectral data were first normalized to the reference signal at  $\pm 100$  ppm and then fitted to a model that consists of three Lorentzian functions representing the three different compartments (Fig. 3.1).

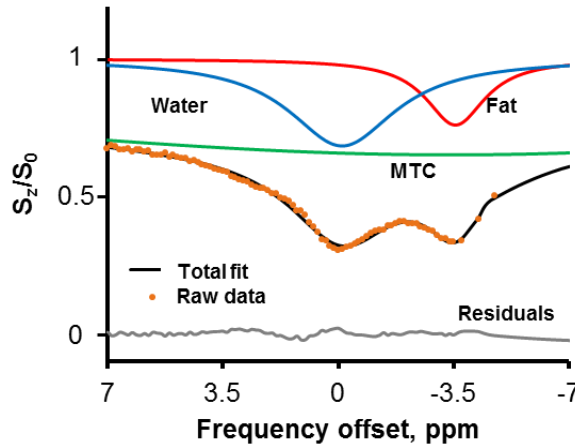


Figure 3-1 ZSI processing.

Z-Spectrum Imaging data are fitted to a multi-Lorentzian model including the peaks corresponding to water (cyan), fat (red) and MTC (green) pools. Total fit performance is good ( $R^2 > 0.98$ ) with residuals  $< 2\%$ .

The amplitudes of the water (W) and methylene-fat (F) peaks were used to compute the fat-water fraction as:

$$FWF = \frac{F}{F + W} \quad (17)$$

The pixelwise FWF value was used to produce color-coded FWF maps and overlapped onto  $T_2$ -weighted images for anatomical reference. To produce quantitative maps, a calibration was performed assuming  $FWF = 0.9$  in areas of pure fat and  $FWF = 0$  in lean tissue.

### 3.2.5 Statistical analysis

The FWF maps were evaluated based on *a priori* knowledge of BAT depots distribution and values were presented as mean  $\pm$  standard deviation and compared to results from previous published works.

Fit performance was assessed by both the correlation coefficient and the residuals between the fit and the raw data. Average values from regions of interest in subcutaneous white and interscapular or supraclavicular brown fat were presented. Differences between tissue types both *in vitro* and *in vivo* were assessed by Student's t-test and significance level was set to 0.05. Also, comparison to Dixon IDEAL fat water fraction was evaluated by t-tests in the human subjects.

## 3.3 Results

The Lorentzian fitting of a representative Z-Spectrum from *ex vivo* BAT tissue is shown in Fig. 3.1 with three peaks corresponding to fat, water and MTC. Z-Spectra were well fitted with an average  $R^2 > 0.981$  and residues  $< 2\%$ . Fig. 3.2a shows representative Z-Spectra from BAT, WAT, and lean tissue (muscle). Z-Spectra from the extracted tissues were characterized by two major peaks corresponding to the water and lipid direct saturation. Samples containing white fat showed predominantly the peak originating from the methylene protons at -3.5 ppm from the water resonance (set at 0 ppm), while lean tissue samples showed only the water peak. Interscapular BAT samples showed apparently larger water dip than WAT. Maps of fat-water fraction were obtained for the three samples, clearly showing the difference in relative fat content (Fig.3.2b).

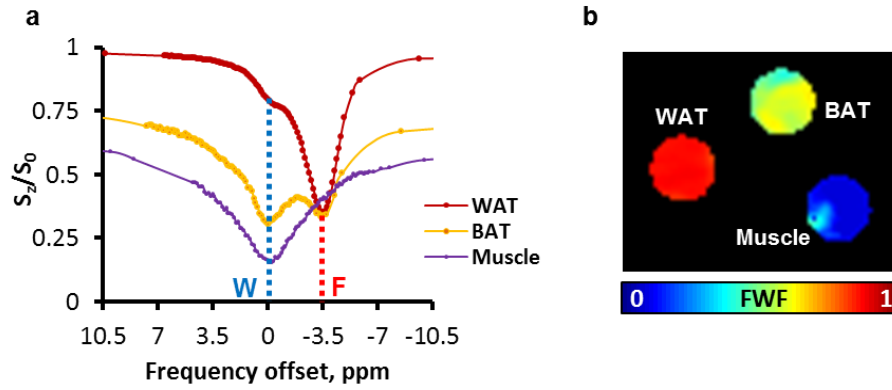


Figure 3-2 ZSI results from extracted mouse tissues.

Data are centered to water frequency. WAT and Muscle are characterized by either the fat or the water peak, while BAT shows a mixed contribution of both (a). Fat-water fraction can be derived from the fitted amplitudes in every pixel to produce colored maps (b). W: Water; F: Methylene-Fat.

In the calibration phantom, the oblique placement of the imaging plane resulted in a linear gradient of oil and water composition as shown on the  $T_2$ -weighted images (Fig. 3.3 a). As expected, FWF map derived from the Z-Spectral fitting showed the gradient of oil to water ratio across the oil-water interface (Fig. 3.3 b, c). The measured FWF values from the pixels crossing the oil-water interface were found to be linearly correlated to the actual fat water fraction ( $R^2=0.986$ ).

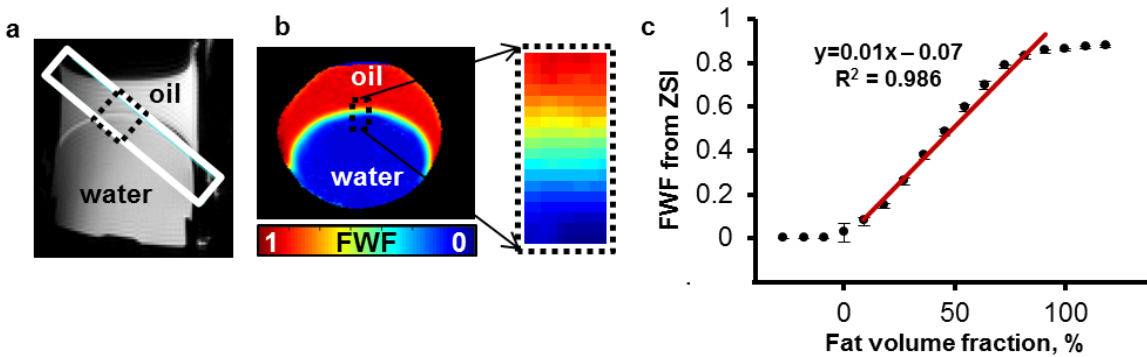


Figure 3-3 FWF calibration in phantom containing a mix of peanut oil and water.

(a)  $T_2$ -weighted image displaying the oblique slice placement. The interface area shows a gradual mix of fat and water within the slice. (b) FWF map of the slice shows a linear gradient across the interface (dotted black box). (c) FWF scales linearly with the estimated fat volume fraction in the interface area ( $R^2 = 0.986$ ).

*In vivo* data from healthy young mice confirmed the *in vitro* results. From the sagittal and axial T<sub>2</sub>-weighted images covering the central region of the fat depot, we can identify the triangular shaped subcutaneous WAT and the two underlying lobes of BAT, the largest known BAT depots in the interscapular region. The FWF maps computed from this area showed that BAT has lower levels of fat-water fraction than WAT. The fraction values were found comparable to what previously reported(14,29,30), ranging between 0.4 and 0.6 ( $0.54 \pm 0.08$ ) in the BAT lobes (Fig. 3.4b). The subcutaneous WAT identified on both T<sub>2</sub>-weighted and CEST images, instead, showed FWF values ranging from 0.7 to 0.9 ( $0.74 \pm 0.06$ ). Areas with predominantly lean tissues showed very low FWF (< 0.3). After calibration, values were corrected to  $0.62 \pm 0.10$  and  $0.82 \pm 0.04$  for BAT and WAT respectively (Fig. 3.4 c). As expected, t-tests revealed that FWF in BAT was significantly different ( $p < 0.004$ ) from WAT in all animals and in the specimens sets.

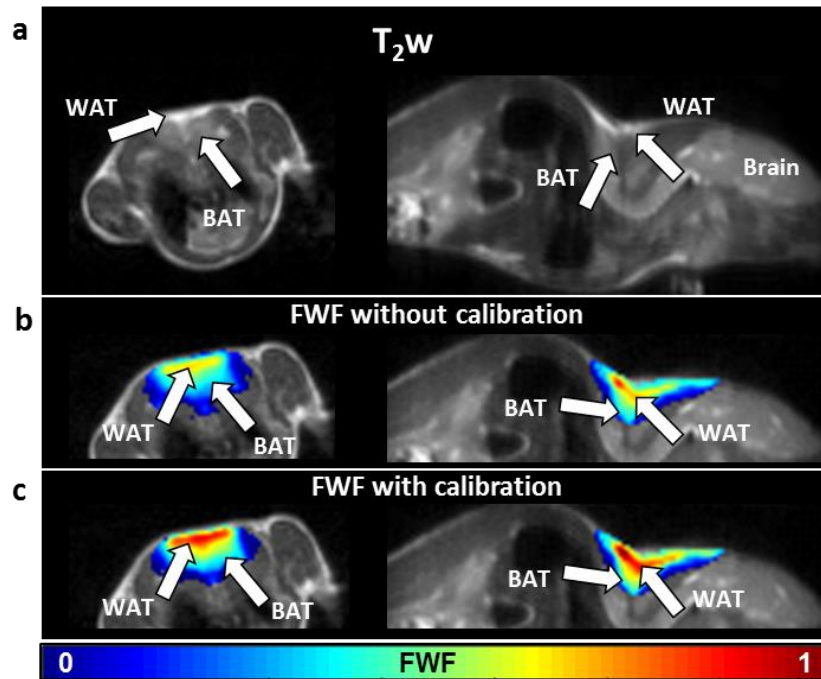


Figure 3-4 In vivo FWF heatmaps.

T<sub>2</sub>-weighted images from healthy male mice, showing location of the interscapular BAT depot with respect to the WAT layer, in axial (left) and sagittal (right) orientation (a). Fat-water fraction maps superimposed to the same anatomical references before (b) and after (c) calibration.

The human study further demonstrated the capability of ZSI to characterize BAT. FWF map of the supraclavicular area, site of active BAT depots in adult humans, showed a heterogeneous FWF distribution compared to the homogeneous subcutaneous fat in the torso, with FWF values of  $0.56 \pm 0.09$ , compared to  $0.72 \pm 0.04$  of WAT. In addition, we found a high agreement in FWF spatial distributions between values derived from Z-Spectrum data and those produced by the Dixon's method (Fig. 3.5 a,b). The agreement is further improved by the calibration performed using WAT from the torso and muscles as reference points (Fig. 3.5 c) resulting in no significant difference between the values evaluated in the ROIs ( $p > 0.07$ ). Fat-water fractions were  $0.63 \pm 0.07$  for BAT and  $0.83 \pm 0.05$  for WAT as evaluated by ZSI, while  $0.55 \pm 0.04$  and  $0.79 \pm 0.03$  as given by the Dixon MRI (Fig. 3.5 d). As expected, Dixon's method occasionally rendered fat-water switch artifacts caused by phase wrapping during the IDEAL reconstruction. The artifact can be visualized in the whole neck region (Figure 3.5 a, arrow), where a high fat fraction value is assigned to areas containing lean tissue. No such errors were observed in the colormap derived from the ZSI method (Figure 3.5 b).

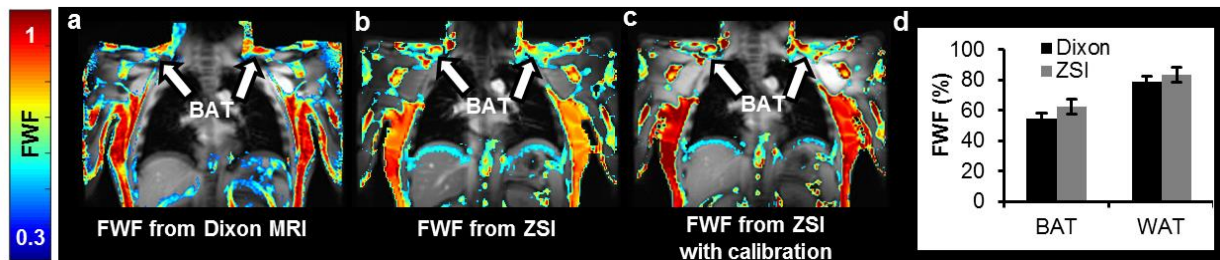


Figure 3-5 FWF in human subjects.

The protocol was tested at a clinical 3T scanner on healthy volunteers. FWF maps derived from Dixon MRI (a) and ZSI (b) show similar patterns. Similarity is further improved after calibration (c). Supraclavicular BAT depots (a-c, arrows) have lower fat content than the subcutaneous WAT. (d) No significant difference is assessed between the results from the two techniques in both brown and subcutaneous white fat.

### 3.4 Discussion

We demonstrated in this study with *in vitro* and *in vivo* experiments that Z-Spectral imaging can measure the fat-water fraction in tissues based on the direct saturation of both water and lipid signals, providing a tool to quantify brown adipose tissue mass.

Multi-point Dixon sequences with reconstruction algorithms like GE's IDEAL have been often used to measure fat and water signals for BAT detection and differentiation from white fat. However, up to 10% of routine scans are affected by fat-water swapping artifacts, due to algorithm's convergence to local minima in areas where phase is wrapped(16,17,31,32). The novel ZSI method is inherently insensitive to phase wrapping and field inhomogeneity issues. Z-Spectrum Imaging can provide the signal of each component alone through fitting, with no prior knowledge about the chemical shifts of either pool, producing  $B_0$ -insensitive fat-water fraction maps. For the same reason, ZSI is also independent from chemical shifts induced by environmental factors, like local susceptibility and temperature variations. Conventional multiecho sequences instead, rely on the assumption that the chemical shift between water and fat is constant and do not take into account such confounding factors(16,18).

It is also worthwhile to note that chemical shift encoded techniques (such as the Dixon's method) can suffer from  $T_2^*$  biases(29). In fact, the different signal losses between the in- and out-of-phase echoes due to varying TEs and hence  $T_2^*$  decays of water and fat can erroneously be attributed to phase cancellation and lead to an inaccurate quantification of FWF. Currently this effect has been reported only in cases of very short  $T_2^*$ , like in fatty livers with excessive iron(29), and the  $T_2^*$  impact on high vascularized BAT tissues remains to be explored. In any case, ZSI is carried out at the same TE for each frequency offset and is immune to  $T_2^*$  decay issues.

The calibration of the ZSI technique with oil and water phantoms revealed a linear relationship between the computed and actual FWF, allowing for a straightforward interpretation of quantitative results.

In the images, the transition area between the fluids appears curvilinear. This is likely caused by the fact that the oblique orientation of the imaging plane cuts through the interface in a cylindrical probe, but it is also due to the curvature induced by the different superficial tension in the two fluids at the interface. Nevertheless, the area where the transition is linear is clearly visible and extends for more than 10 pixels along the whole curve profile.

The same phantom design we used in the calibration was previously adopted by other influential studies(33). Such design provides a continuous range of fat water fraction from 0 to 100%, artificially created from the partial volume effect of oil present in an imaging slice obliquely crossing the oil-water interface. Given its starkly hydrophobic nature, oil doesn't mix with water naturally and it's challenging to obtain homogeneous mixtures with controlled ratios of the two species. Other groups addressed this limitation by using emulsifiers to bind oil molecules to water, and agar or other gelling agents to trap the emulsion in a stable phase(24,34). Although this approach can deliver satisfactory compounds at low fat fractions, it fails almost completely to produce stable mixture at increasing fat content (from FWF>50%)(24,35). Moreover, the mixing procedure during the gel cooling phase always entails the risk of creating air bubbles and inhomogeneous density distributions. Aware of this practical limitation, we opted for this imaging method relying on partial volume effect.

It must be noted, though, that the imaging device we produced is simply a simulation of the partial volume effect, not exactly a replica of the BAT structure at the cellular scale, which is characterized by a mixed composition of water and fat droplets within the cell. Nevertheless, this method allows us to validate and calibrate our technology for the quantification of FWF. Also, the calibration performed *in vitro* doesn't translate directly to the *in vivo* quantification given that the calibrated slope may change with tissue relaxation times and imaging parameters. Calibrations can nevertheless be easily established for any *in vivo* applications with only two required reference data points, for example by setting the FWF of subcutaneous WAT to 0.9 and muscle to 0, according to published results(35,36).

Similarly to the present study, other works used MR spectroscopy or spectroscopic imaging to measure FWF difference between BAT and WAT(35,37). Although the basic principles are similar, our approach has a number of advantages by providing higher spatial resolution and taking shorter acquisition time. While shorter than MRS methods, the acquisition time in ZSI is still the limiting factor when compared to Dixon MRI. However, fast imaging technologies are being increasingly applied to CEST techniques(38,39), and we foresee that reasonable scanning time will bridge 3D ZSI to wide clinical applications in the near future.

Another potential limitation is the use of a single peak to model the lipid compartment, which has been described by up to 9 small resonant groups(18,32,39). Even though the fitting of the methylene peak alone provided a reliable FWF quantification in this study, the inclusion of the smaller contributions in a Z-Spectrum acquired with a lower and shorter saturation pulse may reveal intriguing results about tissue lipid composition.

Other players can also contribute to the Z-Spectrum, like CEST effects from exchanging protons and Nuclear Overhauser Enhancement (NOE) effects from dipole-dipole interactions between semi-solid components and water. However, such contributions are expected to be small compared to the dominant direct saturation on water and fat signals. In fact, the current fitting is accurate enough to render negligible errors (<2%) across the entire Z-spectrum. Further investigation of these smaller components may be used to study the metabolism of fat tissues, which will be our future work.

The spatial resolution used in this study is not high and can be improved by increasing the matrix size during the signal short acquisition, without notably increasing the acquisition time. However, due to the sparse nature of BAT distribution, high resolution imaging is definitely beneficial while not critically important for the quantification of fat water fraction.

Finally, we decided not to study the correlation with a widespread technique like  $^{18}\text{F}$ FDG-PET. In fact, we already mentioned how PET may have biases in the detection of active BAT and is virtually insensitive to inactive BAT(11,12). In addition, we feel that the comparison of FWF data with fat fractions derived geometrically (in phantoms) or from Dixon MRI (*in vivo*) sufficiently validates the ZSI strategy. Nevertheless, we plan to further characterize the technique by including the aforementioned correlations and by increasing the sample size in future studies.

In conclusion, Z-Spectrum Imaging has been demonstrated in this study to be a potentially valuable tool in the measurement of brown fat mass *in vivo* in preclinical and clinical settings. Unlike other chemical shift based imaging methods, this novel technique is insensitive to imaging phase issues and field inhomogeneity. ZSI for the quantification of BAT may therefore serve as an important novel tool for the diagnosis and treatment of metabolic diseases.

### 3.5 Summary

Brown adipose tissue (BAT) has a great relevance in metabolic diseases and has been shown to be reduced in obesity and insulin resistance patients. Currently, Dixon MRI is used to calculate fat-water fraction (FWF) and differentiate BAT from white adipose tissue (WAT). However, it may fail in areas of phase wrapping and introduce fat-water swapping artifacts. The purpose in this study is therefore to investigate the capacity of the Z-Spectrum Imaging (ZSI) for the identification of BAT *in vivo*.

As a proof of concept, WAT, BAT and lean tissue from healthy mice were studied *ex vivo* on a 9.4T preclinical scanner. Four C57BL/6 healthy mice were then assessed *in vivo*, and finally 5 healthy volunteers were studied at 3T.

Z-Spectra data were fitted to a model with three Lorentzian peaks reflecting the direct saturation of tissue water (W) and methylene fat (F), and the magnetization transfer from the semi-solid tissues. The

peak amplitudes of water and fat were used to map the FWF. The novel FWF metric was calibrated with an oil and water mixture phantom and validated in specimens, mice and human subjects. FWF distribution was compared to published work and values compared to Dixon's MRI results. Comparisons were performed by t-tests.

ZSI clearly differentiated WAT, BAT, and lean tissues by having FWF=1, 0.5 and 0 respectively.

Calibration with oil mixture phantoms revealed a linear relationship between FWF and the actual fat fraction ( $R^2=0.98$ ). *In vivo* experiments in mice confirmed *in vitro* results by showing FWF=0.6 in BAT.

FWF maps of human subjects showed the same FWF distribution as Dixon's MRI ( $p>0.07$ ). ZSI is independent from  $B_0$  field inhomogeneity and fat-water swapping since both lipid and water frequency offsets are determined simultaneously during Z-Spectral fitting.

In conclusion, we demonstrated that ZSI can derive artifact-free FWF maps, which can be used to identify BAT distribution *in vivo* non-invasively.

## Bibliography

1. Rueggsegger GN, Booth FW. Running from disease: Molecular mechanisms associating dopamine and leptin signaling in the brain with physical inactivity, obesity, and type 2 diabetes. *Front Endocrinol (Lausanne)*. 2017;8(MAY):1–8.
2. Rajan T, Menon V. Psychiatric disorders and obesity: A review of association studies. *J Postgrad Med*. 2017;63(3):182.
3. Herrero L. Fatty acid metabolism and the basis of brown adipose tissue function. *Adipocyte*. 2016;5(2):98–118.
4. Chen Y, Pan R, Pfeifer A. Fat tissues , the brite and the dark sides. *Pflügers Arch - Eur J Physiol*. 2016;1803–7.
5. Nicholls DG. The hunt for the molecular mechanism of brown fat thermogenesis. *Biochimie*. 2016;1–10.
6. Cypess AM, Haft CR, Laughlin MR, Hu HH. Brown Fat in Humans: Consensus Points and Experimental Guidelines. *Cell Metab*. 2015;20(3):408–15.
7. Beijer E, Schoenmakers J, Vijgen G, Kessels F, Dingemans A, Schrauwen P, et al. A role of active brown adipose tissue in cancer cachexia ? *Oncol Rev*. 2012;6:88–94.
8. Trayhurn P. Origins and early development of the concept that brown adipose tissue thermogenesis is linked to energy balance and obesity. *Biochimie*. 2016;
9. Wu B, Warnock G, Zaiss M, Lin C, Chen M, Zhou Z, et al. An overview of CEST MRI for non-MR physicists. *EJNMMI Phys*. 2016;3(1):19.
10. Cristina T, Bargut L, Aguila MB, Mandarim-de-lacerda CA. Tissue and Cell Brown adipose tissue : Updates in cellular and molecular biology. *Tissue Cell*. 2016;48(5):452–60.
11. Abreu-vieira G, Hagberg CE, Spalding KL, Cannon B, Nedergaard J. Adrenergically stimulated blood flow in brown adipose tissue is not dependent on thermogenesis. *Am J Physiol Endocrinol Metab*. 2015;822–9.
12. Gifford A, Towse TF, Walker RC, Avison MJ, Welch EB, Gifford A, et al. Characterizing active and inactive brown adipose tissue in adult humans using PET-CT and MR imaging. *Am J Physiol Endocrinol Metab*. 2016;i(2):95–104.
13. Chen Y, Pan R, Pfeifer A. Fat tissues , the brite and the dark sides. *Pflügers Arch - Eur J Physiol*. 2016;1803–7.
14. Hu HH, Jr. DLS, Nayak KS, Goran MI, Nagy TR. Identification of Brown Adipose Tissue in Mice with Fat-Water IDEAL-MRI. *J Magn Reson Imaging*. 2010;31(5):1195–202.
15. Hamilton G, Jr. DLS, Bydder M, Nayak KS, Hu HH. Magnetic resonance properties of brown and white adipose tissues. *J Magn Reson Imaging*. 2012;34(2):468–73.

16. Bley TA, Wieben O, Francois CJ, Brittain JH, Reeder SB. Fat and water magnetic resonance imaging. *J Magn Reson Imaging*. 2010;31(1):4–18.
17. Ladefoged CN, Hansen AE, Keller SH, Holm S, Law I, Beyer T, et al. Impact of incorrect tissue classification in Dixon-based MR-AC: fat-water tissue inversion. *EJNMMI Phys*. 2014;1(1):101.
18. Yu H, Shimakawa A, Hines CDG, McKenzie CA, Hamilton G, Sirlin CB, et al. Combination of Complex-Based and Magnitude-Based Multiecho Water-Fat Separation for Accurate Quantification of Fat-Fraction. *MRM*. 2012;66(1):199–206.
19. Glover GH. Multipoint Dixon Technique for Water and Fat Proton and Susceptibility Imaging. *JMRI*. 1991;1:521–30.
20. Branca RT, Zhang L, Warren WS, Auerbach E, Khanna A, Degan S, et al. In Vivo Noninvasive Detection of Brown Adipose Tissue through Intermolecular Zero-Quantum MRI. *PLoS One*. 2013;8(9).
21. Branca RT, He T, Zhang L, Floyd CS, Freeman M, White C, et al. Detection of brown adipose tissue and thermogenic activity in mice by hyperpolarized xenon MRI. *Proc Natl Acad Sci*. 2014;111(50):18001–6.
22. Grad J, Bryant RG. Nuclear magnetic cross-relaxation spectroscopy. *J Magn Reson*. 1990;90(1):1–8.
23. Ward KM, Aletras AH, Balaban RS. A new class of contrast agents for MRI based on proton chemical exchange dependent saturation transfer (CEST). *J Magn Reson*. 2000;143(1):79–87.
24. Holmes JH, Johnson KM, Hernando D, Reeder SB, Samsonov A. Magnetization transfer ratio ( MTR ) imaging in the presence of fat. In: *Intl Soc Mag Reson Med*. 2015. p. 100651.
25. Lunati E, Farace P, Nicolato E, Righetti C, Marzola P, Sbarbati A, et al. Polyunsaturated Fatty Acids Mapping by 1 H MR-Chemical Shift Imaging. *Magn Reson Med*. 2001;883:879–83.
26. Kim M, Gillen J, Landman BA, Zhou J, Peter CM. WAter Saturation Shift Referencing (WASSR) for chemical Exchange Saturation Transfer Experiments. 2010;61(6):1441–50.
27. Lilburn DML, Cooper AS, Murphy P, Sinclair CDJ, Semple SI, Janiczek RL. Initial experience using Magnetization Transfer with Iterative Decomposition of water and fat with Echo Asymmetry and Least-squares estimation ( MT-IDEAL ) in the abdomen . In: *Intl Soc Mag Reson Med*. 2015. p. 1744.
28. Healthcare GE. Discovery TM MR750, a 3.0T system. Tech data. 2009;
29. Hu HH, Hines CDG, Smith Jr DL, Reeder SB. Variations in T2\* and Fat Content of Murine Brown and White Adipose Tissues by Chemical-Shift MRI. *MRM*. 2013;30(3):323–9.
30. Prakash KNB, Srour H, Velan SS, Hsiang-Kai C. A method for the automatic segmentation of brown adipose tissue. *Magn Reson Mater Physics, Biol Med*. 2016;29(2):287–99.
31. Reeder SB, Wen Z, Yu H, Pineda AR, Gold GE, Markl M, et al. Multicoil Dixon Chemical Species Separation With an Iterative Least-Squares Estimation Method. *Magn Reson Med*. 2004;45(July 2003):35–45.

32. Ma J. Dixon Techniques for Water and Fat Imaging. *JMRI*. 2008;558:543–58.
33. Fuller S, Reeder S, Shimakawa A, Yu H, Johnson J, Beaulieu C, et al. Iterative decomposition of water and fat with echo asymmetry and least-squares estimation (IDEAL) fat spin-echo imaging of the ankle: Initial clinical experience. *Am J Roentgenol*. 2006;187(6):1442–7.
34. Qiang G, Kong HW, Xu S, Pham HA, Parlee SD, Burr AA, et al. Lipodystrophy and severe metabolic dysfunction in mice with adipose tissue-specific insulin receptor ablation. *Mol Metab*. 2016;5(7):480–90.
35. Peng X, Ju S, Fang F, Wang Y, Fang K, Cui X, et al. Comparison of brown and white adipose tissue fat fractions in ob, seipin, and Fsp27 gene knockout mice by chemical shift-selective imaging and <sup>1</sup>H-MR spectroscopy. *Am J Physiol Endocrinol Metab*. 2013;(30):160–7.
36. Zhang Q, Kuang H, Chen C, Yan J, Do-umehara HC, Dada L, et al. Highly-accelerated CEST Measurements in Three Dimensions with Linear Algebraic Modeling. *Proc Intl Soc Mag Reson Med* 24. 2015;16(5):458–66.
37. Boesch C, Machann J, Vermathen P, Schick F. Role of proton MR for the study of muscle lipid metabolism. *NMR Biomed*. 2006;(2):968–88.
38. Dixon WT, Hancu I, Ratnakar SJ, Sherry AD, Robert E, Alsop DC. A Multislice Gradient Echo Pulse Sequence for CEST Imaging. *Magn Reson Med*. 2010;63(1):253–6.
39. Hines CDG, Yu H, Shimakawa A, McKenzie CA, Brittain JH, Reeder SB. T1 independent, T2\* corrected MRI with accurate spectral modeling for quantification of fat: Validation in a fat-water-SPIO phantom. *J Magn Reson Imaging*. 2009;30(5):1215–22.

#### 4. CHARACTERIZATION OF BROWN ADIPOSE TISSUE (BAT) IN POLYCYSTIC OVARY SYNDROME (PCOS) PATIENTS BY Z-SPECTRUM IMAGING (ZSI)

(Previously published as: Li L, Scotti A, Fang J, Yin L, Xiong T, He W, Qin Y, Liew C, Khayyat N, Zhu W, Cai K. Characterization of brown adipose tissue (BAT) in polycystic ovary syndrome (PCOS) patients by Z-Spectral Imaging (ZSI). Eur J Radiol. 2020 Feb; 123:108777.)

##### 4.1 Introduction

Polycystic ovary syndrome (PCOS) is a common reproductive female disorder which can affect women's health during different stages of reproductive and post-reproductive life. The worldwide occurrence of PCOS ranges from 6 % to 21 % according to the ESHRE/ASRM 2003 criteria [1]. PCOS is frequently associated with several metabolic consequences [2, 3], although the mechanism underlying this association is still not clear [4]. A majority of patients with PCOS demonstrate obesity, abdominal adiposity, and chronic insulin resistance. As a result of their insulin resistance and suboptimal compensatory hyperinsulinemia, patients with PCOS are at increased risk for metabolic syndrome, type 2 diabetes mellitus and cardiovascular disease [2, 3]. In the study of metabolic disorders, researchers have recently focused on brown adipose tissue (BAT), a subtype of fat that can affect the whole-body metabolism by producing heat to improve glucose tolerance, increase insulin sensitivity, and promote weight loss [5]. Given that the majority of patients with PCOS demonstrate obesity and chronic insulin resistance [2, 3], and the loss of the weight in PCOS patients is associated with the resumption of ovulation [6], the relationship between PCOS and BAT can potentially carry insight of the treatment of PCOS.  $^{18}\text{F}$ -FDG PET/CT scanning is the most commonly used non-invasive method for determining the presence of active BAT in humans, relying on the glucose uptake in the activated state of BAT. PET/CT-based BAT analysis has recently been challenged [7,8]. Fundamentally, the precise correlation between  $^{18}\text{F}$ -FDG uptake and BAT thermogenesis is not fully validated [8–10]. It has been shown that  $^{18}\text{F}$ -FDG

uptake is fully maintained even when BAT thermogenesis are diminished, suggesting that increased BAT  $^{18}\text{F}$ -FDG uptake may occur independently of thermal function at least in some instances [11, 12]. The other limitation for PET/CT imaging is the radiation exposure, preventing frequent longitudinal examinations [13, 14]. Therefore, alternative approaches are desirable. To date, conventional and novel MRI techniques [15–20] have been used to detect BAT mass. Due to relatively reduced fat content in BAT compared to white adipose tissues (WAT) [21], fat-water fraction (FWF) has emerged as a natural biomarker for the detection of BAT [7,22, 23]. Dixon MRI and Z-spectral imaging (ZSI) have been used to calculate the FWF and detect BAT in vivo, with the latter overcoming the inherent sensitivity to phase artifacts due to direct saturation of both water and fat signals [22]. In addition, the image processing for ZSI quantification of FWF is relatively simple. In this study, therefore, we aimed to characterize BAT mass and function in PCOS by using ZSI.

## 4.2. Materials and methods

### 4.2.1. Subjects

The study was performed with approved IRB protocols and all subjects signed informed consent. The study included 3 groups of subjects: 1) 19 healthy female controls (NCF), between 24–34 years old with normal ovulation (BMI:  $20.24 \pm 1.90$ ). 2) 17 healthy male controls (NCM), between 22–35years old (BMI:  $22.58 \pm 1.57$ ). 3) 13 female patients with polycystic ovary syndrome (PCOS), between 20–33years old (BMI:  $25.76 \pm 3.64$ ). The exclusion criteria of the three groups were 1) if subjects have systemic diseases (hyperthyroidism or hypothyroidism, hypertension, diabetes, cancer, or acute infection); 2) if subjects have medication history (taking  $\beta$ -blockers, antidepressants, oral contraceptives and drug abuse history) and history of surgery and drug allergy. On the other hand, the inclusion criteria for PCOS [1] were 1) if patients meeting two or more of the following criteria: scanty menstruation or anovulation,

hyperandrogenism, ovarian morphological changes based on ultrasound (12 or more small follicles in one or two ovaries, or ovarian volume greater than 10 cm<sup>3</sup>); 2) if ovulation disorders or hyperandrogenism were not caused by other diseases; 3) The patients did not take any medications. Some biological and physiological information were also collected from subjects including general conditions (history of smoking and drinking, and exercise intensity) and physical examinations (heart rate, blood pressure). Also, there are additional information collected for the PCOS subjects, including hematology results (blood glucose and insulin concentrations in oral glucose tolerance test (OGTT)) for the determination of insulin resistance [24] and serum hormone levels for hyperandrogenism [25].

#### 4.2.2. Imaging protocols

MRI scans were performed using a 3 T MR scanning system (GE Discovery MR 750; GE Healthcare, Waukesha, WI, USA) with a 32-channel torso coil. All the scans were completed before 1 pm of the examining day in winter time (January - April) and the temperature in the scanner was maintained at 18 °C to narrow the BAT differences caused by time changes. All the subjects wear the hospital gown to standardize the clothing condition, and they had breakfast 2 h to being not fasted and did not have smoking or caffeine intake for 2 days before the scan. All NCF subjects were scanned within 1–2 days after the menstrual period when metabolic rate is stable [26]. T<sub>2</sub>-weighted coronal anatomical body images were acquired as follow: fast spin echo (FSE) sequence with repetition time (TR) of 4 sand echo time (TE) of 85 ms, matrix size of 320 × 224, field of view (FOV) of 46 × 46 cm<sup>2</sup>, and slice thickness of 5 mm. Single-slice ZSI data was then acquired on the optimal BAT coronal section in the supraclavicular area. The slice selection was based on the T<sub>2</sub>-weighted images. The pre-saturation pulse of the ZSI sequence consisted of a train of 4 saturation pulses with magnitude of 0.94μT, 50 ms each, resulting in a total saturation duration of 200 ms, followed by a single-shot fast spin echo (FSE) readout with parameters: slice thickness =5 mm, TR = 6 s, TE = 2.7 ms, FOV = 46 × 46 cm<sup>2</sup>, and matrix size = 128 ×128. ZSI images were collected at 43 pre-saturation frequencies from -5 to 5 ppm with 0.25 ppm intervals and

+100 ppm for signal normalization. The total acquisition time for collecting the ZSI data was 4 min and 25 s. In addition, a 6-point Dixon MRI with the commercial GE version (IDEAL IQ) reconstruction was performed using parameters  $TE_1 = 1.3$  ms,  $\Delta TE = 2.0$  ms,  $TR = 7.3$  s, and matrix size =  $160 \times 160$ .

#### 4.2.3 Image processing

The collected Z-spectra contain information for the direct saturation of fat and water. To separately quantify these components, Z-spectra were first normalized to the reference signal at +100 ppm and then fitted to a model consisting of multiple Lorentzian functions representing the different compartments. For the fat components [22, 23], 6 Lorentzian functions were prescribed with offsets tightly constrained to the main methylene peak location (-3.4 ppm from water resonance). The lipid offsets are -3.8 ppm, -3.4 ppm, -2.67 ppm, -1.93 ppm, -0.5 ppm and 0.61 ppm, respectively. The amplitudes of the fitted water (W) dip and the main methylene-fat (F) dip were used to compute the fat-water fraction as  $FWF = F / (F + W)$ . The pixel-wise FWF value was used to produce color-coded FWF maps which were then overlapped onto the raw ZSI images. All the tissue within the manually-drawn supraclavicular area was then classified as WAT, BAT, or muscle based on FWF thresholds determined as described below. The histogram distribution of FWF from the supraclavicular region of interest was created. In reference to our preview study [22] and other studies [7, 23], the FWF distribution with the highest FWF represented WAT, with FWF ranging from 0.7 to 1. The FWF distribution with lowest FWF values ( $FWF < 0.4$ ) represented muscle, and the midlevel distribution was considered to be BAT. Based on these thresholds, three separated masks were generated corresponding to WAT, BAT, and muscle. Two major parameters were quantified: BAT fraction ( $BATf$ ), defined as the normalized area of BAT over the total fat (Eq. 19) and the average FWF value within BAT area or  $FWF(BAT)$  (Eq. 20),

$$BATf = \frac{BAT}{BAT + WAT} \quad (18)$$

$$FWF(BAT) = \frac{\sum_1^n FWF_i}{n} \quad (19)$$

Where  $FWF_i$  represents the pixel-wise FWF value within the BAT segmentation and  $n$  represents the total number of BAT pixels.

#### 4.2.4. Statistical analysis

Differences among the parameters ( $BATf$  and  $FWF(BAT)$ ) in the three groups were evaluated by Student's t-test and the statistical significance was prescribed if  $p < 0.05$ . For the comparison analysis among the three groups, 3 subjects from the NCM group were excluded because their BMI was larger than 25 (overweight). The correlations between  $BATf$  and the BMI,  $FWF(BAT)$  and the BMI in the three groups were also examined based on linear regressions by ANOVA test. Results were presented as mean  $\pm$  standard deviation. Statistical analyses were all performed with the statistics software package SPSS (IBM, ver. 23.0).

### 4.3 Results

There was no statistical difference in the age, history of smoking/drinking, exercise intensity, and physical examination among the three study groups. However, there was significant difference in the BMI between the NCF ( $20.0 \pm 5.6$ ) and NCM ( $22.6 \pm 6.9$ ) groups ( $P = 0.001$ ) and between the NCF and the PCOS ( $25.76 \pm 3.64$ ) group ( $P < 0.001$ ). The hematology results for the NCF and NCM were within norm ranges, while all the patients in the PCOS group showed hyperandrogenism and insulin resistance ( $HOMA-IR = 5.47 \pm 2.21$ ). Representative ZSI data from BAT, WAT, and muscle ROIs are fitted to a multi-Lorentzian model including the dips corresponding to the direct saturation of water and multiple fat components (Fig. 4.1).

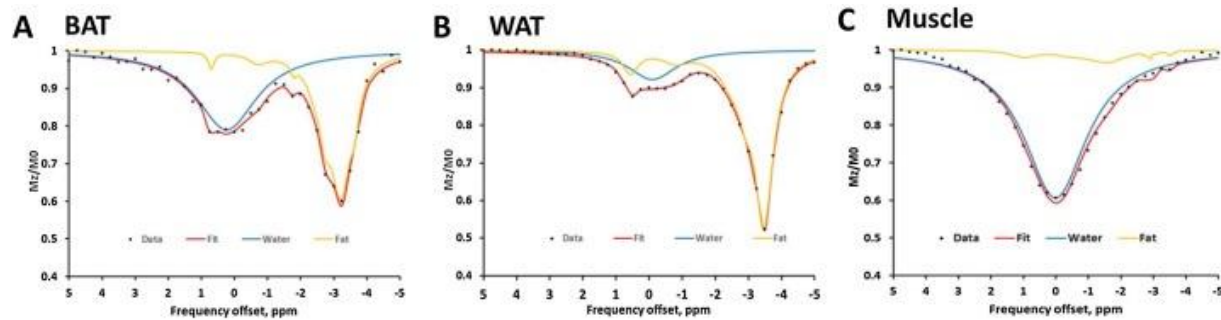


Figure 4-1 Z-Spectral imaging data.

Representative ROIs spectra of BAT (A), WAT (B), and muscle (C) are fitted to a multi-Lorentzian functions corresponding to the direct saturation of water (blue) and fat peaks (yellow).

There were multi-fat peaks and a water peak in the Z-spectra of BAT, while there were higher multi-FAT peaks but lower water peak in WAT. And, there were a broadest and deepest water peaks and small FAT peaks in muscle. The total fit performance is good ( $R^2 > 0.98$ ) with residuals  $< 2\%$ . Pixel-wise FWF was calculated with the fitted amplitude of the direct saturation of water and the main lipid component centered at -3.4 ppm from water as demonstrated in Fig. 4.2B. Although the absolute scaling was slightly different, there is high agreement found in FWF spatial distributions in the FWF maps derived from ZSI data and those produced by the Dixon's method (Fig. 4.2B&C), consistent to our previous report [22]. A representative histogram distribution of pixel-wise FWF values quantified with ZSI from the supraclavicular region of interest was showed in Fig. 4.2D. With the FWF thresholds, the supraclavicular tissue (Fig. 4.2E) was segmented as WAT, BAT or muscle (Fig. 4.2F–H).

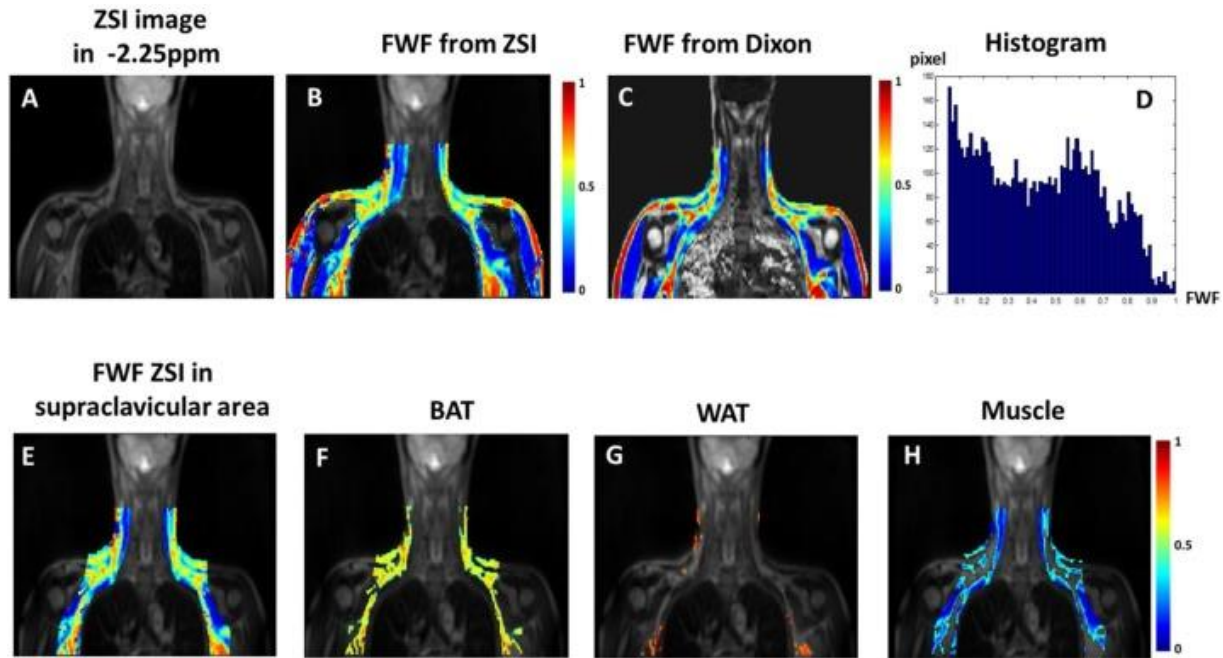


Figure 4-2 FWF analysis.

A) An anatomical ZSI image collected at -2.25 ppm. B) The color-coded FWF map produced from ZSI. C) The color-coded FWF map produced from Dixon's method. D) The histogram of pixel FWF values calculated with ZSI analysis from image B. E) ZSI FWF map of the manually-drawn supraclavicular area were segmented into BAT (F), WAT (G) and muscle (H) maps.

#### 4.3.1 The correlation between BATf, FWF(BAT) and BMI

The correlations between the  $BATf$ ,  $FWF(BAT)$  and the BMI for all subject groups are shown in Fig. 4.3.

In the NCM group, there was an obviously linear correlation between the  $BATf$  and BMI ( $R^2=0.7748$ ,  $P < 0.001$ ), and between the  $FWF(BAT)$  and BMI ( $R^2=0.3219$ ,  $P < 0.05$ ). Correlation for  $BATf$  ( $R^2=0.2549$ ,  $P < 0.05$ ) was showed in the NCF group, while there was no linear correlation between the  $FWF(BAT)$  and BMI ( $P > 0.05$ ). Interestingly, no correlation was found in the PCOS group between  $BATf$  and BMI, the  $FWF(BAT)$  and BMI ( $P > 0.05$ ).

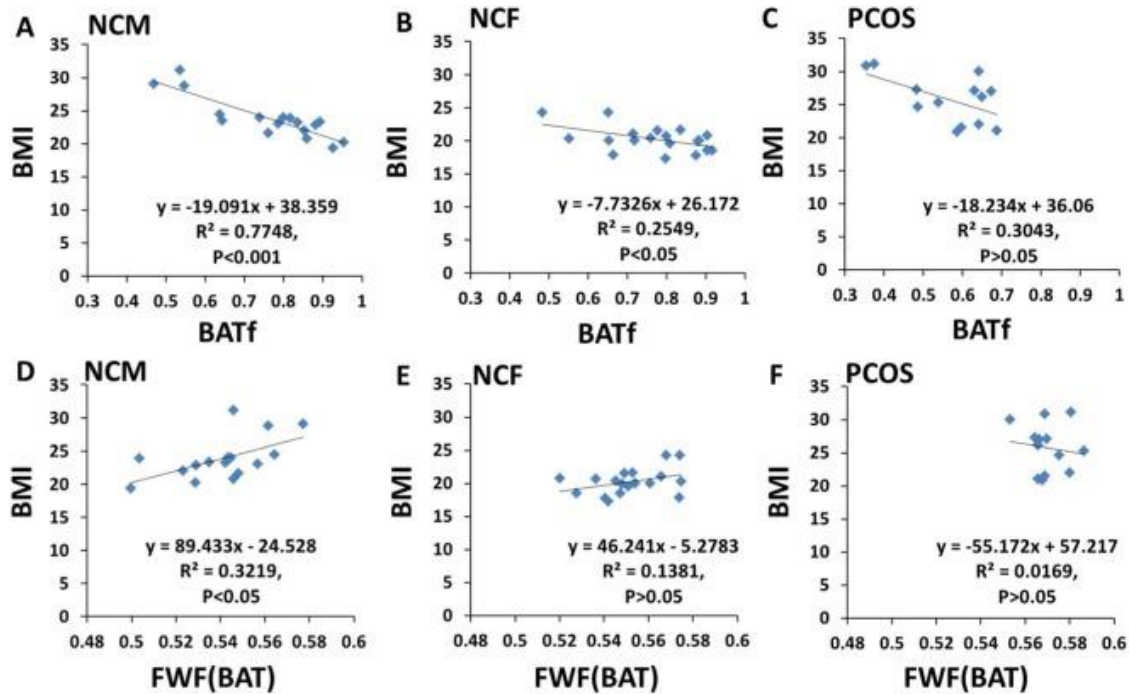


Figure 4-3 Correlations between ZSI parameters and BMI.

The correlation analysis between BATf and BMI (A, B, C) and between FWF(BAT) and BMI (D, E, F) for the subjects in the three groups.

#### 4.3.2. Comparison of group *BATf* and *FWF(BAT)*

The BAT, WAT and muscle maps were compared directly to show the distributions in the three groups (Fig. 4). The subject in NCM group had most “muscle” and least “WAT”, while the subject in PCOS group had least “muscle” and most “WAT”. However, the subject in NCF group had more content of BAT than the subjects in NCM and PCOS groups. Due to the individual differences of the subjects in the three groups, the comparisons of *BATf* and *FWF(BAT)* among the different groups are summarized in Fig. 4.5.

The average *BATf* in the PCOS group ( $0.5651 \pm 0.1102$ ) was found significantly lower than the NCF group ( $0.7671 \pm 0.1238$ ,  $P = 0.00005$ ), while there was no significant difference ( $P = 0.252$ ) between the NCF group and the NCM group ( $0.8134 \pm 0.0946$ ). As for the *FWF(BAT)*, the mean value in BAT of the PCOS

group ( $0.5702 \pm 0.0086$ ) was significantly higher than the NCF group ( $0.5518 \pm 0.0152$ ,  $P = 0.0005$ ), while the mean value in the NCF group was higher than the NCM group ( $0.5363 \pm 0.0182$ ,  $P = 0.01$ ).

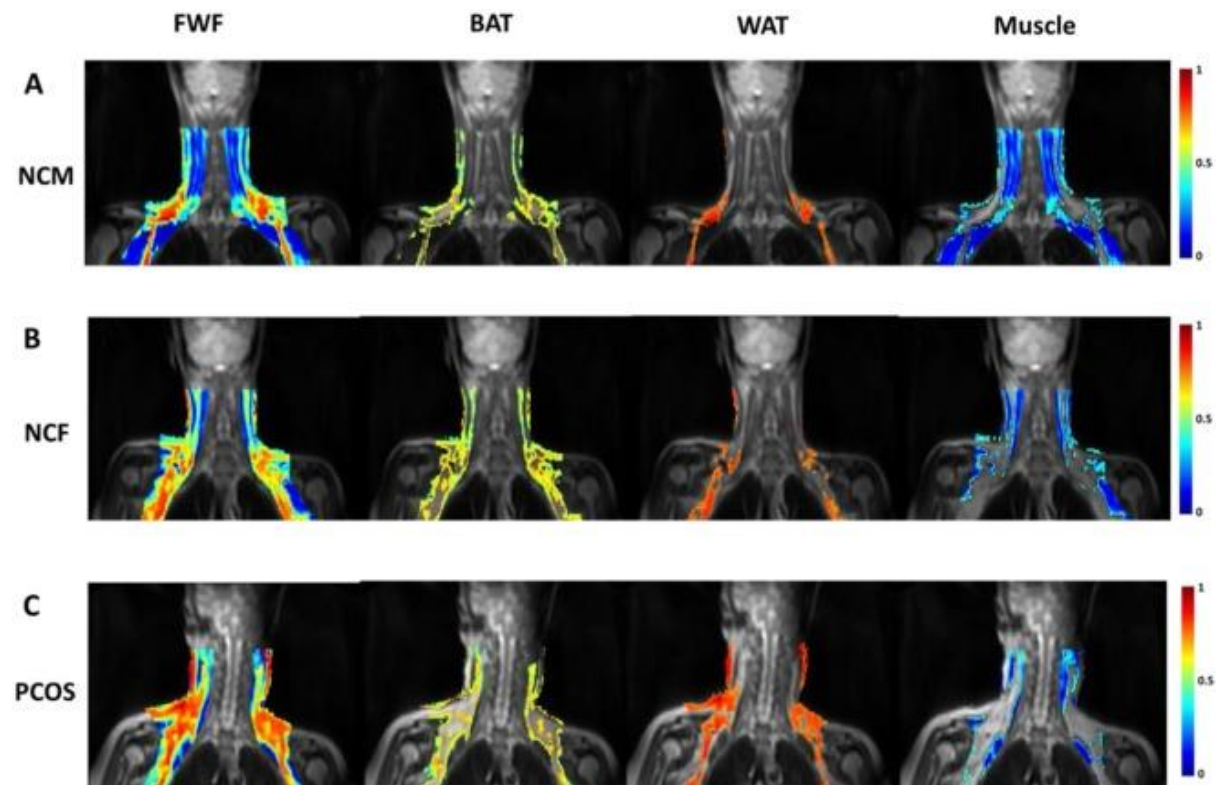


Figure 4-4 FWF segmentation. Representative maps of FWF, BAT, WAT, and muscle segmentations from NCM (A), NCF (B), and PCOS (C) subjects.

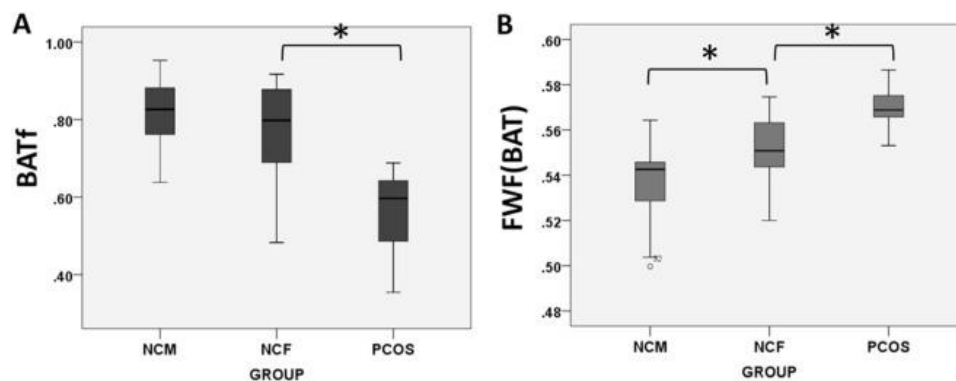


Figure 4-5 Comparisons of group averages. Significant differences ( $*P < 0.05$ ) were found between PCOS and controls in BATf (A) and FWF(BAT) (B).

## 4.4 Discussion

In this study, we have characterized BAT in PCOS patients and compared with healthy subjects using a novel ZSI MR technique. PCOS and metabolic syndrome are highly associated with each other, and BAT is considered to a new and promising target for the treatment of metabolic diseases. Therefore, the characterization of BAT in PCOS with ZSI may help to monitor responses of the treatments targeting PCOS syndromes, facilitating the development of new therapies for PCOS. As a novel imaging technique, ZSI allows the quantification of BAT in human subjects by providing comparable FWF maps with the conventional Dixon's method. With the analysis of ZSI data, two important parameters were produced. One is the  $BATf$ , which shows the ratio of BAT mass over the whole fat tissue. It is essentially a relative measurement of BAT mass. It is a better index for BAT mass than BAT area itself given that the normalization to total fat area helps to minimize inter-subject variability and any other possible variations due to imaging setups and RF transmission and receiving. PCOS group showed significantly lower  $BATf$ , indicating relatively reduced BAT mass or increased WAT in PCOS patients. Given that BAT is metabolically beneficiary, reduced BAT in PCOS confirmed that PCOS patients have metabolic disorders. Another important parameter provided by ZSI is the  $FWF(BAT)$ , the mean FWF value in the BAT tissue, essentially the relative fat content in the BAT tissue.  $FWF(BAT)$  is a parameter that reflects BAT activity given that the fat content is reduced in brown fat cells proportionally to cellular metabolism as reported early [27]. Prolonged activation of BAT cells led to reduced fat deposition in cells due to the consumption of free fatty acids into heat, the non-shivering thermogenesis process. On the other hand, insufficient stimulation of BAT increases lipid deposition within brown adipocytes as it has been observed in obese subjects [28]. Therefore, the smaller the  $FWF(BAT)$ , the higher the activities of BAT mass. PCOS patients have the highest  $FWF(BAT)$  level compared to healthy female and male controls, indicated their BAT mass have the least activity level. Recently, a cutaneous temperature measurement [29] of the supraclavicular skin was used to explored BAT thermogenesis and its associations in women

with and without PCOS, suggested that women with PCOS have lower BAT activity compared to controls, which is consistent with our in vivo result with novel method. We believe that insulin resistance associated with PCOS patients [5] may lead to the reduced activity in BAT mass. Such hypothesis needs further investigation. PCOS animal models [30] may help to study the underlying mechanism.

Furthermore, there were negative linear correlations between  $BATf$  and BMI in the normal subjects (NCM & NCF), which indicated that normal subjects with higher BMI had relatively lower level of metabolic beneficial BAT depot but higher level of metabolic passive WAT depot. On the other hand, normal subjects with higher BMI also have increased  $FWF(BAT)$ , indicating relatively increased lipid content and reduced metabolism in their BAT depots. This is in consistent to literature. Cypess [5] and other researchers [10, 23, and 31] also found that BMI was a predictor of the presence and the activity of BAT mass. Interestingly, we found that  $BATf$  and  $FWF(BAT)$  of PCOS patients did not correlate with BMI, which indicated that the BAT mass and the activity were affected by PCOS pathology. Our results also seem to indicate the difference on BAT function between normal non-obese male and female subjects. While the  $BATf$  was the same between normal male and female subjects, the subjects in NCF group had higher  $FWF(BAT)$  level compared to the male subjects, indicating that BAT in females may have lower activity level. The difference of BAT mass and function between male and female is still under debating. Some previous  $^{18}\text{F}$ -FDG PET/CT studies [5, 9, 31, 32] showing higher prevalence of BAT in women than in men under thermo-neutral conditions. However, Saito [11] and Yoneshiro [12] recently found no gender difference in BAT prevalence with a controlled cooling protocol by  $^{18}\text{F}$ -FDG PET/CT. This inconsistency may due to the variations in acquisition and quantification methods. On the other hand, it also reflects that the measurement of BAT mass and function with  $^{18}\text{F}$ -FDG PET/CT is still a challenge. The glucose-uptake activity measured by  $^{18}\text{F}$ -FDG-detected BAT can be influenced by many other factors, including partial volume effects and normalization of SUV to body weight [9,10 11, and 14]. In addition, the direct correlation between BAT thermogenesis and  $^{18}\text{F}$ -FDG uptake is still

questionable [11]. Given that the difference on BAT mass and function between genders is still not clear, more systematic studies on the effects of sex steroids [33] or other biochemical factors on BAT mass are needed in the future. The limitation of this study is that the BMI of the PCOS patients were not matched with that of the control female subjects given that PCOS patients are typically overweighted. With more subjects to be recruited for this study in the future particularly those healthy females with relatively large BMI, we could perform BMI-matched comparison between PCOS and healthy subjects to better control for any bodyweight induced confounding factors.

In conclusion, we found that BAT mass and functional variations are associated with PCOS patients. Therapies targeting to BAT may provide new insight for the treatment of PCOS syndrome. Novel imaging techniques with ZSI for the quantification of BAT mass and function may help to monitor treatment responses of PCOS therapies, facilitating new treatment development for PCOS patients.

## 4.5 Summary

The purpose of the study was to characterize brown adipose tissue (BAT) in polycystic ovary syndrome (PCOS) patients in comparison to healthy subjects using Z-spectral imaging (ZSI).

ZSI data were collected on 19 normal control females (NCF), 17 males (NCM), and 13 PCOS patients. By fitting to multiple Lorentzian functions, ZSI provides fat-water fraction (FWF) of tissue in the supraclavicular area that can be used to differentiate between white adipose tissue (WAT), BAT, and muscle. The fraction of BAT over the total fat depot ( $BAT_f$ ) and the average FWF in BAT or  $FWF(BAT)$  were then computed, reflecting relative BAT mass and BAT metabolism respectively. The parameters were compared among the three groups, and the correlations to Body Mass Index (BMI) were also quantified.

We found an inverse correlation between  $BATf$  and BMI in normal subjects. The  $BATf$  of the PCOS group was significantly smaller than the NCF ( $P < 0.001$ ). On the other hand,  $FWF(BAT)$  correlated linearly with BMI in healthy subjects. The PCOS group had higher  $FWF(BAT)$  than the NCF group ( $P < 0.001$ ).

In summary, normal subjects with higher BMI show less  $BATf$  and have increased  $FWF(BAT)$ , indicating relatively higher level of metabolic passive WAT depot and relatively reduced metabolism in their BAT depots. PCOS patients have the least  $BATf$  and the highest  $FWF(BAT)$ , suggesting decreased BAT mass and function in PCOS. Novel imaging technique with ZSI for the characterization of BAT mass and function in PCOS may help to monitor treatment responses of PCOS therapies.

## Bibliography

- [1] Revised 2003 consensus on diagnostic criteria and long-term health risks related to polycystic ovary syndrome (PCOS), *Hum. Reprod.* 19 (1) (2004) 41–47.
- [2] R. Azziz, Polycystic ovary syndrome, *Obstet. Gynecol.* 132 (2) (2018) 321–336, <https://doi.org/10.1097/AOG.0000000000002698>.
- [3] H.F. Escobar-Morreale, Polycystic ovary syndrome: definition, aetiology, diagnosis and treatment, *Nat. Rev. Endocrinol.* 14 (5) (2018) 270–284, <https://doi.org/10.1038/nrendo.2018.24>.
- [4] D. Lizneva, L. Suturina, W. Walker, et al., Criteria, prevalence, and phenotypes of polycystic ovary syndrome, *Fertil. Steril.* 106 (1) (2016) 6–15, <https://doi.org/10.1016/j.fertnstert.2016.05.003>.
- [5] A.M. Cypess, S. Lehman, G. Williams, et al., Identification and importance of brown adipose tissue in adult humans, *N. Engl. J. Med.* 360 (15) (2009) 1509–1517, <https://doi.org/10.1056/NEJMoa0810780>.
- [6] C.J. Glueck, N. Goldenberg, Characteristics of obesity in polycystic ovary syndrome: etiology, treatment, and genetics, *Metabolism* (2018), <https://doi.org/10.1016/j.metabol.2018.11.002>.
- [7] H.H. Hu, D.L. Smith, K.S. Nayak, et al., Identification of brown adipose tissue in mice with fat-water IDEAL-MRI, *J. Magn. Reson. Imaging* 31 (5) (2010) 1195–1202, <https://doi.org/10.1002/jmri.22162>.
- [8] L. Sun, J. Yan, L. Sun, et al., A synopsis of brown adipose tissue imaging modalities for clinical research, *Diabetes Metab.* 43 (5) (2017) 401–410, <https://doi.org/10.1016/j.diabet.2017.03.008>.
- [9] V. Ouellet, A. Routhier-Labadie, W. Bellemare, et al., Outdoor temperature, age, sex, body mass index, and diabetic status determine the prevalence, mass, and glucose-uptake activity of  $^{18}\text{F}$ -FDG-detected BAT in humans, *J. Clin. Endocrinol. Metab.* 96 (1) (2011) 192–199, <https://doi.org/10.1210/jc.2010-0989>.
- [10] B.P. Leitner, S. Huang, R.J. Brychta, et al., Mapping of human brown adipose tissue in lean and obese young men, *Proc. Natl. Acad. Sci. U. S. A.* 114 (32) (2017) 8649–8654, <https://doi.org/10.1073/pnas.1705287114>.
- [11] M. Saito, Y. Okamatsu-Ogura, M. Matsushita, et al., High incidence of metabolically active brown adipose tissue in healthy adult humans: effects of cold exposure and adiposity, *Diabetes* 58 (7) (2009) 1526–1531, <https://doi.org/10.2337/db09-0530>.

- [12] T. Yoneshiro, S. Aita, M. Matsushita, et al., Age-related decrease in cold-activated brown adipose tissue and accumulation of body fat in healthy humans, *Obesity*(Silver Spring) 19 (9) (2011) 1755–1760,<https://doi.org/10.1038/oby.2011.125>.
- [13] M. Soret, S.L. Bacharach, I. Buvat, Partial-volume effect in PET tumor imaging, *J.Nucl. Med.* 48 (6) (2007) 932–945,<https://doi.org/10.2967/jnumed.106.035774>.
- [14] M.C. Adams, T.G. Turkington, J.M. Wilson, et al., A systematic review of the factors affecting accuracy of SUV measurements, *AJR Am. J. Roentgenol.* 195 (2) (2010)310–320,<https://doi.org/10.2214/AJR.10.4923>.
- [15] G. Hamilton, D.L. Smith, M. Bydder, et al., MR properties of brown and white adipose tissues, *J. Magn. Reson. Imaging* 34 (2) (2011) 468–473,<https://doi.org/10.1002/jmri.22623>.
- [16] T. Romu, L. Elander, O.D. Leinhard, et al., Characterization of brown adipose tissue by water-fat separated magnetic resonance imaging, *J. Magn. Reson. Imaging* 42 (6)(2015) 1639–1645,<https://doi.org/10.1002/jmri.24931>.
- [17] Y.I. Chen, A.M. Cypess, C.A. Sass, et al., Anatomical and functional assessment of brown adipose tissue by magnetic resonance imaging, *Obesity* (Silver Spring) 20 (7)(2012) 1519–1526,<https://doi.org/10.1038/oby.2012.22>.
- [18] T.A. Bley, O. Wieben, C.J. François, et al., Fat and water magnetic resonance imaging, *J. Magn. Reson. Imaging* 31 (1) (2010) 4–18, <https://doi.org/10.1002/jmri.21895>.
- [19] J. Ren, I. Dimitrov, A.D. Sherry, et al., Composition of adipose tissue and marrow fat in humans by  $^1\text{H}$  NMR at 7 Tesla, *J. Lipid Res.* 49 (9) (2008) 2055–2062,<https://doi.org/10.1194/jlr.D800010-JLR200>.
- [20] T. Baum, C. Cordes, M. Dieckmeyer, et al., MR-based assessment of body fat distribution and characteristics, *Eur. J. Radiol.* 85 (8) (2016) 1512–1518,<https://doi.org/10.1016/j.ejrad.2016.02.013>.
- [21] K. Chechi, J. Nedergaard, D. Richard, Brown adipose tissue as an anti-obesity tissue in humans, *Obes. Rev.* 15 (2) (2014) 92–106,<https://doi.org/10.1111/obr.12116>.
- [22] A. Scotti, R.W. Tain, W. Li, et al., Mapping brown adipose tissue based on fat water fraction provided by Z-spectral imaging, *J. Magn. Reson. Imaging* 47 (6) (2018)1527–1533,<https://doi.org/10.1002/jmri.25890>.

- [23] A. McCallister, L. Zhang, A. Burant, et al., A pilot study on the correlation between fat fraction values and glucose uptake values in supraclavicular fat by simultaneous PET/MRI, *Magn. Reson. Med.* 78 (5) (2017) 1922–1932, <https://doi.org/10.1002/mrm.26589>.
- [24] M. Kunicki, E. Rudnicka, J. Skórska, et al., Insulin resistance indexes in women with premature ovarian insufficiency - a pilot study, *Ginekol. Pol.* 89 (7) (2018) 364–369, <https://doi.org/10.5603/GP.a2018.0062>.
- [25] D.A. Dumesic, A.L. Akopians, V.K. Madrigal, et al., Hyperandrogenism accompanies increased intra-abdominal fat storage in normal weight polycystic ovary syndrome women, *J. Clin. Endocrinol. Metab.* 101 (11) (2016) 4178–4188, <https://doi.org/10.1210/jc.2016-2586>.
- [26] C.F. Draper, K. Duisters, B. Weger, et al., Menstrual cycle rhythmicity: metabolic patterns in healthy women, *Sci. Rep.* 8 (1) (2018) 14568, <https://doi.org/10.1038/s41598-018-32647-0>.
- [27] J. Deng, L.M. Neff, N.C. Rubert, et al., MRI characterization of brown adipose tissue under thermal challenges in normal weight, overweight, and obese young men, *J. Magn. Reson. Imaging* 47 (4) (2018) 936–947, <https://doi.org/10.1002/jmri.25836>.
- [28] S. Cinti, Adipose organ development and remodeling, *Compr. Physiol.* 8 (4) (2018) 1357–1431, <https://doi.org/10.1002/cphy.c170042>.
- [29] S. Shorakae, E. Jona, B. de Courten, et al., Brown adipose tissue thermogenesis in polycystic ovary syndrome, *Clin. Endocrinol. (Oxf.)* (2018), <https://doi.org/10.1111/cen.13913>.
- [30] A. Benrick, B. Chanclón, P. Micallef, et al., Adiponectin protects against development of metabolic disturbances in a PCOS mouse model, *Proc. Natl. Acad. Sci. U. S.A.* 114 (34) (2017) E7187–E7196, <https://doi.org/10.1073/pnas.1708854114>.
- [31] P. Lee, M.M. Swarbrick, K.K. Ho, Brown adipose tissue in adult humans: a metabolic renaissance, *Endocr. Rev.* 34 (3) (2013) 413–438, <https://doi.org/10.1210/er.2012-1081>.
- [32] C.G. Cronin, P. Prakash, G.H. Daniels, et al., Brown fat at PET/CT: correlation with patient characteristics, *Radiology* 263 (3) (2012) 836–842, <https://doi.org/10.1148/radiol.12100683>.
- [33] M.A. Bredella, Sex differences in body composition, *Adv. Exp. Med. Biol.* 1043(2017) 9–27, [https://doi.org/10.1007/978-3-319-70178-3\\_2](https://doi.org/10.1007/978-3-319-70178-3_2).

## 5. Z-SPECTRUM IMAGING CAN DETECT ADIPOSE TISSUE ACTIVATION THROUGH CHANGES IN FWF

### 5.1 Background and introduction

In Chapter 1, we introduced brown adipose tissue and its perks, especially the metabolic benefits its activation can bring about [1,2]. Unfortunately, BAT is not abundant in obese patient and its activation would have limited impact on the overall condition, limiting its application to surgical approaches [3-4]. The good news is that more and more reports are surfacing about the possibility of converting the widespread white adipose tissue into brown-like tissue. In fact, *browning* of adipose cells have been observed in various white fat depots [5-11]. Browning of visceral fat is of particular interest to human health due to its association to high risk of metabolic disease and its resistance to conventional browning stimuli [12-14]. Recently, browning of adipose cells have been observed in subcutaneous and visceral fat of a murine model [12-13].

Detection of BAT or the browning process is conventionally performed by measuring activity in the form of glucose uptake in  $^{18}\text{F}$ FDG-PET. Standard detection by PET/CT is yet inadequate especially for longitudinal monitoring, due to radiation exposure and low spatial resolution. Moreover, glucose, the conventional source of contrast for PET, provides just 10% of the thermogenesis fuel, whereas intracellular and plasma lipid make up for the prevalent amount [6,15]. An alternative noninvasive method is the detection of increased perfusion in BAT during activation through change in  $T_2^*$ . However, the mechanism is not specific and no consistent results have been obtained from the studies that attempted this feat [16-20]. Several studies have successfully used fat water fraction as a marker of activation, under the hypothesis that thermogenesis is fueled by lipolysis, leading to reduced fat content in the cells. In this context, almost the totality of works are based on the use of chemical shift encoded techniques like Dixon MRI [21-22]. Despite being reliable and available commercially, we showed in Chapter 3 how Z-Spectrum imaging has the advantages of being artifacts free and independent on  $B_0$

field inhomogeneity [23]. Here we therefore aimed at showing the efficacy of Z-spectrum MRI in detecting adipose tissue activation by measuring changes in FWF. In order to do so, we made use of a transgenic mouse model that previously showed enhanced predisposition to fat activation, and in particular browning of visceral fat [13-14, 24]. We chronically stimulated such mouse model with CL 316,243, a drug that is known to activate thermogenesis in adipose tissue, and compared the results after two weeks to a control group.

## 5.2 Materials and methods

In order to optimize the possibility of detection of the activation process, we included in the study the transgenic mice model developed by Liew et al. [13-14, 24]. These transgenic mice were developed from a C57Bl/6 strain by ablating the transcriptional regulator TRIP-Br2, a factor associated with obesity-related inflammation. In the KO model, expression of adipose tissue activation is facilitated.

Five female mice, aged 7 weeks old, were bred and housed at regular conditions (12 hours day/night cycle, ad libitum access to normal chow diet, 24 °C housing temperature). Every day at the same time, around noon, for fifteen days, mice were treated with 1mg/Kg of the activating drug  $\beta_3$  adrenergic receptor agonist CL316,243 by an intraperitoneal injection [25]. Age matched wild types were similarly treated with saline solution.

### 5.2.1 MRI protocol

Animals underwent MRI before and 4, 10 and 15 days after the beginning of the treatment. Experiments were carried out at a preclinical 9.4T animal scanner with 10cm bore (Varian-Agilent, Santa Clara, CA, US.). Mice were anesthetized by breathing a mixture of 3% isoflurane and air, and maintained asleep for the entire duration of the experiment by breathing through a nosecone with 1.5% mix. Respiratory

patterns and rectal temperature were monitored by a MRI compatible sensor system (Model 1025, SA Instruments Inc., Stony Brook, NY, USA). Mice were placed prone and immobilized with bitebar and tape, in order to minimize respiratory motion. The visceral area of interest was identified by scout images and high resolution multislice  $T_2$ -weighted sequences were acquired for anatomical references. Fat in the  $T_2$  FSE sequence appears bright due to breaking of J-coupling and is therefore easily distinguishable from muscular tissue. The entire fat depot spanning from the top end of the kidneys to the level of intestine was imaged and region of interest were drawn on the  $T_2$ -weighted slices in order to

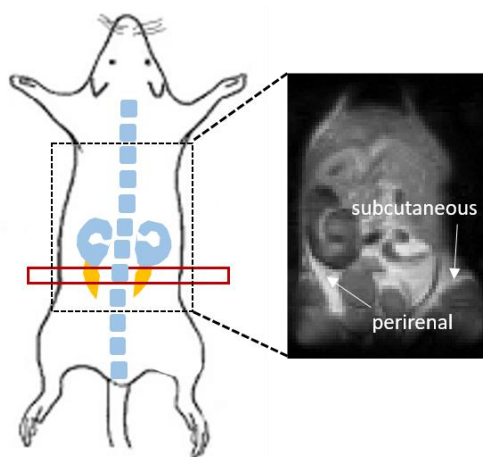


Figure 5-1 Coronal view of mouse body.

ZSI was carried out on the slice highlighted in red, including portions of the perirenal and subcutaneous fat depots.

compute the depots volume.

The subcutaneous fat sitting at the same level was imaged, but volume was not calculated, given that slightly different animal positions might result in the skin and its attached fat layers being pulled in one direction or another. Once the area of interest was identified, global and slice shimming routines were performed and a WASSR sequence [26] acquired. After a visual inspection of the WASSR data, if the  $B_0$  inhomogeneity fell within  $\pm 0.25$  ppm from the central frequency in the muscular tissue in the field of view, the field distribution was considered acceptable. Otherwise, manual shimming was repeated, or the central frequency was shifted to minimize the offset in the slice. ZSI consisted of a CEST sequence with a series of ten square saturation pulses of  $0.47 \mu\text{T}$  for 50ms each and a 1005 duty cycle, resulting in

an equivalent 500ms pulse. Frequency offsets ranged from -6 to 6 ppm at intervals of 0.1 ppm, together with  $\pm 10$ ,  $\pm 20$ ,  $\pm 100$  ppm offsets. The saturation pulse was followed by single-slice fast spin echo readout with parameters: FOV = 40 x 40 mm<sup>2</sup>, matrix size = 128 x 128, echo train length (ETL) = 16, effective TE = 4.9 ms. The delay time between repetitions was 1.5 s.

### 5.2.2 Image processing

After normalizing all data to the 100 ppm signal intensity, Z-spectral data were smoothed with a spline function over the frequency dimension, to remove gross jerk-motion artifacts. Pixelwise curves were fitted to a multi-Lorentzian model including the direct saturation of water and fat peaks and the magnetization transfer from semisolid components like macromolecules. The fat profile was described by the main 6 resonances. The least square fit curves' were fitted by determining the parameters amplitude, width and offset for each Lorentzian curve, as described before. Parameters were loosely constrained to account for variation in lipid composition. FWF was quantified from the fitted amplitudes as previously said and colormaps generated for each mouse [23].

Perirenal fat depots and subcutaneous fat regions of interest were drawn on FSE  $T_2$  images at the corresponding slice to the ZSI images. Comparison between groups at different time points were evaluated by two-tailed student's t-test. Significance level was set to 5%.

## 5.3 Results

Image quality in the visceral area was good, free from gross artifacts deriving from respiratory or peristaltic motions. Fitting performance was good everywhere, with residuals below 2%. The perirenal depots in the axial view were easily identifiable and distinguishable from surrounding organs or

muscular tissue, given the bright signal on FSE images (especially at 100 ppm offset, where direct saturation is minimal).

As a main result we found that the drug treated mice developed a lower fat-water fraction over time compared to the control group. Exemplary fat-water fraction maps derived from the pixelwise fitting are shown in Fig. 5.2. The treated mice feature a clearly reduced content of lipids compared to the wild type controls treated with saline, both in the perirenal (white arrows) and the subcutaneous (black arrows) fat depots.

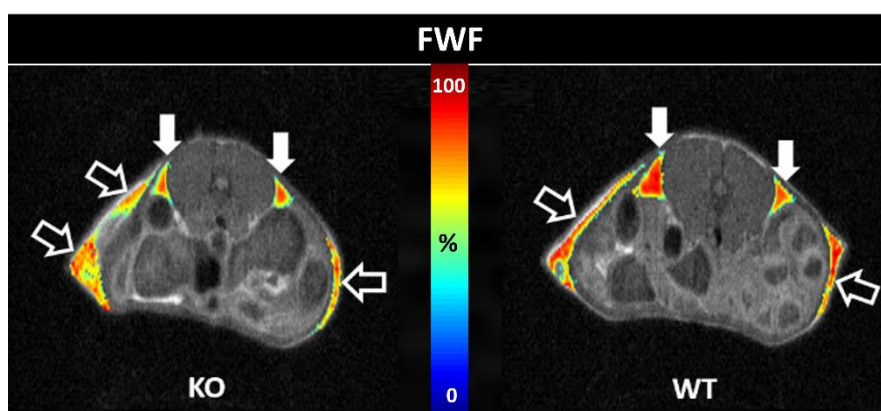


Figure 5-2 FWF colormaps.

Color-coded maps of fat-water fraction in treated transgenic (left) and wild types untreated mice (right), overlaid to anatomical T<sub>2</sub>-weighted slice of the visceral area. Data are from 10 days into the treatment.

The groupwise distribution is shown in Figure 5.3. Values are presented as mean  $\pm$  standard deviation among mice in the treated and untreated groups. The average values within the regions of interest of depots on both sides were used to compute the distribution. FWF differences between the groups in perirenal fat up to 15% were already detectable after 4 days, and increased to 20% at ten days, but decreased at 2 weeks. Subcutaneous fat showed a sustained decrease in FWF, reaching an average of 25% reduction at the end of the study, but with a higher variability within the group (12% in subcutaneous vs 6.5% in perirenal).

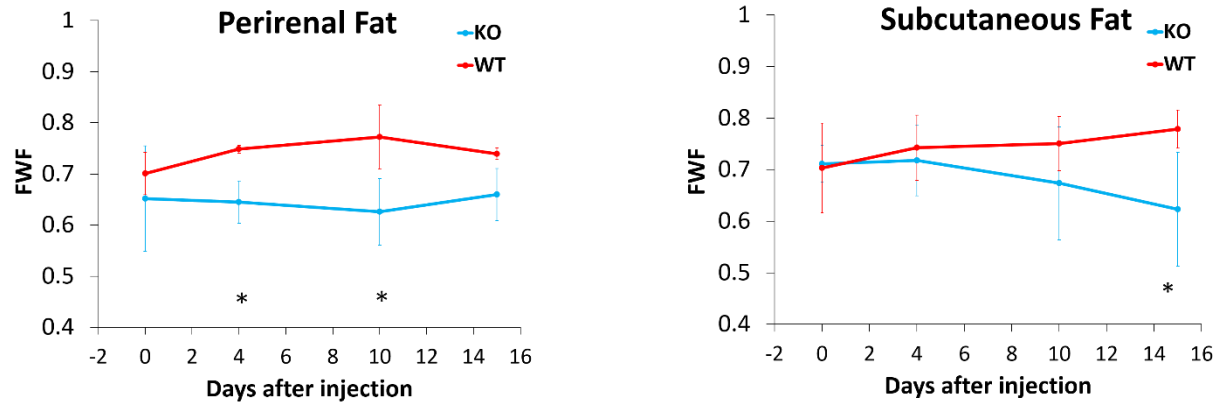


Figure 5-3 FWF trends.

Lower fat-water fraction was found in the CL316243- treated mice compared to the wild types, in both perirenal brown fat and subcutaneous white fat.

Decrease in FWF was consistent with a reduced volume: the perirenal fat depots decreased in size over time in the KO mice, with volumes shrinking from  $11.7 \pm 1.9 \text{ mm}^3$  before treatment to  $6.9 \pm 2.4 \text{ mm}^3$  after two weeks. The wild types instead had stable or slightly increased size throughout the study. Finally, also the average body weight was found lower in the mice from the treated group compared to the untreated wild types (18.9 vs 24.2 g).

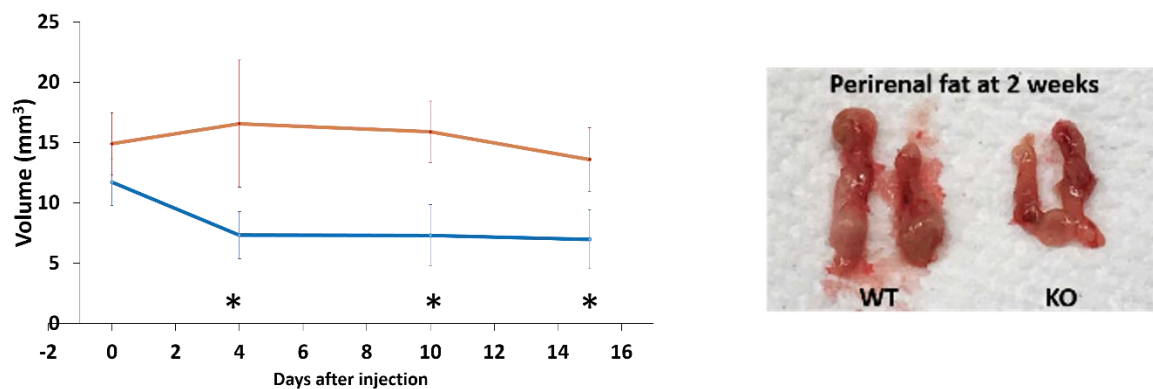


Figure 5-4 Volume trends.

Perirenal brown fat depot volume assessed by T<sub>2</sub>-weighted multislice images. Treated transgenic mice (blue line) decreased in volume compared to the wild types. On the right, perirenal depots, resected from mice after two weeks of treatment, show a clear difference in size between the groups.

## 5.4 Discussion

In this experiment, we showed how Z-spectrum MRI can successfully measure changes in FWF as a marker of brown fat activation. After the increased uptake of glucose seen on  $^{18}\text{F}$ FDG PET, measuring fat content reduction is the most widespread method to assess the thermogenic activity in the adipose organ [27-30]. Here, we aimed at following this strategy for demonstrating the validity of the proposed technique, ZSI, in accomplishing a similar task. At the same time, we wanted to exploit the potential of an animal model which features gives him a relevant position in the study of brown adipose tissue [13-14, 24].

We found significantly lower FWF and volume in the transgenic mice treated with the adrenergic drug, compared to the saline-treated wild types. In all tested mice, derived FWF maps were free from phase artifacts and a small intersubject variability was recorded.

As pointed out by many other works, the reduction in fat fraction can descend from two separate factors. Firstly, to an increased water content, attributable to an enhanced blood flow. It has in fact been demonstrated that BAT depots are much more vascularized than white depots and when activated, a potent blood flow is cast into the tissue [30-31]. It is possible that chronic activation over two weeks led to a boosted vascular system in the adipose depots.

Still, the volume ratio of even an enhanced vascularization could not justify more than 10% decrease in FWF. The second possible factor to be called into question is therefore a reduced lipid content, most likely manifesting as a breakdown of intracellular triglycerides. It has been previously observed a reduction in the size of the lipid droplets harbored within the cells of a fat depot undergoing activation, and a relative occupation of their space by the cytoplasm. The mechanism underlying our technique, Z-spectrum MRI, is based on the direct saturation of protons on the fatty acids chains. A reduction in the cellular volume of lipids available for saturation will lead to a reduced relative fat saturation and an

increase in the signal from water, translating in a net lower fat-water fraction. This mechanism is consistent with the second main finding of our study, that is, a reduced size of the entire perirenal fat depot. It is therefore reasonable to conclude that the lower fat fraction in transgenic mice was indeed due to a lower intracellular lipid content, marker of brown adipose tissue activation, induced by the drug stimulation.

It is interesting to note the different evolution of FWF in perirenal and subcutaneous fat depots. In mice, the small depots below the kidneys is considered to be formed by classical brown adipocytes, similar to the ones found in the interscapular depots [32-33]. What we see in our results is that FWF is slightly decreased over time, but what drives the main difference between the groups is the increase in FWF in the control group. The wild types mice, in fact, seem to undergo a mild fat accumulation in the depot. Considering the mice under study are young, the phenomenon can be attributed to the simple process of ageing [34-35]. Chronic BAT activation in the treated mice will cause resistance to this accumulation and maintain a low FWF in the depot over time. The data show a different story in the subcutaneous white fat, where the FWF significantly decreased over time in all treated mice, compared to the beginning of the study. It is here than a true browning process, a conversion from white to brown adipocytes, is more impactful. The timeline of FWF changes, with a quick and maintained response in brown depot, as opposed to a delayed but increasing response in the white/beige depot, is also consistent with a different susceptibility to activation previously suggested [36-38]. It is possible that extending the duration of the experiment beyond two weeks would have showed different results. In some recent studies, in fact, Liew et al. suggested a potential adaptation mechanism occurring in adipose tissue subject to thermogenic stimulation, especially in visceral fat [39]. Such mechanism consists on a remodeling of the lipid composition and might lead to resistance to activation, after an initial apparent response. In future studies, we will address this possibility and investigate the best timeline for a comprehensive study.

There are a number of confounding effects in the study of brown adipose tissue activation. The mice housing temperature (24°C) might have caused the mice to be in a state of mild activation, being not at complete thermoneutrality (30°C) [36]. The effect of the CL 316,243 drug in this case would be to stimulate the activation further, with respect to the untreated cohort. It has been proposed that a more translational approach would have been to select “humanized” conditions, that is, the conditions at which BAT in mice is more similar to BAT in humans: living at thermoneutrality, with a high fat diet, sedentary. Regardless, the differences between the cohorts still reach significant levels and we expect at humanized conditions they would have been accentuated.

The choice of performing a chronic activation in spite of an acute activation in the experiment design is given by the more consistent results found in literature and by the possibility to use isoflurane as anesthetic agent. Isoflurane and other volatile anesthetics have been suggested to significantly reduce activation in mice [40]. While different studies managed to detect activation even when using isoflurane, we resolved to avoid such possibility even for a slightly reduced activation. By administering the drug on awake mice, every day, we limit the impact that the anesthetic inhaled only during image session might have on the overall activation status.

The inclusion of the transgenic mouse model Trip2-KO, while not strictly indispensable for the assessment of ZSI efficacy, has nevertheless indicated a valid model for the study of fat activation, in particular in the visceral area. The majority of imaging BAT studies focuses on the larger interscapular depot in mice, but the perirenal depots offers the advantages of being less affected by respiratory motion and phase artifacts and more clearly isolated from subcutaneous fat. We showed how, in this mouse model, activation of perirenal BAT and subcutaneous white fat is easily achievable by a simple adrenergic drug administration. In this experiment we lacked the possibility to perform a solid pathological validation of the ZSI findings, including for example staining for the thermogenic protein UCP1. But we expect that our study would have produced similar results to what previously published

[13-14, 24]. Surely we will include a histological assessment in the next study, along with a larger sample size (~10/group) and a control group of wild types treated with CL 316,243 to investigate differences uniquely given by the transgenic model.

In conclusion, we demonstrated how the use of Z-spectrum MRI to measure FWF is feasible in an *in vivo* experiment of adipose tissue activation. We showed that in the current transgenic model, chronic treatment with CL 316,243 leads to reduced fat content and volume in perirenal brown and subcutaneous visceral white fat.

## 5.5 Summary

The purpose of this experiment was to demonstrate the efficacy of Z-spectrum MRI in detecting adipose tissue activation through changes in FWF. Detection of brown and white adipose tissue activation are of particular interest due to their benefits against obesity and metabolic disorders. Here a transgenic mouse model, TripBr2-KO, was treated with an adrenergic drug to stimulate fat activation. Mice were studied for two weeks by Z-spectrum MRI and compared to saline-treated wild types. FWF derived from ZSI was significantly reduced over time in the treated group compared to the controls, suggesting that lipid consumption, associated with adipose tissue activation, has occurred. The successful detection, confirmed by a reduction in the depot size, was found both in perirenal brown fat and in subcutaneous white fat.

## Bibliography

1. Rui L. Brown and Beige Adipose Tissues in Health and Disease. *Compr Physiol*. 2017 Sep 12;7(4):1281-1306. doi: 10.1002/cphy.c170001. PMID: 28915325; PMCID: PMC6192523.
2. Srivastava S, Veech RL. Brown and Brite: The Fat Soldiers in the Anti-obesity Fight. *Front Physiol*. 2019 Jan 30;10:38. doi: 10.3389/fphys.2019.00038. PMID: 30761017; PMCID: PMC6363669.
3. Trayhurn P. Brown Adipose Tissue-A Therapeutic Target in Obesity? *Front Physiol*. 2018;9:1672. doi: 10.3389/fphys.2018.01672. PubMed PMID: 30532712; PMCID: PMC6265308.
4. Emont MP, Kim DI, Wu J. Development, activation, and therapeutic potential of thermogenic adipocytes. *Biochim Biophys Acta Mol Cell Biol Lipids*. 2019;1864(1):13-9. doi: 10.1016/j.bbalip.2018.05.004. PubMed PMID: 29763732; PMCID: PMC6240366.
5. Ishibashi J, Seale P. Medicine. Beige can be slimming. *Science*. 2010;328(5982):1113-4. doi: 10.1126/science.1190816. PubMed PMID: 20448151; PMCID: PMC2907667.
6. Ong FJ, Ahmed BA, Oreskovich SM, Blondin DP, Haq T, Konyer NB, Noseworthy MD, Haman F, Carpentier AC, Morrison KM, Steinberg GR. Recent advances in the detection of brown adipose tissue in adult humans: a review. *Clin Sci (Lond)*. 2018;132(10):1039-54. doi: 10.1042/CS20170276. PubMed PMID: 29802209.
7. Young P, Arch JR, Ashwell M. Brown adipose tissue in the parametrial fat pad of the mouse. *FEBS Lett*. 1984;167(1):10-4. PubMed PMID: 6698197.
8. Himms-Hagen J, Melnyk A, Zingaretti MC, Ceresi E, Barbatelli G, Cinti S. Multilocular fat cells in WAT of CL-316243-treated rats derive directly from white adipocytes. *Am J Physiol Cell Physiol*. 2000;279(3):C670-81. doi: 10.1152/ajpcell.2000.279.3.C670. PubMed PMID: 10942717.
9. Xue B, Coulter A, Rim JS, Koza RA, Kozak LP. Transcriptional synergy and the regulation of Ucp1 during brown adipocyte induction in white fat depots. *Mol Cell Biol*. 2005;25(18):8311-22. doi: 10.1128/MCB.25.18.8311-8322.2005. PubMed PMID: 16135818; PMCID: PMC1234324.
10. Chen YC, Cypess AM, Chen YC, Palmer M, Kolodny G, Kahn CR, Kwong KK. Measurement of human brown adipose tissue volume and activity using anatomic MR imaging and functional MR imaging. *J Nucl Med*. 2013;54(9):1584-7. doi: 10.2967/jnumed.112.117275. PubMed PMID: 23868958; PMCID: PMC4167352.
11. Wu J, Bostrom P, Sparks LM, Ye L, Choi JH, Giang AH, Khandekar M, Virtanen KA, Nuutila P, Schaart G, Huang K, Tu H, van Marken Lichtenbelt WD, Hoeks J, Enerback S, Schrauwen P, Spiegelman BM. Beige adipocytes are a distinct type of thermogenic fat cell in mouse and human. *Cell*.

- 2012;150(2):366-76. doi: 10.1016/j.cell.2012.05.016. PubMed PMID: 22796012; PMCID: PMC3402601.
12. He P, Hou B, Li Y, Xu C, Ma P, Lam SM, Gil V, Yang X, Yang X, Zhang L, Shui G, Song J, Qiang G, Liew CW, Du G. Lipid Profiling Reveals Browning Heterogeneity of White Adipose Tissue by B3-Adrenergic Stimulation. *Biomolecules* 2019, 9, 444; doi:10.3390/biom9090444.
  13. Qiang G, Kong HW, Fang D, et al. The obesity-induced transcriptional regulator TRIP-Br2 mediates visceral fat endoplasmic reticulum stress-induced inflammation. *Nat Commun.* 2016;7:11378. Published 2016 Apr 25. doi:10.1038/ncomms11378.
  14. Qiang G, Whang Kong H, Gil V, Liew CW. Transcription regulator TRIP-Br2 mediates ER stress-induced brown adipocytes dysfunction. *Sci Rep.* 2017;7:40215. Published 2017 Jan 9. doi:10.1038/srep40215.
  15. Kaisanlahti A, Glumoff T. Browning of white fat: agents and implications for beige adipose tissue to type 2 diabetes. *J Physiol Biochem.* 2018. doi: 10.1007/s13105-018-0658-5. PubMed PMID: 30506389.
  16. Hu Q, Cao H, Zhou L, Liu J, Di W, Lv S, Ding G, Tang L. Measurement of BAT activity by targeted molecular magnetic resonance imaging. *Magn Reson Imaging.* 2020 Dec 10;77:1-6. doi: 10.1016/j.mri.2020.12.006. Epub ahead of print. PMID: 33309921.
  17. Hui SCN, Ko JKL, Zhang T, Shi L, Yeung DKW, Wang D, Chan Q, Chu WCW. Quantification of brown and white adipose tissue based on Gaussian mixture model using water-fat and T2\* MRI in adolescents. *J Magn Reson Imaging.* 2017 Sep;46(3):758-768. doi: 10.1002/jmri.25632. Epub 2017 Jan 16. PMID: 28092409.
  18. Franz D, Diefenbach MN, Treibel F, Weidlich D, Syväri J, Ruschke S, Wu M, Holzapfel C, Drabsch T, Baum T, Eggers H, Rummeny EJ, Hauner H, Karampinos DC. Differentiating supraclavicular from gluteal adipose tissue based on simultaneous PDFF and T<sub>2</sub> \* mapping using a 20-echo gradient-echo acquisition. *J Magn Reson Imaging.* 2019 Aug;50(2):424-434. doi: 10.1002/jmri.26661. Epub 2019 Jan 25. PMID: 30684282; PMCID: PMC6767392.
  19. Oreskovich SM, Ong FJ, Ahmed BA, Konyer NB, Blondin DP, Gunn E, Singh NP, Noseworthy MD, Haman F, Carpentier AC, Punthakee Z, Steinberg GR, Morrison KM. MRI Reveals Human Brown Adipose Tissue Is Rapidly Activated in Response to Cold. *J Endocr Soc.* 2019 Oct 14;3(12):2374-2384. doi: 10.1210/js.2019-00309. PMID: 31745532; PMCID: PMC6855213.
  20. van Rooijen BD, van der Lans AA, Brans B, Wildberger JE, Mottaghy FM, Schrauwen P, Backes WH, van Marken Lichtenbelt WD. Imaging cold-activated brown adipose tissue using dynamic T2\*-

weighted magnetic resonance imaging and 2-deoxy-2-[18F]fluoro-D-glucose positron emission tomography. *Invest Radiol*. 2013 Oct;48(10):708-14. doi: 10.1097/RLI.0b013e31829363b8. PMID: 23695084.

21. Stahl V, Maier F, Freitag MT, Floca RO, Berger MC, Umathum R, Diaz MB, Herzig S, Dimitrakopoulou-strauss A, Rink K, Bachert P, Ladd ME, Nagel AM. In Vivo Assessment of Cold Stimulation Effects on the Fat Fraction of Brown Adipose Tissue Using DIXON MRI. *J Magn Reson Imaging*. 2016;1-12. doi: 10.1002/jmri.25364.
22. Lundström E, Strand R, Johansson L, Bergsten P, Ahlström H. Magnetic Resonance Imaging Cooling- Reheating Protocol Indicates Decreased Fat Fraction via Lipid Consumption in Suspected Brown Adipose Tissue. *Plos One*. 2015;1-13. doi: 10.1371/journal.pone.0126705.
23. Scotti A, Tain RW, Li W, Gil V, Liew CW, Cai K. Mapping brown adipose tissue based on fat water fraction provided by Z-spectral imaging. *J Magn Reson Imaging*. 2018;47(6):1527-33. doi: 10.1002/jmri.25890. PubMed PMID: 29148120; PMCID: PMC5957768.
24. Liew CW, Boucher J, Cheong JK, Vernochet C, Koh HJ, Mallol C, Townsend K, Langin D, Kawamori D, Hu J, Tseng YH, Hellerstein MK, Farmer SR, Goodyear L, Doria A, Bluher M, Hsu SI, Kulkarni RN. Ablation of TRIP-Br2, a regulator of fat lipolysis, thermogenesis and oxidative metabolism, prevents diet-induced obesity and insulin resistance. *Nat Med*. 2013;19(2):217-26. doi: 10.1038/nm.3056. PubMed PMID: 23291629; PMCID: PMC3567215.
25. Leitner BP, Weiner LS, Desir M, Kahn PA, Selen DJ, Tsang C, Kolodny GM, Cypess AM. Kinetics of human brown adipose tissue activation and deactivation. *Int J Obes (Lond)*. 2018. doi: 10.1038/s41366-018-0104-3. PubMed PMID: 29795459; PMCID: PMC6252171.
26. Kim M, Gillen J, Landman BA, Zhou J, van Zijl PC. Water saturation shift referencing (WASSR) for chemical exchange saturation transfer (CEST) experiments. *Magn Reson Med*. 2009 Jun;61(6):1441-50. doi: 10.1002/mrm.21873. PMID: 19358232; PMCID: PMC2860191.
27. Gerngross C, Schretter J, Klingenspor M, Schwaiger M, Fromme T. Active Brown Fat During (18)F-FDG PET/CT Imaging Defines a Patient Group with Characteristic Traits and an Increased Probability of Brown Fat Redetection. *J Nucl Med*. 2017;58(7):1104-10. doi: 10.2967/jnumed.116.183988. PubMed PMID: 28104743.
28. Gifford A, Towse TF, Walker RC, Avison MJ, Welch EB, Gifford A, Tf T, Rc W, Mj A, Eb W. Characterizing active and inactive brown adipose tissue in adult humans using PET-CT and MR imaging. *Am J Physiol Endocrinol Metab*. 2016;i:95-104. doi: 10.1152/ajpendo.00482.2015.
29. Fueger BJ, Czernin J, Hildebrandt I, Tran C, Halpern BS, Stout D, Phelps ME, Weber WA. Impact of

Animal Handling on the Results of 18 F-FDG PET Studies in Mice. *The Journal of Nuclear Medicine*. 2006;999-1007.

30. Cypess AM, Haft CR, Laughlin MR, Hu HH. Brown Fat in Humans: Consensus Points and Experimental Guidelines. *Cell Metab*. 2015;20:408-15. doi: 10.1016/j.cmet.2014.07.025. Brown.
31. Leitner BP, Weiner LS, Desir M, Kahn PA, Selen DJ, Tsang C, Kolodny GM, Cypess AM. Kinetics of human brown adipose tissue activation and deactivation. *Int J Obes (Lond)*. 2018. doi: 10.1038/s41366-018-0104-3. PubMed PMID: 29795459; PMCID: PMC6252171.
32. Cao Q, Liu L, Hu Y, Jiang N, Wang Y, Chen J, Zhou Q, Guo R. Irradiation of carotid baroreceptor with low-intensity pulsed ultrasound exerts different metabolic protection in perirenal, epididymal white adipose tissue and interscapular brown adipose tissue of obese rats. *FASEB J*. 2020 Nov;34(11):15431-15447. doi: 10.1096/fj.202001550R. Epub 2020 Sep 21. PMID: 32954572.
33. Jespersen NZ, Feizi A, Andersen ES, Heywood S, Hattel HB, Dagaard S, Peijs L, Bagi P, Feldt-Rasmussen B, Schultz HS, Hansen NS, Krogh-Madsen R, Pedersen BK, Petrovic N, Nielsen S, Scheele C. Heterogeneity in the perirenal region of humans suggests presence of dormant brown adipose tissue that contains brown fat precursor cells. *Mol Metab*. 2019 Jun;24:30-43. doi: 10.1016/j.molmet.2019.03.005. Epub 2019 Mar 15. PMID: 31079959; PMCID: PMC6531810.
34. Islam MT, Henson GD, Machin DR, Bramwell RC, Donato AJ, Lesniewski LA. Aging differentially impacts vasodilation and angiogenesis in arteries from the white and brown adipose tissues. *Exp Gerontol*. 2020 Dec;142:111126. doi: 10.1016/j.exger.2020.111126. Epub 2020 Oct 25. PMID: 33203620.
35. Zhang D, He S, Wang Q, Pu S, Zhou Z, Wu Q. Impact of Aging on the Characterization of Brown and White Adipose Tissue-Derived Stem Cells in Mice. *Cells Tissues Organs*. 2020;209(1):26-36. doi: 10.1159/000507434. Epub 2020 Jun 11. PMID: 32526740.
36. Jankovic A, Golic I, Markelic M, Stancic A, Otasevic V, Buzadzic B, Korac A, Korac B. Two key temporally distinguishable molecular and cellular components of white adipose tissue browning during cold acclimation. *J Physiol*. 2015;593(15):3267-80. doi: 10.1113/JP270805. PubMed PMID: 26096127; PMCID: PMC4553052.
37. Giordano A, Smorlesi A, Frontini A, Barbatelli G, Cinti S. White, brown and pink adipocytes: The extraordinary plasticity of the adipose organ. *European Journal of Endocrinology*. 2014;170. doi: 10.1530/EJE-13-0945. PubMed PMID: 24468979.
38. Cinti S. UCP1 protein: The molecular hub of adipose organ plasticity. *Biochimie*. 2017;134:71-6.

doi: 10.1016/j.biochi.2016.09.008. PubMed PMID: 27622583.

39. Hou B, Zhao Y, He P, Xu C, Ma P, Lam SM, Li B, Gil V, Shui G, Qiang G, Liew CW, Du G. Targeted lipidomics and transcriptomics profiling reveal the heterogeneity of visceral and subcutaneous white adipose tissue. *Life Sci.* 2020 Mar 15;245:117352. doi: 10.1016/j.lfs.2020.117352. Epub 2020 Jan 29. PMID: 32006527.
40. Ohlson KB, Lindahl SG, Cannon B, Nedergaard J. Thermogenesis inhibition in brown adipocytes is a specific property of volatile anesthetics. *Anesthesiology.* 2003;98(2):437-48. PubMed PMID: 12552204.

## 6. Z-SPECTRUM IMAGING TO MEASURE TEMPERATURE

### 6.1 Introduction

The first and most distinguishing feature of brown adipose tissue is unquestionably the nonshivering thermogenesis (1). This mechanism has been historically considered a regulatory system to maintain the optimal body temperature in harsh environmental conditions, but it also has a range of metabolic consequences (2-4). The path to fully understand the mechanism of activation of thermogenesis in fat is still long and impervious and a convenient strategy for its detection hasn't been established yet. In adult humans it has been reported that BAT distribution is sparse and detection relies on *a priori* knowledge of the position of active depots (5).  $^{18}\text{F}$ FDG-PET is currently the gold standard technique (6-8), but its use in BAT imaging is burdened by technical and conceptual limits (9). It is also inadequate for the study of thermogenesis, since it has been shown that increased BAT  $^{18}\text{F}$ -FDG uptake can occur independently of thermal function (10). Alternatively, it has been proposed to exploit the characteristic increased perfusion to image thermogenic fat (11). However, the thermogenic process is uncoupled from the perfusion increase, as it has been recently reported (12), suggesting a simultaneous occurrence but not a causal relationship. In conclusion, a direct detection of the thermogenesis is a preferable route.

Among the noninvasive methods, Magnetic Resonance has become the methodology of choice for thermometry measurement and is currently used to monitor clinical thermal therapies efficacy (13). Many MR properties are affected by temperature changes: relaxation times  $T_1$  and  $T_2$ , magnetization transfer ratio and proton resonance frequency shift. Water PRFS-based temperature measurements are widely used because of the relatively high sensitivity ( $-0.01$  ppm/ $^{\circ}\text{C}$ ) and because of their versatility in different tissues (13-14). PRF shifts can be measured directly by  $^1\text{H}$ -MR Spectroscopy in the localized voxels of interest relying on non-shifting protons like methyl and methylene protons as reference (15-16). However, being a spectroscopic method, this technique suffers from low spatial resolution or

impractically long acquisition times. In alternative, the temperature change can be derived from the phase difference between gradient echo images acquired at different temperatures (17-18).

Unfortunately, when the measurement has to be performed in fatty tissues, the signal might be corrupted by the fat protons resonating close to water (-3.5 ppm distant) but generally stable from shifts in the frequency domain. The cohabitation of protons from the two species in the same voxel translates to an ambiguity in the signal phase, which can produce artifacts or uncertainties (19-21). This problem is present in any mixed tissue, and crucially relevant in thermogenic brown adipose tissue.

As discussed in the previous chapters, Z-Spectrum imaging has been used to measure the fat-water fraction in BAT by the simultaneous measurement of fat and water resonances. Interestingly, the spectrally selective nature of the technique has in theory the potential to provide also information about frequency shifts and therefore temperature (22-23), while at the same time being independent from phase artifacts encountered in mixed tissues (23). Here we aim to prove this concept by designing a modification of the Z-spectrum imaging sequence that allows a high sensitivity thermal measurement in aqueous and fatty tissues.

## 6.2 Materials and methods

### 6.2.1 Z-spectrum for temperature

As described in Chapter 2, the PRFS effect allows to derive the information on local temperature from the Larmor frequency in the voxel. Therefore, any sequence that can selectively tag the water resonance and monitor its traveling in the frequency domain is theoretically amenable to temperature measurement. Z-spectrum imaging, as presented here, fits the description: the water offset is identified by the position of the center of the Lorentzian curve representing the direct saturation of the bulk water

protons. When temperature changes, we can observe the curve shifting (Fig. 6.1) and is thus possible to measure the thermal differential after fitting the curve at two time points, as presented in (23-24).

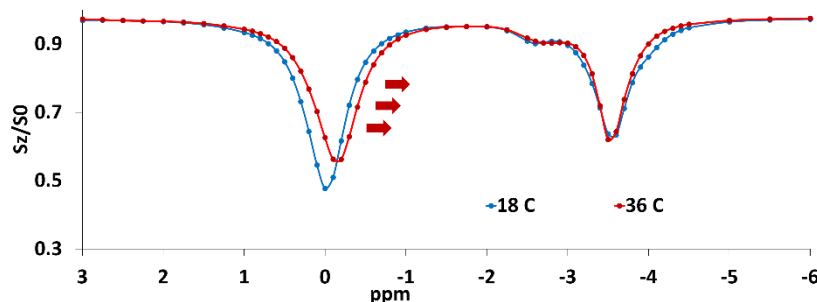


Figure 6-1 Z-spectra from brown adipose tissue at different temperatures. When the tissue is heated, the water dip (around 0 ppm) shifts toward lower frequencies (red curve). The methylene dip (around -3.5ppm) is instead fairly stable and no shift is observed.

Now, the accuracy of the thermal measurement depends on the precision of the water resonance offset assessment. Sources of indetermination in the fitting of the Lorentzian curve can be low SNR or inadequate model. In our case, approaches to change the SNR (lower matrix, spectral width or ETL) led to negligible improvement of the already high performances (<2% residuals) or were limited by the presence of fat protons. Refinements of the model, by adding fat peaks to the spectral profile, carried more fitting parameters and inconsistency with previous results. Another, more resilient source of indetermination is the wide linewidth in the direct saturation curve. This can be minimized by improving the local shim or by reducing the intensity of the saturation, which has to be traded for enough signal over the background noise. But even after optimizing these factors, the linewidth is inherently limited by the  $T_2$  of the bulk water pool; our experimental routine couldn't accurately detect resonance shifts below 0.04 ppm, which translates to 4°C in aqueous tissues and is therefore not adequate for detecting the thermogenesis effect, reportedly within 3-5°C.

Hence we see how Z-spectrum imaging, due to its spectrally selective form, is a natural platform for the measurement of proton resonance frequency shifts, but lacks the accuracy to provide fine

quantifications. A potential remedy can rest on the modification of the sequence by changing the preparation pulse.

### 6.2.2 Binomial preparation pulse

It is known that under some conditions, the excitation profile in the frequency domain can be predicted by the Fourier transform of the RF perturbation in the time domain (25). The magnetization at the frequency offset  $\Delta\omega$  can be expressed as

$$M(\Delta\omega) = i\gamma M_0(\Delta\omega) FT^{-1}[H_1(t - t_0)] \quad (20)$$

where the function  $H_1(t)$  is the perturbation profile of the RF irradiation and it is assumed to be much shorter than the relaxation time  $T_2$ . The pulse sequence scheme that produces a frequency profile proportional to  $M(\Delta\omega)$  can be thus simply inferred by inverting equation 20. In our case, we want to obtain an excitation profile that allows a high spectral resolvability, so to be able to measure fine frequency shifts. A simple sinusoidal pattern would allow this. Remembering that a cosine function is the Fourier transform of two delta functions, we can design a preparatory module made of two short pulses separated by a delay. If we consider two *sinc* pulses  $t_s$  long, separated by a lag time  $\tau$ , so that  $t_s \ll \tau$ , we have:

$$H_1(t) = \text{sinc}(t) \cdot \frac{1}{2}[\delta(t - \tau) + \delta(t + \tau)] \quad (21)$$

The Fourier transform of this function, for the convolution theorem, corresponds to the convolution of the Fourier transforms of the individual functions:

$$M(f) = \frac{\pi}{2} \text{rect}(\Delta f) * \cos(2\pi \tau \Delta f) \quad (22)$$

which represents a sinusoidal pattern oscillating within a window related to the pulse's parameters. The periodicity of the function is dependent on the delay between the pulses. It is therefore possible to modulate the periodicity, and thus the spectral resolvability, by choosing a long enough delay  $\tau$ .

This can perhaps be better pictured in the classical description of the magnetization vector. Let's consider the binomial pulse module just described, also known as the Jump and Return sequence (26-29), with hard pulses along the y-axis and opposite polarity (this is necessary for a balanced result, as we'll explained shortly. Besides the excitation profile resulting in a sine rather than a cosine, the concept is the same as for pulses with same polarity). The equilibrium magnetization along the z-axis is flipped by the first pulse, allowed to evolve during the delay  $\tau$ , and then flipped back to the yz-plane by the second pulse irradiated along -y. On-resonance protons do not evolve in the rotating frame and their magnetization will be fully flipped back onto the z-axis. Off-resonance spins instead will dephase during  $\tau$  according to their chemical shift and will have less magnetization available at the end of the module, when the readout part starts. In proximity of the central frequency, the net excitation profile will resemble a sinusoidal function of the chemical shift  $\Delta\omega$ , with null/maxima values determined by the delay-resonance product  $\Delta\omega \cdot \tau$ .

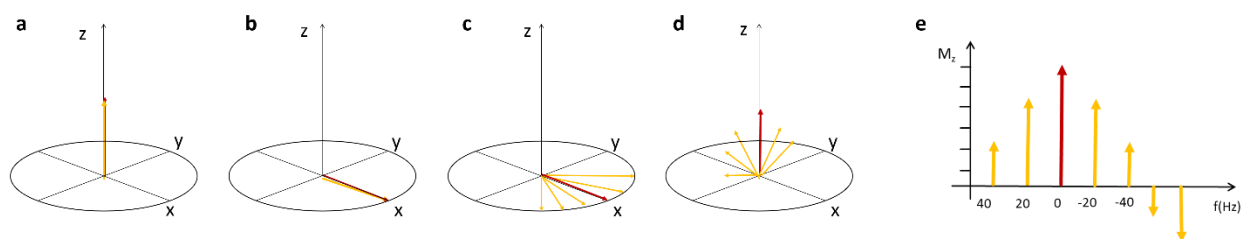


Figure 6-2 Scheme of the magnetization vector traveling during the binomial pulse.

a) At equilibrium, all spins are aligned along z. b) After the first pulse along y-axis, the spins are tilted along the x-axis. c) After the delay  $\tau$ , the off-resonance spins fan out, depending on the frequency difference with respect to the central on-resonance frequency, which is stable. d) The second pulse along -y, tilts back the spins on the yz plane. The more the magnetization is off-resonance, the more has fan out and produces less signal. e) The final pattern near the resonance is a sine function of chemical shift.

When temperature changes, the water resonance  $\omega_0 = \Delta\omega - \omega$  shifts and with it the curve. By fitting the curve with a sine function of  $(\Delta\omega \cdot \tau)$ , it is possible to keep track of the shift and therefore of the temperature changes.

### 6.2.3 In vitro experiments

As a proof of principle, experiments were first carried out on a phantom containing phosphate buffer sodium solution at a 9.4 T preclinical animal scanner. Temperature in the phantom was increased from 16 to 31 °C by regulating the warm air flow into the scanner bore. An MRI- compatible physiological monitoring system with the sensor tip inserted in the phantom monitored the thermal changes in real time. A scheme of the binomial-ZSI sequence is shown in Figure 6.3.

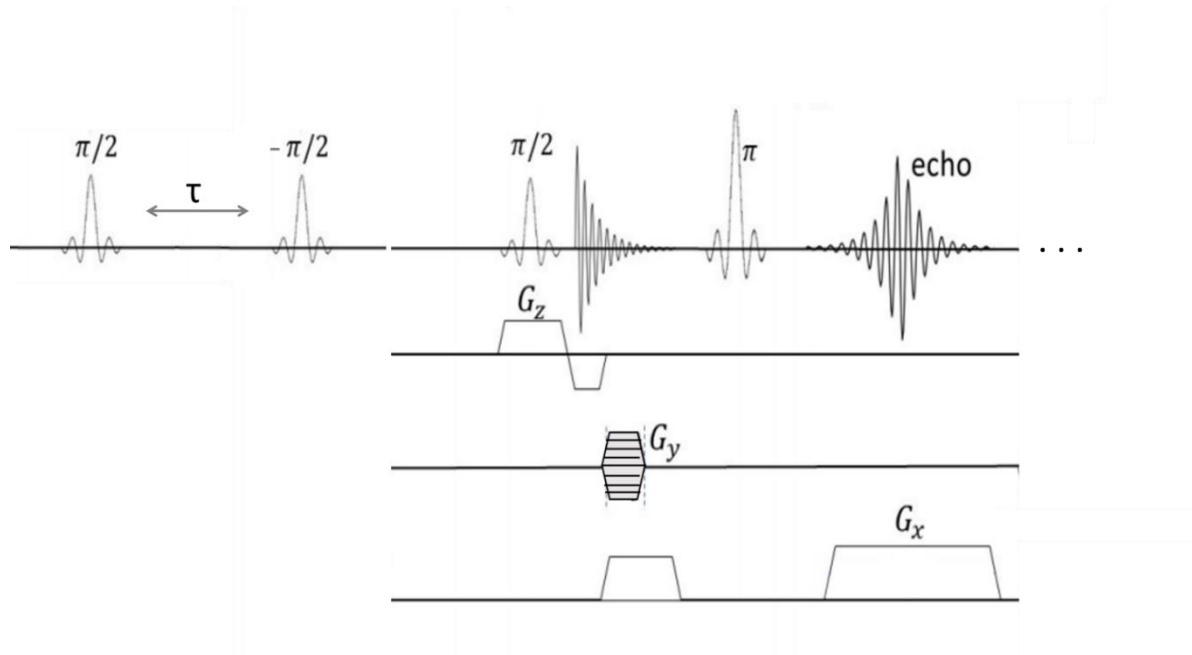


Figure 6-3 Scheme of the binomial-ZSI sequence.

The preparation module, on the left, consists of two frequency-selective pulses opposed in phase and separated by a delay much longer than their pulse width. Immediately following the preparation, a FSE readout is carried out. The scheme is repeated while tuning the preparation at all frequency offsets to sample the Z-spectrum.

The sequence consisted on a preparatory module of two 90° *sinc* pulses 0.3ms long with opposite phase (along  $y$  and  $-y$  axes), separated by a 3ms long delay. Following the preparation, applied at different frequency offsets, a FSE readout with 2 segments and a 32x32 matrix collected the signal. The sequence was repeated to monitor the temperature going up and down as controlled by the air flow.

Interleaved to the binomial-ZSI sequences, also conventional gradient echo sequences (min TE=0.85ms, 15 echoes) were acquired, and temperature variation derived from the phase differences (30-32).

After the proof of concept in the aqueous phantom, the protocol was then tested on a phantom containing heavy whipped cream (commercial, fat content ~25%) undergoing temperature variation, with the intent of showing the efficacy of the method in mixed composition tissues.

#### 6.2.4 Image processing

Data from each repetition were pooled together and fitted to a function of the chemical shift:

$$S(f) = a|1 - \sin(2\pi \tau (f - f_0))| \quad (23)$$

where  $a$  is a scaling factor constant over all repetitions, the frequencies are expressed in *Hertz* and the delay in seconds. The absolute value is considered because the fit is performed on the magnitude images. The only variable changing over time is the water resonance frequency  $f_0$ . It's possible to derive the temperature changes as:

$$\Delta T = \frac{\Delta f_0}{\alpha} \quad (24)$$

Where  $f$  is the saturation offset frequency,  $\Delta f_0$  is the shift of the water resonance at a given time point, and  $\alpha = -0.01$  °C/ppm (31).

For the study in fatty tissue, the fitting model was the sum of two sine functions (for fat and water protons) with a starting relative phase difference of  $f_0 - f_F = -3.5ppm \cdot 400 MHz/ppm$

$$S(f) = | a [1 - \sin(2\pi \tau (f - f_0))] + b [1 - \sin(2\pi \tau (f - f_F))] | \quad (25)$$

In this case, the system reduced to two variables constant over time  $a, b$  and two time-varying frequencies for water and fat pools respectively  $f_0, f_F$ .

## 6.3 Results

### 6.3.1 Excitation profile

The excitation profile in aqueous solution is described by the convolution of a sine and a square function, as predicted in equation 22. The signal over a wide range of offsets is shown in Figure 6.4. The curve rolls over as an effect of considering the magnitude signal, and the imperfect square envelope is due to the approximation of the condition  $t_s \ll \tau$ .

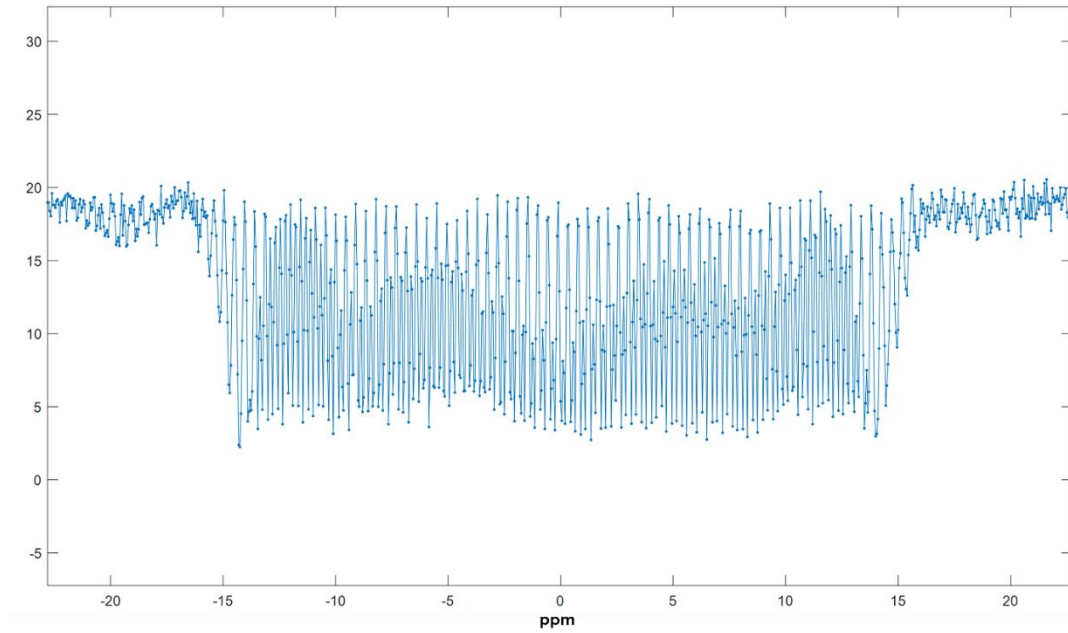


Figure 6-4 Excitation profile of binomial ZSI.

The signal oscillates as a function of the chemical shift and the delay between the pulses, within a square window determined by the pulse parameters.

In the square window, the signal oscillates with a frequency given by the product  $2\pi \cdot \Delta f \cdot \tau$  and is null at any  $f=n/2\tau$  offsets from the central frequency (or half of it, due to magnitude rollover). As a comparison, a preparation module with *square* pulses instead of *sinc*, produces a *sinc* envelope:

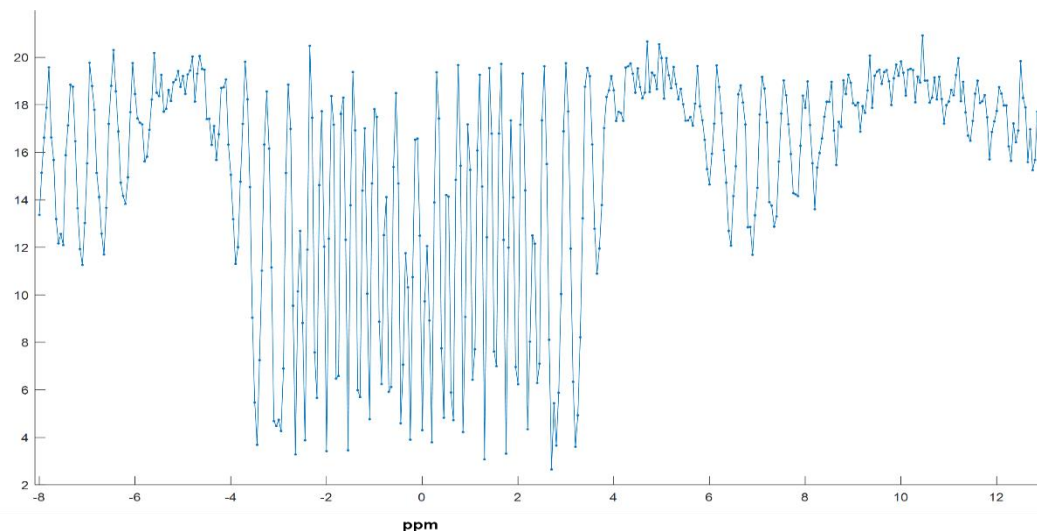


Figure 6-5 Excitation profile of binomial ZSI with square pulses.

Signal as a function of the chemical shift when the excitation module is made of a pair of square pulses separated by a delay.

### 6.3.2 Phantoms at varying temperature

When temperature changed inside the phantom, the curve clearly shifted toward lower frequencies according to the PRFS effect:

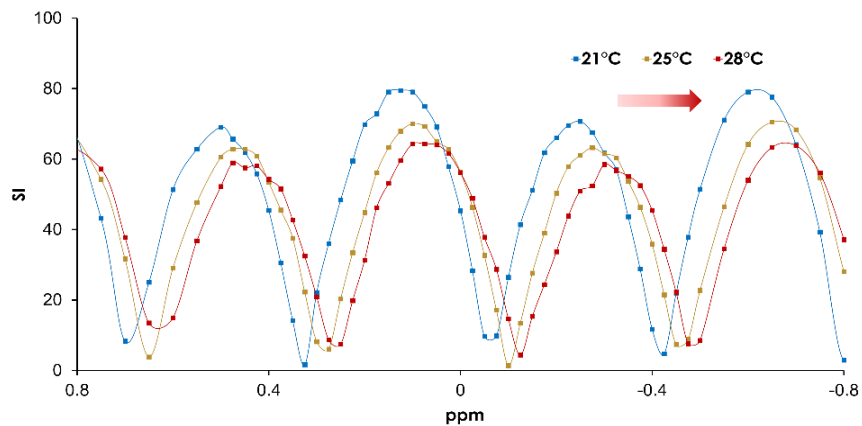


Figure 6-6 Signal modulation over frequency offsets at different temperatures.

The proton resonance frequency shift observed through the binomial-ZSI in PBS phantom heated by flowing hot air.

The curve fitting in every pixel returned colormaps of temperature change, computed with respect to the initial time point. The temperature assessment was homogeneous across the field of view and independent of  $B_0$  inhomogeneity.

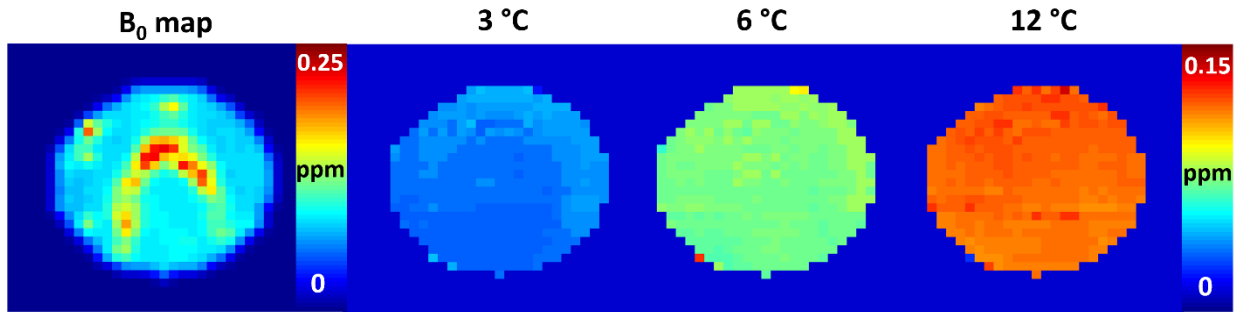


Figure 6-7 Temperature change in PBS phantom as measured by binomial-ZSI. The distribution of temperature across the imaged slice is very homogeneous, even when  $B_0$  variation are present.

The protocol, finally tested in the whipped cream phantom, also delivered an accurate measurement of temperature change over time.

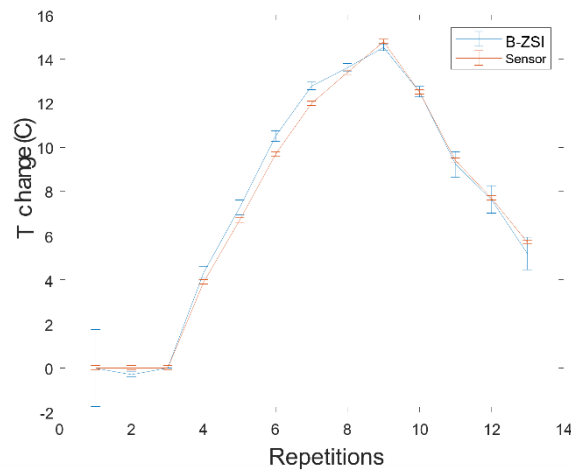


Figure 6-8 Temperature changes in whipped cream. The measurement by the binomial ZSI (blue) followed the ground truth measurement by the thermal electrode directly inserted in the phantom (red).

In fact, the thermal variation obtained from the frequency shift correlated with the ground truth measurement from the sensor, with a coefficient  $R^2 > 0.99$ , contrary to the results from the GRE phase differences, which produced as expected variable results when fat and water protons were not in-phase.

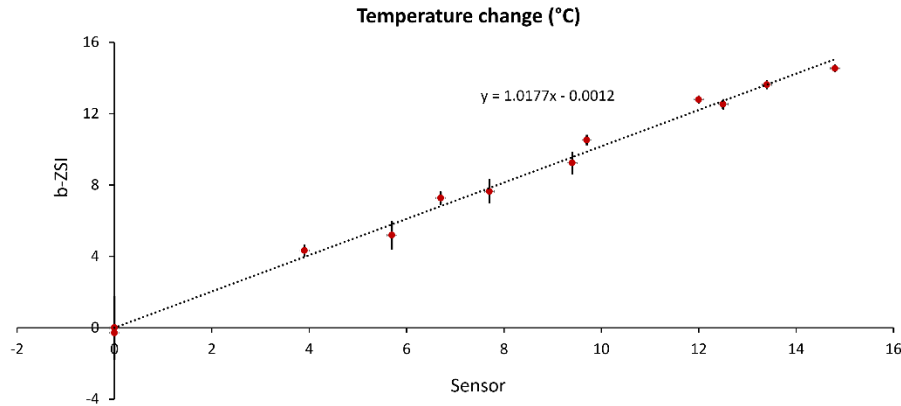


Figure 6-9 Correlation between ZSI and GRE results. The measurement of temperature changes performed by binomial-ZSI and the ground truth sensor placed inside the phantom correlated linearly with  $R^2 > 0.99$

## 6.4 Discussion

In this chapter is presented the successful design and implementation of a temperature-sensitive modification of the Z-spectrum imaging technique. After demonstrating the proof of concept in a watery solution, the protocol was applied on a whipped cream phantom exposed to heating air. Whipped cream filled in the role of a generic tissue with homogeneously mixed composition. While it might not reflect the distribution of lipid droplets in an animal cell, still the co-presence of fat and water components within the voxel constitute a valid model for the technique demonstration. Here, we were able to measure temperature change in fatty tissues through the proton resonance frequency shift (13-15).

Two great advantages derive from this technique. First, it is magnitude based, no phase component is necessary and therefore it does not suffer from the phase ambiguity that originates in fatty tissues when other techniques are used (19-21). In our test, in fact, the GRE multiecho sequence returned variable results depending on the TE adopted. For the same TE at which the echo is formed in the GRE, we assume a defined combination of water and fat protons contributing to the signal. But when the chemical shift decreases, the two species travel a series of intermediate conditions between in-phase and out-of-phase states, therefore introducing a variable weighting to the fat component into the final signal. Severe  $B_0$  inhomogeneities can also influence the determination of temperature. While reconstruction algorithms can more or less effectively address the problem, we here propose a straightforward and easily implementable approach that is inherently insensitive to phase or field issues.

A second advantage relies in the ability to control the thermal sensitivity of the technique. The key is the parameter  $\tau$ : by choosing larger delays, the periodicity of the sine function representing the signal over the frequency offsets will decrease (27). With a narrower curve, and enough signal over the noise, it will be possible to measure smaller shifts, which means, finer temperature changes. In the present work, we reached a thermal sensitivity below 1°C. We expect the same can be adopted *in vivo*.

The pulse structure 1-1 that we used in this work, also known as the Jump and Return (26), is the simplest version of binomial pulse. Many other more sophisticated combinations have been developed and can be used for the same purpose. The choice in the current work was driven by the higher signal and stable phase across the spectrum with respect to other pulses in the binomial series (27-29).

The binomial-ZSI measurement is generally dependent on the fat water fraction, as the collected signal include the resonance of both species. We don't expect in this experiment a significant change in FWF because the variation of temperature was small. The amplitude parameter  $a$  in equation 25 can include FWF weighting, but is also dependent on the tissue  $T_1$ . It will be a priority in future experiment to

combine the information from FWF and temperature, especially aimed at a comprehensive assessment of brown and browning adipose tissue.

## 6.5 Summary

Here we proposed a new sequence based on a ZSI platform, where the preparatory RF saturation pulse is substituted by a binomial pulse, the Jump-Return. The effect of the paired hard pulses is to refocus the saturated magnetization as a function of chemical shift. The resulting signal oscillates as a sine function of the offset. When the temperature changes, the PRFS assures a shift of the entire curve. The technique has been tested in PBS and fatty solution exposed to hot air flow. Being independent on phase artifacts and capable of fine thermal sensitivity, the technique may be suitable for the study of adipose tissue activation.

## Bibliography

1. Herrero, L., Fatty acid metabolism and the basis of brown adipose tissue function. *ADIPOCYTE*, 2016. **5**: p. 98-118.
2. Kiefer, F.W., The significance of beige and brown fat in humans. *Endocrine Connections*, 2017. **6**: p. R70-R79.
3. Stanford, K.I., et al., Brown adipose tissue regulates glucose homeostasis and insulin sensitivity. *J Clin Invest*, 2013. **123**: p. 215-223.
4. Liu, X., et al., Brown adipose tissue transplantation improves whole-body energy metabolism. *Cell Research*, 2013. **23**: p. 851-854.
5. Cypess, A.M., et al., Brown Fat in Humans: Consensus Points and Experimental Guidelines. *Cell Metab*, 2015. **20**: p. 408-415.
6. Borga, M., et al., Brown Adipose Tissue in Humans : Detection and Functional Analysis Using PET ( Positron Emission Tomography ), MRI ( Magnetic Resonance Imaging ), and DECT ( Dual Energy Computed Tomography ), in *Methods in Enzymology*. 2014. p. 141-159.
7. Gifford, A., et al., Characterizing active and inactive brown adipose tissue in adult humans using PET-CT and MR imaging. *Am J Physiol Endocrinol Metab*, 2016. **i**: p. 95-104.
8. Chen, K.Y., et al., Brown Adipose Reporting Criteria in Imaging Studies (BARCIST 1.0): Recommendations for Standardized FDG-PET/CT Experiments in Humans. *Cell Metabolism*, 2016. **24**: p. 210-222.
9. Yu, X.X., et al., Cold elicits the simultaneous induction of fatty acid synthesis and beta-oxidation in murine brown adipose tissue: prediction from differential gene expression and confirmation in vivo. *The FASEB journal : official publication of the Federation of American Societies for Experimental Biology*, 2002. **16**: p. 155-168.
10. Hamilton, G., et al., MR properties of brown and white adipose tissues. *J Magn Reson Imaging*, 2011. **34**(2): p. 468-73
11. Rooijen, B.D.V., et al., Imaging Cold-Activated Brown Adipose Tissue Using Dynamic T2\*-Weighted Magnetic Resonance Imaging and 2-Deoxy-2-[18F]fluoro-D-glucose Positron Emission Tomography. *Invest Radiol*, 2013. **48**: p. 708-714.
12. Abreu-vieira, G., et al., Adrenergically stimulated blood flow in brown adipose tissue is not dependent on thermogenesis. *Am J Physiol Endocrinol Metab*, 2015: p. 822-829.

13. Winter, L., et al., Magnetic resonance thermometry: Methodology, pitfalls and practical solutions. *International Journal of Hyperthermia*, 2016. **32**: p. 63-75.
14. Rieke, V. and K.B. Pauly, MR Thermometry. *JMRI*, 2013. **27**: p. 376-390.
15. Cady, E.B., et al., The estimation of local brain temperature by in vivo <sup>1</sup>H magnetic resonance spectroscopy. *Magnetic resonance in medicine : official journal of the Society of Magnetic Resonance in Medicine / Society of Magnetic Resonance in Medicine*, 1995. **33**: p. 862-867.
16. Zhu, M., Z. Sun, and C.K. Ng, Image-guided thermal ablation with MR-based thermometry. *Quantitative Imaging in Medicine and Surgery*, 2017. **7**: p. 356-368.
17. Ishihara, Y., et al., A precise and fast temperature mapping using water proton chemical shift. *Magnetic resonance in medicine : official journal of the Society of Magnetic Resonance in Medicine / Society of Magnetic Resonance in Medicine*, 1995. **34**: p. 814-823.
18. Lüdemann, L., et al., Non-invasive magnetic resonance thermography during regional hyperthermia. *International journal of hyperthermia : the official journal of European Society for Hyperthermic Oncology, North American Hyperthermia Group*, 2010. **26**: p. 273-282.
19. Poorter, J.D., Noninvasive MRI Thermometry with the Proton Resonance Frequency Method: Study of Susceptibility Effects. *MRM*, 1995. **34**: p. 359-367.
20. Yuan, J., et al., Fast fat-suppressed reduced field-of-view temperature mapping using 2D RF excitation pulses. *JMR*, 2011. **210**: p. 115-38-43.
21. Soher, B.J., et al., Noninvasive Temperature Mapping With MRI Using Chemical Shift Water-Fat Separation. *MRM*, 2011. **63**: p. 1238-1246.
22. Liu, G., et al., Non-invasive temperature mapping using temperature- responsive water saturation shift referencing (T-WASSR) MRI. *NMR Biomed*, 2015. **27**: p. 320-331.
23. Scotti, A., et al., Mapping brown adipose tissue based on fat water fraction provided by Z-spectral imaging. *J Magn Reson Imaging*, 2018. **47**(6): p. 1527-1533.
24. Scotti A, Li L, Damen F, Li W, Gil V, Zhu W, Liew CW, and Cai K. Thermal measurement in fatty tissues with Z-Spectrum Imaging. *Proc. Intl. Soc. Mag. Reson. Med.* 27 (2019); 4022.
25. Morris GA and Freeman R. Selective Excitation in Fourier Transform Nuclear Magnetic Resonance. *Journ Magn Res*, 29,433-462 (1978).
26. Plateau P, Gueron M. Exchangeable proton NMR without baseline distortion, using new strong pulse sequences. *J Am Chem Soc* 1982; 104: 7310-7311.

27. Hore PJ. Solvent suppression in Fourier transform nuclear magnetic resonance. *J Magn Reson* 1983; 55: 283– 300.
28. Harms SE, Flamig DP, Hesley KL, Evans WP 3rd, Cheek JH, Peters GN, Knox SM, Savino DA, Netto GJ, Wells RB, et al. Fat-suppressed three-dimensional MR imaging of the breast. *Radiographics*. 1993 Mar;13(2):247-67. doi: 10.1148/radiographics.13.2.8460218.
29. Thomasson D, Purdy D, Finn JP. Phase-modulated binomial RF pulses for fast spectrally-selective musculoskeletal imaging. *Magn Reson Med*. 1996 Apr;35(4):563-8. doi: 10.1002/mrm.1910350416.
30. Dickinson RJ, Hall AS, Hind AJ, Young IR. Measurement of changes in tissue temperature using MR imaging. *Journal of Computer Assisted Tomography* 1986;10:468–472.
31. Rieke V, Pauly KB. MR Thermometry. *JMRI* 2008 Feb;27(2):376-90. doi: 10.1002/jmri.21265.
32. Odéen H, Parker D. Magnetic Resonance Thermometry and Its Biological Applications - Physical Principles and Practical Considerations. *Prog Nucl Magn Reson Spectrosc*. 2019 Feb;110:34-61. doi: 10.1016/j.pnmrs.2019.01.003. Epub 2019 Jan 31.

## 7. Z-SPECTRUM MEASUREMENT OF TEMPERATURE IN VIVO

### 7.1 Introduction

Detecting thermogenesis directly is arguably the best approach to assess the function of brown and browning adipose tissue. The availability of a reliable method to measure thermogenesis is however one of the biggest limiting factor for the advancement of the field (1-2). Without it, it is harder to understand the macroscopic thermogenic mechanism, in terms of temporal and spatial distribution of activation. More importantly, without measuring thermogenesis, it is hard to develop pharmaceutical or environmental therapies to induce white fat browning and monitor the efficacy of activation-based treatments in obesity and metabolic diseases (1, 3-4).

Temperature in biological tissue can be studied through several diverse mechanisms. Indirect calorimetry is used to estimate the metabolic strain of a task, based on oxygen consumption or carbon dioxide production rate (5). Infrared thermography exploits the long-infrared range to detect the heat emitted through the body surface (6-7). But these and other popular methods are either unspecific, non-local or cannot reach penetration depths meaningful for the study of internal organs and tissues. In this respect, MRI is surely competitive and can offer large coverage, high spatial resolution and good contrast. As we presented in Chapter 2, several MR-based methods can perform temperature measurement, each one with different sensitivity and dependent on different conditions (8-10). Z-spectrum imaging is one of such methods and it has been shown in the previous chapter how the technique can in practice be adapted for thermometry.

The aim in this chapter is to show that binomial-ZSI technique can reliably be applied *in vivo* and provide thermometry data comparable to conventional methods.

In order to test the hypothesis, healthy young mice were studied under a thermal challenge. Ideally, the best validation should be carried out in brown adipose tissue, for example within the interscapular depot in rodents, right where the thermogenesis process occurs. But it has been reported that thermogenesis

might be hindered or reduced under the use of volatile anesthetics like isoflurane (11-12). In the current study, alternative anesthetics like pentobarbital were not available and therefore we were constrained to the use of isoflurane and its possible side effects. In order to avoid unpredictable thermic behavior, the experiment was then carried out in other tissues, namely the inguinal area, where large homogeneous portions of muscular and fat tissues are present. We here demonstrated that binomial-ZSI can be performed as a valid temperature measurement *in vivo*.

## 7.2 Materials and methods

The experiment included three 7 weeks old healthy male C57BL/6 mice. All studies were performed according to protocols approved by the Institutional Animal Care and Use Committee.

Before starting the MRI study, mice were observed with a thermal infrared camera (HT-04D Thermal Imager 160x120, Xintai Instrument Co., Dongguan City, GD, China) to monitor the physiological decay in body temperature induced by anesthesia. Emissivity was set to 0.95 and the camera was kept at 15 cm from the mouse body. Anesthesia was induced by 3.5% isoflurane and air mix, and maintained during imaging at 1–1.5% in 100 % O<sub>2</sub> by means of a nose cone with spontaneous respiration throughout the experiment. Mice were allowed to sleep prone on a holder in fixed position, without blanket or ventilation, and their surface temperature was registered by the thermal camera every few minutes for two hours. After experiment was completed, a different mouse was anesthetized for the MRI session. During the MR study, temperature ranging from 27°C to 36 °C in ascending and descending order were set by regulating the air flow into the scanner bore. Five minutes of delay were introduced before acquiring each image set, in order to allow some temperature stabilization. An MRI- compatible physiological monitoring system (Model 1025, SA Instruments Inc., Stony Brook, NY, USA) recorded the respiratory pattern and the body temperature through a rectal probe sensor registering the thermal

changes in real time. The imaging field of view was selected as the inguinal area due to its close proximity to the sensor probe. The imaging plane was placed just above the position of the sensor tip, in order to avoid susceptibility artifacts. MRI was carried out at an Agilent Varian 9.4T preclinical scanner with a 39 mm proton volume coil. First and second order shimming was performed to minimize  $B_0$  field inhomogeneity. WASSR sequences at the beginning and the end of the experiment were carried out to assess the entity of the inhomogeneity and eventually correct it by manually adjusting the central frequency.  $T_2$ -weighted images were obtained for anatomical reference. As in the *in vitro* experiments, the binomial-ZSI was carried out by a CEST sequence with a preparatory module consisting of two opposite phase sinc-shaped  $\pi/2$  pulses 0.5 ms long, separated by a 5 ms delay. The readout involved a fast spin echo sequence with 4 segments over a rectangular matrix 128x64 and a square 20 mm<sup>2</sup> FOV, producing square pixels sized 0.64x0.64 mm and 1 mm thickness. The preparation was repeated over 41 offsets around the water resonance, from -200 Hz to 200 Hz. The protocol was repeated without interruption throughout the duration of the thermal challenge. Interleaved to the binomial-ZSI, conventional GRE sequences with 20 echoes, a minimum  $TE$  of 1.47 ms and  $\Delta TE=1.55$  ms were acquired as references, and the phase difference between consecutive repetitions was used to compute temperature change in every pixel. In the binomial-ZSI, temperature was derived from the proton resonance frequency shift measured as a variable parameter in the curve fitting as described in the previous Chapter. To study the variation in fatty tissue, where it is expected that gradient echo sequences will suffer from phase artifacts, a series of  $T_1$  mapping sequences was acquired interleaved to ZSI in another experiment. Eleven inversion times ranging from 100 ms to 7 s were used in an inversion recovery-type sequences, for a duration of 5 minutes and a reduced matrix: 64x32. Since the coefficient  $m_1$  from equation 5 was not known in the case of mouse tissue at 9.4T, only relative  $T_1$  variations, proportional to true temperature variations, were considered. Finally, correlation between the imaging techniques were carried out with linear regressions and Pearson's coefficient was evaluated.

### 7.3 Results

Shortly after mice were anesthetized with isoflurane, their body temperature started to decrease. The decrease continued steadily for 2 hours, approaching the room temperature, until measurement stopped, going from 29°C to 24°C surface temperature.

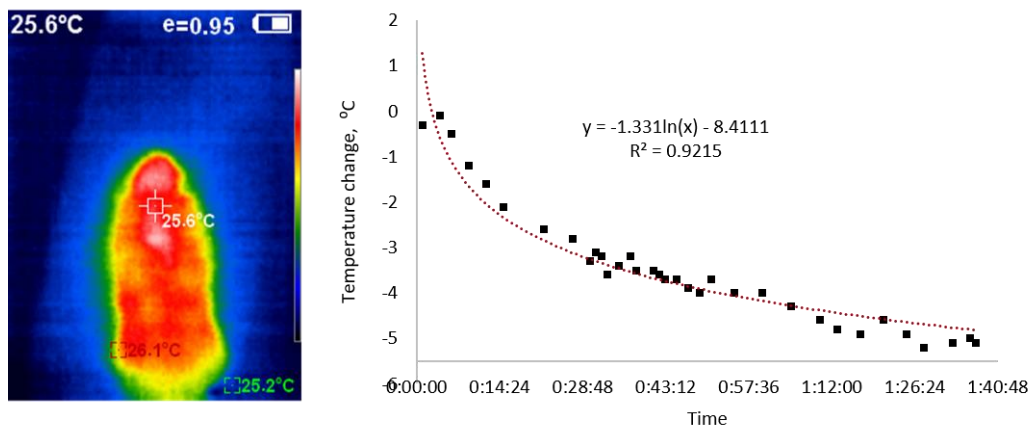


Figure 7-2 Surface measurement from IR thermal camera.

The measurement showed a steady decrease approaching room temperature in a few hours of anesthesia. The red line estimates the logarithmic trend.

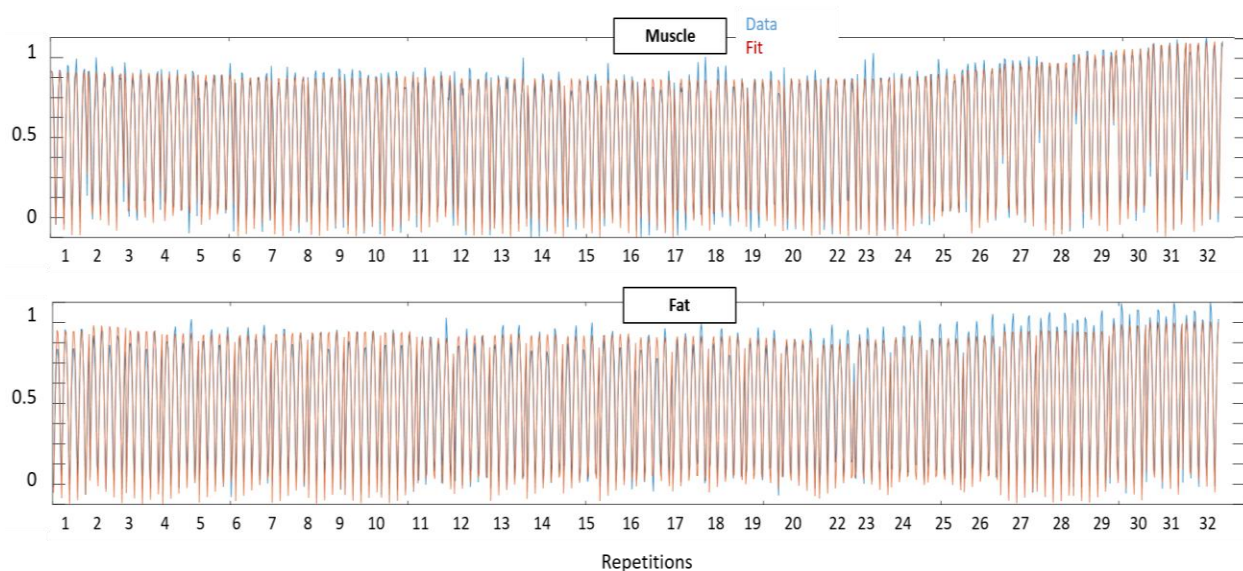


Figure 7-1 Example of binomial Z-spectra.

The spectra were consecutively repeated over time (blue) and fitted to the model function (red). Each repetition covers three sine cycles and reflects the magnetization oscillating over  $[-0.25, 0.25]$  ppm.

The temperature measurement in the mice ventral area showed a clear trend of the proton resonance frequency shift in the studied tissues. The sinusoidal fit faithfully predicted the behavior of the signal with a least square coefficient  $R^2 > 0.97$ . In the following figure, it is shown the fit overlaid to Z-spectra from pixels in muscular and fat tissue. Spectra are concatenated to the consecutive repetitions.

The first ZSI study without temperature control revealed an exponential thermal descent analogous to the one observed from the IR camera, albeit with different time constants.

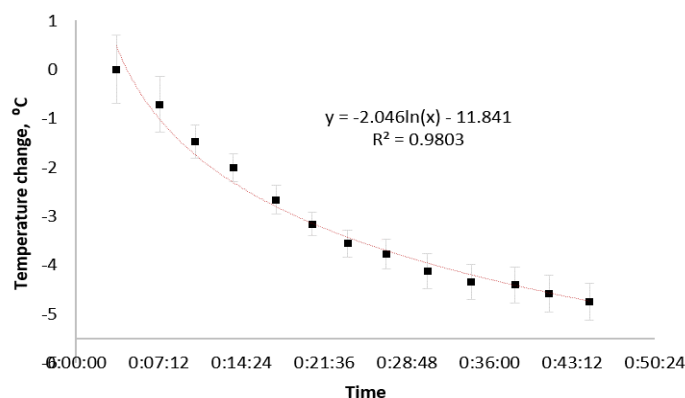


Figure 7-3 ZSI temperature over time.

Temporal evolution of temperature measurement from binomial ZSI in the muscles of a healthy mouse anesthetized with isoflurane. The red line estimates the logarithmic trend.

In the subsequent experiments, the temperature changes estimated by the binomial ZSI reflected the temporal and spatial distribution of the ones measured by the conventional GRE sequence.

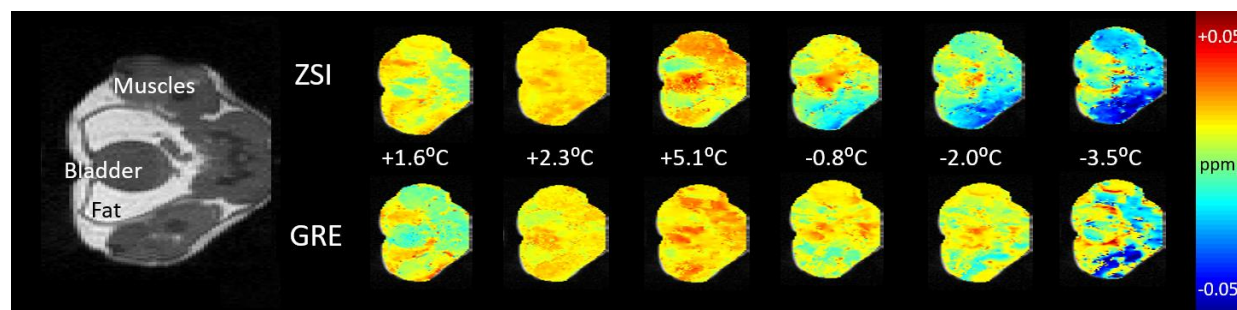


Figure 7-4 PRFS maps from first mouse.

Comparison of proton resonance frequency shift measured by binomial ZSI and multiecho GRE sequences for the first mouse undergoing thermal challenge. The body temperature measured by the rectal probe is indicated for each time point.

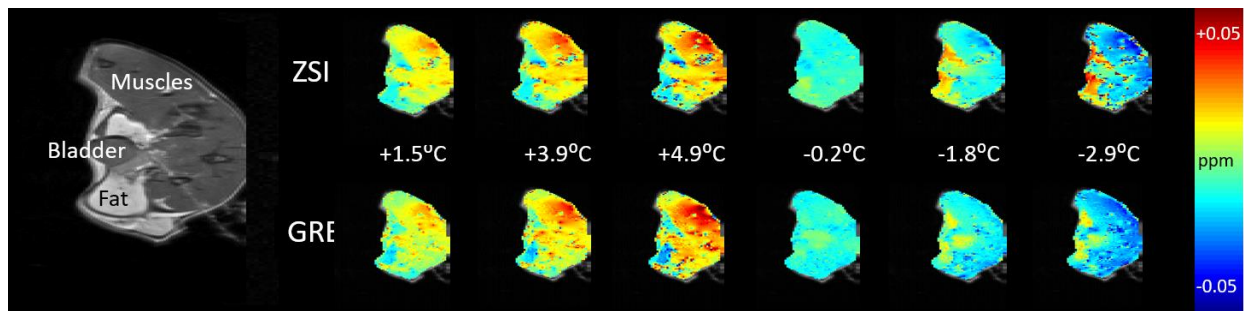


Figure 7-6 PRFS maps from the second mouse.  
Comparison of proton resonance frequency shift measured by binomial ZSI and multiecho GRE sequences for the second mouse undergoing thermal challenge.

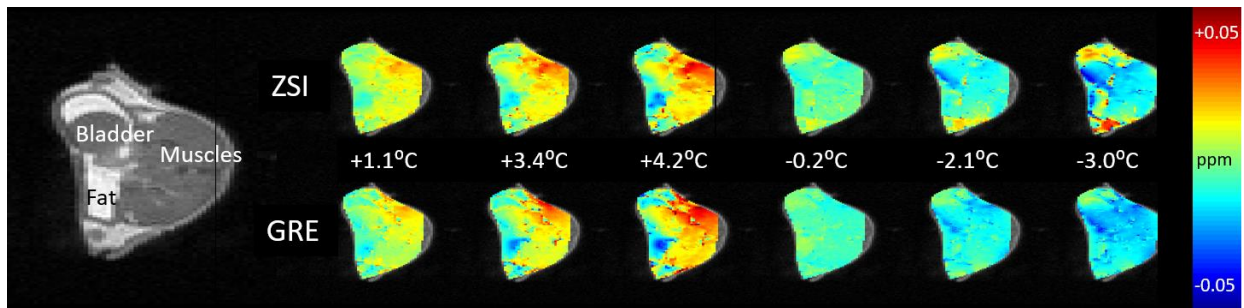


Figure 7-5 PRFS maps from the third mouse.  
Comparison of proton resonance frequency shift measured by binomial ZSI and multiecho GRE sequences for the third mouse undergoing thermal challenge.

The good agreement between the techniques qualitatively observed in the heatmaps was confirmed by the quantitative region of interest analysis.

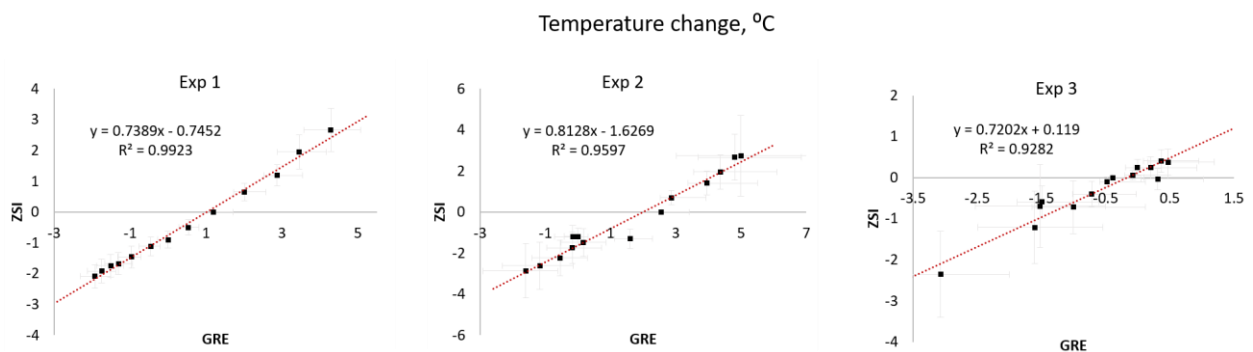


Figure 7-7 Correlations between GRE and ZSI.  
The temperature changes measured by the binomial ZSI and the phase difference from GREs correlated linearly in all studied mice.

In fact, in all three mice the correlation between the temperature measured in the muscle region by ZSI and the phase difference from the GRE was linearly correlated with  $R^2 > 0.92$ . In fat areas, despite the presence of trends, the comparison didn't produce consistent significant correlations.

In the experiment comparing ZSI to  $T_1$  mapping, it was instead found a good linear correlation between the techniques in both muscles and fat.

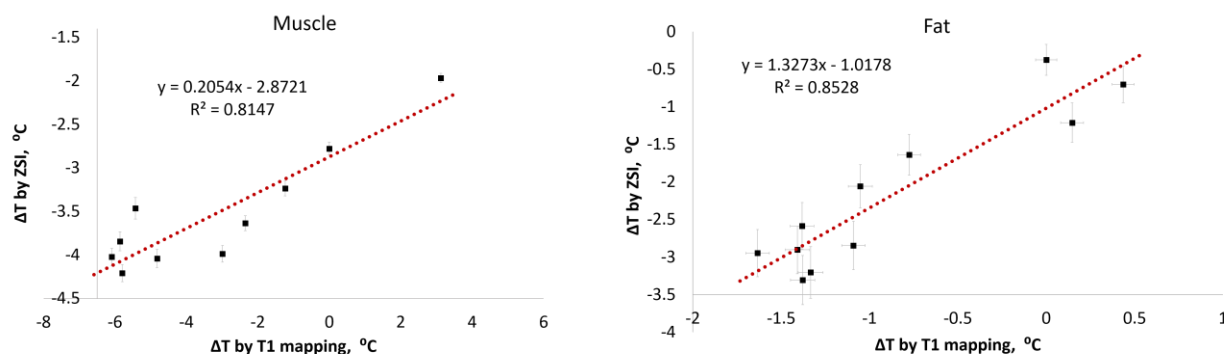


Figure 7-8 Comparison between ZSI and T1 mapping.

The temperature changes derived from the binomial ZSI and T1 mapping linearly correlated in both muscle and fat regions of interest.

## 7.4 Discussion

In this experiment, the feasibility of the binomial-ZSI as a noninvasive *in vivo* thermometry method was demonstrated. The technique allowed a measurement of the full field of view in less than three minutes and a signal to noise ratio on average  $>10$  per single image. The data presented as a sinusoidal function, as expected, and fitting was successfully performed by keeping a single varying parameter, which reflected the temperature change. The measurement detected changes  $<1^\circ\text{C}$  between consecutive measurements and was independent of  $B_0$  inhomogeneity. More importantly, the measurement was in agreement with the nominal temperature set for the air flow, measured in feedback through the rectal probe, with the

infrared surface measurement, with phase difference from GRE and with  $T_1$  changes in muscles as in fat tissues.

The technique was tested in the inguinal area of healthy mice, covering the upper thigh muscles and inguinal fat depots. This area was chosen because it is fairly distant from sources of motion like the lungs and the heart and artifacts are therefore minimized, while at the same time being close to the temperature rectal probe.

In the first experiment, the temperature decreased exponentially as the mouse body acclimated to the laboratory temperature under anesthesia. The measurement from the binomial ZSI reflected the one from the IR camera, reproducing the decay over time. It is worth noting that the experiment was carried out on different mice and that the starting temperature in the two measurements was necessarily different (29°C vs 25°C, due to the longer time under anesthesia during the MRI setup). At a qualitative level, nevertheless, this result provided a first validation of the ZSI technique. A second outcome can also be deduced from this experiment. It is known that intensive use of rapidly switching gradients can overheat the scanner and ultimately lead to a shift in the central proton resonance (13). The purely exponential decay observed in this simple experiment points to a single contribution to the frequency shift, namely the temperature-induced effect, rather than the linear drift due to scanner setup degrading.

In the thermal challenge experiments, it was possible to produce heatmaps of frequency shift distribution, independent of field inhomogeneity assessed by  $B_0$  maps. It is possible to notice a spatial variability of water resonance shift in the ZSI-derived heatmaps. This variability is likely caused by the different level of exposure to the air flow due to the mouse position on the holder. Such variability cannot be captured by the measurement performed with the rectal probe, at a single point source and in a specific physical compartment, measuring the core temperature. This observation simply reiterates the need for a thermometric method with large coverage and high resolution capability. The colormaps derived from the multiecho serve therefore as a more apt comparison in our study. In fact, the variability observed on the

ZSI colormaps was confirmed by the GRE maps. On a more quantitative level, the correlation analysis demonstrated that the average values in the muscle region were in high agreement between the two techniques.

It is interesting to note that the same analysis in other areas failed to produce consistent significant correlations. Only one out of three mice had a correlation with  $R^2 > 0.7$  in the bladder, and none in the fat tissue. While the lack of consistency in the bladder might be due to field inhomogeneity and various spectral components corrupting the signal, the results in fat are likely due to a more complex mechanism. Both ZSI and phase difference rely on the proton resonance frequency shift effect, which depends on the decreased electronic shielding around the nuclei, stretched under higher temperature. While the measurement is perfectly evident in watery tissues, it is commonly assumed that fat protons shouldn't be significantly affected, since the shielding constant in lipids is an order of magnitude lower compared to water:  $\sigma_F = 0.002$ , vs  $\sigma_W = 0.01$  per degree Celsius (14). Nevertheless, we sometimes observed frequency shifts inside the fat tissues. This effect in turn can be due to either the scanner central frequency drifting under the intensive gradient switching during fast sequences, or to changes in the temperature-dependent susceptibility, which is described by a constant of the same magnitude of  $\sigma_W$ . Since we didn't observe the same steady  $B_0$  drift in other areas of the field of view, we can conclude that the shift has to be due to susceptibility, as it has been suggested before (15). It is possible that the different sensitivity to this effect translates in the GRE and the ZSI methods recording different frequency shifts, sometimes with inverted polarity. The measurement through the  $T_1$  mapping method can thus serve as an alternative reference for the study in fat tissue. The linearity found in the correlation with temperature as measured from the binomial ZSI, confirmed the reliability of this technique in both muscular and fatty tissue. It can therefore be concluded that this study validated the binomial-ZSI as a reliable method to measure temperature changes *in vivo*.

The ultimate goal of this project would be the implementation of this technique in clinics. The binomial-ZSI technique has been developed in a preclinical environment, at a high field animal scanner. In a translational perspective, the use of a lower field will likely reduce the temperature sensitivity as the spectral resolution will decrease. While we expect that optimization of the delay time and pulses width will still deliver a sensitivity  $<1^{\circ}\text{C}$ , it will be advisable to implement more sophisticated designs for the preparatory pulse segment. Furthermore, the application of the ZSI technique for the study of brown adipose tissue in clinics will face the sparse nature of the depots in humans. In order to accurately assess the local temperature changes, it will be necessary to acquire the sequence at high spatial resolution, or to adopt reduced field of view strategies (16), provided the excitation scheme doesn't interfere with the preparatory module.

In conclusion, this chapter served as the demonstration that the binomial-ZSI technique can reliably measure temperature changes *in vivo*, paving the path for its application in the study of brown and browning adipose tissue.

## 7.5 Summary

In this chapter, the feasibility of the binomial-ZSI technique implementation *in vivo* has been demonstrated. The protocol was tested in healthy mice undergoing thermal challenge under anesthesia. Hind legs muscles and inguinal fat depots were imaged. Binomial-ZSI provided a reliable measurement of the temperature change across the field of view with high resolution and high sensitivity. Results were in agreement with the nominal temperature set on the scanner bore and with the temperature measured by conventional magnetic resonance methods in both muscle and fat tissues.

## Bibliography

1. Odéen H, Parker D. Magnetic Resonance Thermometry and Its Biological Applications - Physical Principles and Practical Considerations. *Prog Nucl Magn Reson Spectrosc*. 2019 Feb;110:34-61. doi: 10.1016/j.pnmrs.2019.01.003. Epub 2019 Jan 31.
2. Cypess, A.M., et al., Brown Fat in Humans: Consensus Points and Experimental Guidelines. *Cell Metab*, 2015. **20**: p. 408-415.
3. Hu HH, Branca RT, Hernando D, Karampinos DC, Machann J, McKenzie CA, Wu HH, Yokoo T, Velan SS. Magnetic resonance imaging of obesity and metabolic disorders: Summary from the 2019 ISMRM Workshop. *Magn Reson Med*. 2020 May;83(5):1565-1576. doi: 10.1002/mrm.28103. Epub 2019 Nov 29. PMID: 31782551.
4. Wu M, Junker D, Branca RT, Karampinos DC. Magnetic Resonance Imaging Techniques for Brown Adipose Tissue Detection. *Front Endocrinol (Lausanne)*. 2020 Aug 7;11:421. doi: 10.3389/fendo.2020.00421. PMID: 32849257; PMCID: PMC7426399.
5. Sun L, Verma S, Michael N, Chan SP, Yan J, Sadananthan SA, Camps SG, Goh HJ, Govindharajulu P, Totman J, Townsend D, Goh JP, Sun L, Boehm BO, Lim SC, Sze SK, Henry CJ, Hu HH, Velan SS, Leow MK. Brown Adipose Tissue: Multimodality Evaluation by PET, MRI, Infrared Thermography, and Whole-Body Calorimetry (TACTICAL-II). *Obesity (Silver Spring)*. 2019 Sep;27(9):1434-1442. doi: 10.1002/oby.22560. Epub 2019 Jul 13. PMID: 31301122; PMCID: PMC6899540.
6. Hamaoka T, Nirengi S, Fuse S, Amagasa S, Kime R, Kuroiwa M, Endo T, Sakane N, Matsushita M, Saito M, Yoneshiro T, Kurosawa Y. Near-Infrared Time-Resolved Spectroscopy for Assessing Brown Adipose Tissue Density in Humans: A Review. *Front Endocrinol (Lausanne)*. 2020 May 19;11:261. doi: 10.3389/fendo.2020.00261. PMID: 32508746; PMCID: PMC7249345.
7. Law J, Chalmers J, Morris DE, Robinson L, Budge H, Symonds ME. The use of infrared thermography in the measurement and characterization of brown adipose tissue activation. *Temperature (Austin)*. 2018 Jan 29;5(2):147-161. doi: 10.1080/23328940.2017.1397085. PMID: 30393752; PMCID: PMC6209420.
8. Kokuryo D, Kumamoto E, Kuroda K. Recent technological advancements in thermometry. *Adv Drug Deliv Rev*. 2020;163-164:19-39. doi: 10.1016/j.addr.2020.11.001. Epub 2020 Nov 18. PMID: 33217482.

9. Winter L, Oberacker E, Paul K, Ji Y, Oezerdem C, Ghadjar P, Thieme A, Budach V, Wust P, Niendorf T. Magnetic resonance thermometry: Methodology, pitfalls and practical solutions. *Int J Hyperthermia*. 2016;32(1):63-75. doi: 10.3109/02656736.2015.1108462. Epub 2015 Dec 27. PMID: 26708630.
10. Rieke V, Butts Pauly K. MR thermometry. *J Magn Reson Imaging*. 2008 Feb;27(2):376-90. doi: 10.1002/jmri.21265. PMID: 18219673; PMCID: PMC2780364.
11. Ohlson KB, Lindahl SG, Cannon B, Nedergaard J. Thermogenesis inhibition in brown adipocytes is a specific property of volatile anesthetics. *Anesthesiology*. 2003 Feb;98(2):437-48. doi: 10.1097/00000542-200302000-00025. PMID: 12552204.
12. Ohlson KB, Mohell N, Cannon B, Lindahl SG, Nedergaard J. Thermogenesis in brown adipocytes is inhibited by volatile anesthetic agents. A factor contributing to hypothermia in infants? *Anesthesiology*. 1994 Jul;81(1):176-83. doi: 10.1097/00000542-199407000-00024. PMID: 8042786.
13. Foerster BU, Tomasi D, Caparelli EC. Magnetic field shift due to mechanical vibration in functional magnetic resonance imaging. *Magn Reson Med* 2005; 54: 1261- 7.
14. Poorter, J.D., *Noninvasive MRI Thermometry with the Proton Resonance Frequency Method: Study of Susceptibility Effects*. *MRM*, 1995. **34**: p. 359-367.
15. Sprinkhuizen SM, Konings MK, van der Bom MJ, Viergever MA, Bakker CJ, Bartels LW. Temperature-induced tissue susceptibility changes lead to significant temperature errors in PRFS-based MR thermometry during thermal interventions. *Magn Reson Med*. (2010) 64:1360–72. doi: 10.1002/mrm.22531
16. Finsterbusch J. Improving the performance of diffusion-weighted inner field-of-view echo-planar imaging based on 2D-selective radiofrequency excitations by tilting the excitation plane. *J Magn Reson Imaging*. 2012 Apr;35(4):984-92. doi: 10.1002/jmri.23522. Epub 2011 Dec 14. PMID: 22170770.

## 8. CONCLUSION

### 8.1 Summary

Brown adipose tissue is one of the brightest hopes in the fight against the obesity epidemic. Key to the understanding and management of BAT is the establishment of a noninvasive imaging method to unbiasedly detect and monitor brown and browning adipose tissue. The current imaging approaches are either invasive or lack a comprehensive capability to assess the structural and functional aspects of the tissue. Z-Spectrum MR Imaging can bridge this gap. In this dissertation, it is presented how ZSI can produce both structural and functional contrasts, which can be used to study brown and browning adipose tissue.

In the first step it has been shown how ZSI can measure fat water fraction to detect BAT. The technique consists in a series of images acquired after saturating the protons resonating over a range of frequency offsets. The largest dips in signal reflect the direct saturation of water and fat protons. By fitting the Z-spectrum it is possible to extract the relative contribution to the overall signal, summarized in the fat water fraction. The novel FWF metric was calibrated with an oil and water mixture phantom and validated in specimens, mice and human subjects. FWF distribution was compared to published work and values compared to Dixon's MRI results. ZSI clearly differentiated WAT, BAT, and lean tissues by having  $\text{FWF}=1$ ,  $0.5$  and  $0$  respectively. FWF maps of human subjects showed the same FWF distribution as Dixon's MRI, but showed no fat-water swapping artifact in regions of high field inhomogeneity. The technique was then tested on a clinical problem. In fact, it has been reported that polycystic ovary syndrome (PCOS) patients might have reduced BAT functionality. We therefore used ZSI to characterize brown adipose tissue in PCOS compared to healthy subjects. Spectral data were collected at a 3T and a histogram analysis of the FWF distribution in the supraclavicular area was used to derive the fraction of BAT over the total fat depot ( $\text{BATf}$ ) and the average FWF in BAT ( $\text{FWF}(\text{BAT})$ ). The parameters were compared among the male, female patients and the female healthy group, and the correlations to Body

Mass Index were also quantified. In summary, subjects with higher BMI showed less BATf and increased FWF(BAT), indicating relatively higher level of metabolic passive WAT depots and relatively reduced metabolism correlating with BMI. As for the disease, PCOS patients showed the smallest BATf and the highest FWF(BAT) among the groups, suggesting decreased BAT involvement in PCOS. This result show that ZSI can be of use to monitor treatment responses of PCOS therapies.

Next, this dissertation proceeded to demonstrate the efficacy of Z-spectrum MRI in detecting adipose tissue activation through changes in FWF. Detection of brown and white adipose tissue activation are of particular interest due to their benefits against obesity and metabolic disorders. Here a transgenic mouse model, TripBr2-KO, was treated with an adrenergic drug to stimulate fat activation. Mice were studied for two weeks by ZSI and compared to saline-treated wild types. Results showed that FWF was significantly lower over time in the treated group compared to the controls, suggesting that lipid consumption, associated with adipose tissue activation, has occurred. The successful detection, confirmed by a reduction in the depot size, was found both in perirenal brown fat and in subcutaneous white fat, albeit following different temporal patterns, reflective of the different activation potential of the depots.

After showing the potential of the FWF biomarker in characterizing BAT mass and function, it was the aim in this thesis to use to ZSI to produce a marker of BAT very own thermogenesis. Here was then proposed a new sequence based on the ZSI platform, where the preparatory RF saturation pulse is substituted by a binomial pulse, the Jump-Return. The effect of the paired hard pulses is to refocus the saturated magnetization partially as a function of chemical shift. The resulting signal oscillates as a sine function of the offset. When the temperature changes, the proton resonance frequency shift effect (PRFS) assures a shift of the entire curve. The proof of concept was carried out in PBS solution exposed to hot air flow. Then, the technique was tested on a whipped cream phantom, used as a proxy for biological fatty tissue. The temperature measurement was successful and correlated well with the one

form the electrode sensor probe inserted in the phantom. Being independent on phase artifacts and capable of fine thermal sensitivity, the technique is ideal for the study of thermogenesis.

Finally, the feasibility of the binomial-ZSI technique implementation in vivo was assessed. The protocol was tested in healthy mice undergoing thermal challenge under anesthesia. Hind legs muscles and inguinal fat depots were imaged. Binomial-ZSI provided a reliable measurement of the temperature change across the field of view with high resolution and high sensitivity. Results were in agreement with the nominal temperature set on the scanner bore and with the temperature measured in muscles by standard MRI methods, in both muscle and fat.

These studies, taken together, show how Z-spectrum Imaging is capable of producing varied structural and functional contrasts that can be used to comprehensibly characterize brown and browning adipose tissue.

## 8.2 Contributions to the field

The 2019 Workshop on obesity and metabolic disorder from the International Society of Magnetic Resonance Imaging redacted a summary that highlights the most urgent needs in the field. Among these, it reads: “The integrated understanding of the BAT physiology and its therapeutic role in metabolic disorders and obesity remains largely unanswered.” The outcome of this dissertation goes precisely in this direction: to provide a novel imaging method that produces metabolic and structural contrasts, for a comprehensive adipose tissue characterization. Current techniques, in fact, are either invasive or lack the capacity to observe both the structure and the thermogenic function of the adipose organ. Here it was shown that Z-Spectrum Imaging not only can measure fat water fraction and differentiate BAT from WAT, but can also assess thermal changes that can reflect thermogenesis. Despite the enthusiasm that captured the scientific community when active BAT in humans was re-discovered now a decade ago, development

in therapies to exploit the tissue have stagnated. One culprit is surely the lack of a reliable evaluation method for such therapies. On the long term, therefore, ZSI can be used to monitor the impact of pharmacological treatments of obesity and metabolic disease, their efficacy duration and the need for repeated dosage or stimulation, in summary providing a comprehensive screening tool for the treatment. A few results can also have a more immediate impact. The development of an alternative method to chemical shift encoded (Dixon) MRI to measure fat content can expand the number of accessible tissues. The innate resistance of Z-spectrum imaging to field inhomogeneity and phase errors can allow measurement in iron-loaded organs and other heterogeneous boundary areas, like the bone marrow in the spinal cord. Moreover, the temperature measurement based on the binomial-ZSI showed great results in fatty tissues, where current imaging is limited mainly to  $T_1$  relaxation, which requires calibration for each tissue under study. The possibility to modulate the excitation profile and the thermal sensitivity through the sequence parameters and delays, further highlights the potential of the Z-spectrum Imaging technique.

### 8.3 Future works

In this dissertation it was demonstrated the ability of Z-spectrum MR Imaging to produce structural and functional contrast, useful to assess the status of metabolic adipose tissue. The proof of concept, validation through phantoms, *ex-vivo* tissues, *in vivo* experiments and the comparison to standard clinical techniques were all successfully completed and partly published.

Several avenues are now open and the present study requires optimization in order to be translated to clinical research.

The application of ZSI to characterize brown adipose tissue in PCOS patients was fully conducted and published. With more subjects to be recruited for future studies, particularly healthy females with large

BMI, it will be possible to perform BMI-matched comparison between PCOS and healthy subjects to better control for any bodyweight-induced confounding factors

The study of activation in the visceral area through changes in fat-water fraction was completed, presented as abstract and a manuscript is being drafted. Since it has been reported that visceral fat is generally resistant to standard stimulation, further studies with larger sample size (~10/group) and a solid pathological validation of the ZSI findings (in particular by staining for the thermogenic protein UCP1) will be carried out. In addition, by stimulating the mice over time, it will also be possible to assess if activation is maintained in all depots or if it is transient, indicating areas potentially resistant to the browning treatment.

The work on the development of the temperature sensitive ZSI has been presented as abstract and a paper is being drafted. In the next step, a fitting model from the Bloch-McConnell equations, thus taking into account possible variations in relaxation times and pools fraction, will also be designed. The technique will then delve in measuring BAT thermogenesis directly, first in mice anesthetized with pentobarbital and stimulated through adrenergic drug, and then in human volunteers undergoing a cold challenge. Besides measuring temperature deltas, the comprehensive ZSI measurement will inform about the relationship between adipose tissue mass and function. We expect that WAT areas identified through FWF will have negligible or little temperature increase. We expect to see a general correlation between BAT area identified by FWF and thermogenic area. However, subtle activation variability within the depot has been reported and we therefore expect to image such intradepot distribution. With high spatial and thermal resolution, ZSI will provide quantitative, subject-specific measurements, ideal for the monitoring of obesity treatments.

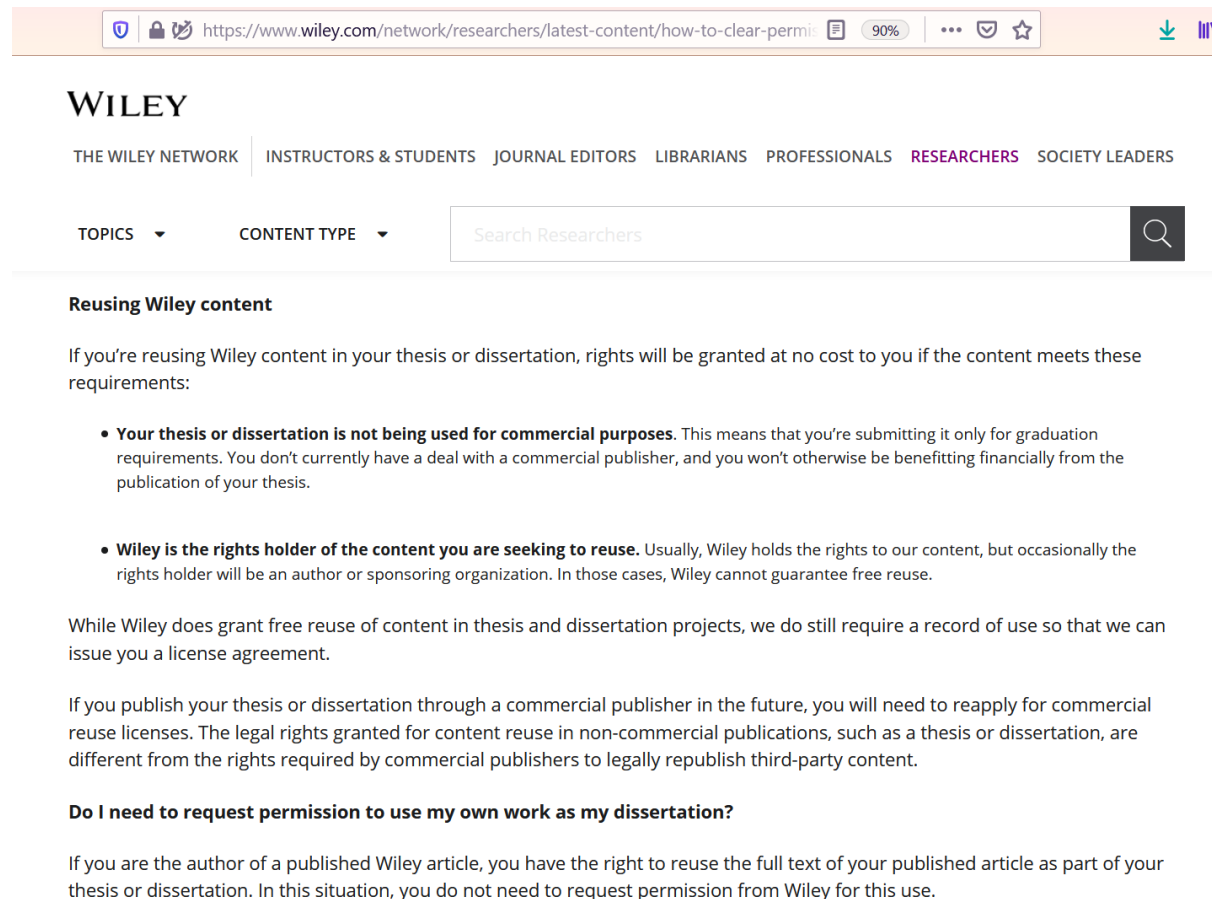
## APPENDIX

The permission to reproduce copyrighted results was granted by the publishers in the case of inclusion of the said results in academic dissertations.

For the work reproduced in Chapter 3, see permission description at:

<https://www.wiley.com/network/researchers/latest-content/how-to-clear-permissions-for-a-thesis-or-dissertation>

Of which the pertaining extract states as follows:



The screenshot shows the Wiley website's 'Reusing Wiley content' page. At the top, the Wiley logo is followed by navigation links: THE WILEY NETWORK, INSTRUCTORS & STUDENTS, JOURNAL EDITORS, LIBRARIANS, PROFESSIONALS, RESEARCHERS (highlighted in pink), and SOCIETY LEADERS. Below these are filters for TOPICS and CONTENT TYPE, and a search bar labeled 'Search Researchers'. The main heading is 'Reusing Wiley content'. The text explains that if you're reusing Wiley content in your thesis or dissertation, rights will be granted at no cost if the content meets two requirements:

- **Your thesis or dissertation is not being used for commercial purposes.** This means that you're submitting it only for graduation requirements. You don't currently have a deal with a commercial publisher, and you won't otherwise be benefitting financially from the publication of your thesis.
- **Wiley is the rights holder of the content you are seeking to reuse.** Usually, Wiley holds the rights to our content, but occasionally the rights holder will be an author or sponsoring organization. In those cases, Wiley cannot guarantee free reuse.

While Wiley does grant free reuse of content in thesis and dissertation projects, we do still require a record of use so that we can issue you a license agreement.

If you publish your thesis or dissertation through a commercial publisher in the future, you will need to reapply for commercial reuse licenses. The legal rights granted for content reuse in non-commercial publications, such as a thesis or dissertation, are different from the rights required by commercial publishers to legally republish third-party content.

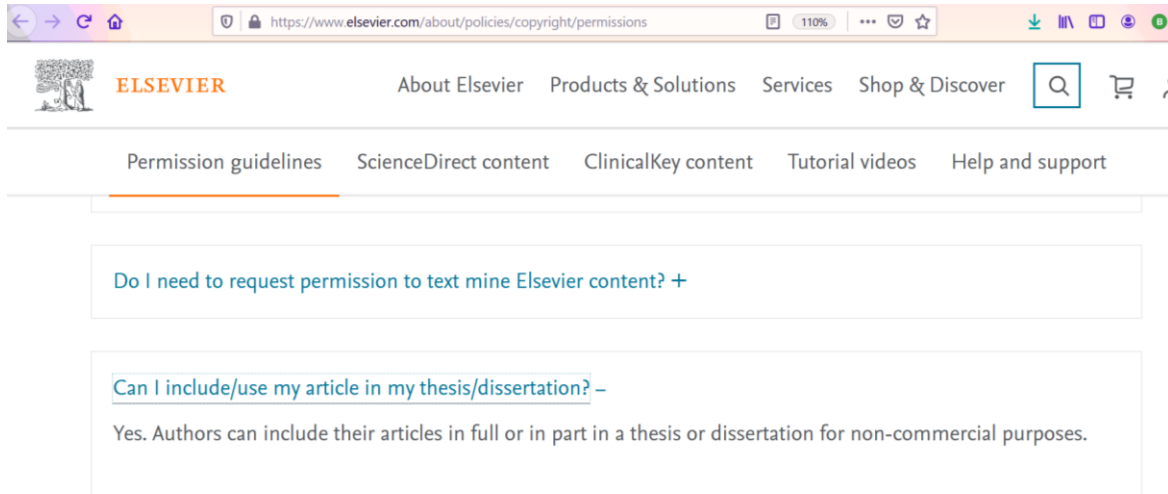
**Do I need to request permission to use my own work as my dissertation?**

If you are the author of a published Wiley article, you have the right to reuse the full text of your published article as part of your thesis or dissertation. In this situation, you do not need to request permission from Wiley for this use.

For the work reproduced in Chapter 4, see:

<https://www.elsevier.com/about/policies/copyright/permissions>

And the pertaining excerpt:



The screenshot shows the Elsevier website's copyright/permissions page. The browser address bar displays the URL <https://www.elsevier.com/about/policies/copyright/permissions>. The page features the Elsevier logo and a navigation menu with links to "About Elsevier", "Products & Solutions", "Services", and "Shop & Discover". A search bar and a shopping cart icon are also present. Below the navigation menu, a horizontal bar contains links to "Permission guidelines", "ScienceDirect content", "ClinicalKey content", "Tutorial videos", and "Help and support". The "Permission guidelines" link is highlighted with an orange underline. The main content area contains two expandable sections. The first section, titled "Do I need to request permission to text mine Elsevier content? +", is currently collapsed. The second section, titled "Can I include/use my article in my thesis/dissertation? –", is expanded, revealing the text: "Yes. Authors can include their articles in full or in part in a thesis or dissertation for non-commercial purposes."

## VITA

### EDUCATION

Ph.D. in Bioengineering, March 2021

*Department of Bioengineering, University of Illinois at Chicago, Chicago, IL*

Dissertation: "A Novel Z-Spectrum MRI for the detection of brown and browning adipose tissue"

Advisor: Professor Kejia Cai

M.S. in Medical Physics, Feb 2012

*Department of Physics, University of Milan, Italy*

Dissertation: "Perfusion MRI for the verification of the effectiveness of an antitumor vaccine in GBM patients".

Advisor: Eng. Domenico Aquino

### WORKING EXPERIENCE

2015-2021; Research Assistant

*Cai Lab, Radiology Department, University of Illinois at Chicago, Chicago, IL*

2014-2015; Research Staff

*4D Lab, Radiology Department, Northwestern University, Chicago, IL*

2012-2014; Research Staff

*High Field MRI, Radiology Department, Neurological Institute "C. Besta", Milan, Italy*

### TEACHING EXPERIENCE

2018-2019; Teaching Assistant, BioE 102: Seminar Presentation Training

*University of Illinois at Chicago, Chicago, IL*

2013-2014; Master Class to Certified Radiology Techs: Perfusion MRI

*"Careggi" University-Hospital, Florence, Italy*

## AWARDS and SCHOLARSHIPS

ISMRM Educational Stipend Award – 2015, 2016, 2017, 2019

50% Graduate Research Assistantship; College of Medicine, UIC, 2015-2021

First Place, College of Medicine UIC CCTS Multidisciplinary Science Award, 2016

First Place, Poster Competition, Neurological Institute “C. Besta”, 2013

## JOURNAL PUBLICATIONS

(In bold the works published during the PhD)

1. **Combination of NK-based immunotherapy and sorafenib against hepatocellular carcinoma. Yang J, Eresen A, Scotti A, Cai K, Zhang Z. Am J Cancer Res. 2021 Feb 1;11(2):337-349. eCollection 2021.**
2. **Characterization of microenvironmental changes in the intervertebral discs of patients with chronic low back pain using multiparametric MRI contrasts extracted from Z-spectrum. Li L, Zhou Z, Xiong W, Fang J, Scotti A, Shaghaghi M, Zhu W, Cai K. Eur Spine J. 2021 Jan 21. Epub ahead of print.**
3. **Multimodal apparent diffusion (MAD) weighted magnetic resonance imaging. Damen FC, Scotti A, Damen FW, Saran N, Valyi-Nagy T, Vukelich M, Cai K. Magn Reson Imaging. 2020 Dec 10;77:213-233. Epub ahead of print.**
4. **Characterization of brown adipose tissue (BAT) in polycystic ovary syndrome (PCOS) patients by Z-Spectral Imaging (ZSI). Li L, Scotti A, Fang J, Yin L, Xiong T, He W, Qin Y, Liew C, Khayyat N, Zhu W, Cai K. Eur J Radiol. 2020 Feb;123:108777. Epub 2019 Dec 11.**
5. ***In vivo* quantification of proton exchange rate in healthy human brains with omega plot. Shaghaghi M, Chen W, Scotti A, Ye H, Zhang Y, Zhu W, Cai K. Quant Imaging Med Surg. 2019 Aug. Epub 2019 Nov.**
6. **Characterization of the microstructure of the intervertebral disc in patients with chronic low back pain by diffusion kurtosis imaging. Li L, Zhou Z, Xiong W, Fang J, Li Y, Jiao Z, Scotti A, Li F, Zhu W, Cai K. Eur Spine J. 2019 Aug 13. Epub 2019 Nov.**

7. Diffusion kurtosis imaging provides quantitative assessment of the microstructure changes of disc degeneration: an in vivo experimental study. Li L, Zhou Z, Li J, Fang J, Qing Y, Tian T, Zhang S, Wu G, Scotti A, Cai K, Zhu W. *Eur Spine J*. 2019 May;28(5):1005-1013. Epub 2019 Feb 18.
8. Improving the detection specificity of endogenous MRI for reactive oxygen species (ROS). Tain RW, Scotti AM, Cai K. *J Magn Reson Imaging*. 2019 Aug;50(2):583-591. doi: 10.1002/jmri.26629. Epub 2019 Jan 7. PMID: 30614137
9. Non-invasive Imaging Methods for Brown Adipose Tissue Detection and Function Evaluation. Zhang Y, Hu X, Hu S, Scotti A, Cai K, Wang J, Zhou X, Yang D, Figini M, Pan L, Shangguan J, Yang J, Zhang Z. *Intern Med Open Access*. 2018;8(6). pii: 299. Epub 2019 Jan 7.
10. Mapping brown adipose tissue based on fat water fraction provided by Z-spectral Imaging. Scotti A, Tain RW, Li W, Gil V, Liew CW, Cai K. *J Magn Reson Imaging*. 2018 Jun; 47(6):1527-1533.
11. Imaging short-lived reactive oxygen species (ROS) with endogenous contrast MRI. Tain RW, Scotti AM, Li W, Zhou XJ, Cai K. *J Magn Reson Imaging*. 2018 Jan; 47(1):222-229. Epub 2017 May 15.
12. Creatine CEST MRI for Differentiating Gliomas with Different Degrees of Aggressiveness. Cai K, Tain RW, Zhou XJ, Damen FC, Scotti AM, Hariharan H, Poptani H, Reddy R. *Mol Imaging Biol*. 2017 Apr; 19(2):225-232.
13. Influence of Free Radicals on the Intrinsic MRI Relaxation Properties. Tain RW, Scotti AM, Li W, Zhou XJ, Cai K. *Adv Exp Med Biol*. 2017; 977:73-79.
14. A longitudinal DTI and histological study of the spinal cord reveals early pathological alterations in G93A-SOD1 mouse model of amyotrophic lateral sclerosis. Marcuzzo S, Bonanno S, Figini M, Scotti A, Zucca I, Minati L, Riva N, Domi T, Fossaghi A, Quattrini A, Galbardi B, D'Alessandro S, Bruzzone MG, García-Verdugo JM, Moreno-Manzano V, Mantegazza R, Bernasconi P. *Exp Neurol*. 2017 Jul; 293:43-52. Epub 2017 Mar 27.
15. Comparison of Diffusion MRI Acquisition Protocols for the In Vivo Characterization of the Mouse Spinal Cord: Variability Analysis and Application to an Amyotrophic Lateral Sclerosis Model. Figini M, Scotti A, Marcuzzo S, Bonanno S, Padelli F, Moreno-Manzano V, García-Verdugo JM,

Bernasconi P, Mantegazza R, Bruzzone MG, Zucca I. PLoS One. 2016 Aug 25; 11(8):e0161646. eCollection 2016.

16. Comprehensive evaluation of aortic disease by in-vivo 4D flow MRI and 3D printing of patient-specific models: a feasibility study. Ahmadian RR, Boyd AP, Scotti A, Collins JD, Carr JC, McCarthy P, Malaisrie SC, Barker A, Markl M. J Cardiovasc Magn Reson. 2016; 18(Suppl 1): P365.
17. Head and Neck Veins of the Mouse. A Magnetic Resonance, Micro Computed Tomography and High Frequency Color Doppler Ultrasound Study. Mancini M, Greco A, Tedeschi E, Palma G, Ragucci M, Bruzzone MG, Coda AR, Torino E, Scotti A, Zucca I, Salvatore M. PLoS One. 2015 Jun 11;10(6):e0129912. doi: 10.1371/journal.pone.0129912. PMID: 26067061; PMCID: PMC4466257.
18. 7T MRI features in control human hippocampus and hippocampal sclerosis: an ex vivo study with histologic correlations. Coras R, Milesi G, Zucca I, Mastropietro A, Scotti A, Figini M, Mühlebner A, Hess A, Graf W, Tringali G, Blümcke I, Villani F, Didato G, Frassoni C, Spreafico R, Garbelli R. Epilepsia. 2014 Dec; 55(12):2003-16. Epub 2014 Nov 3.
19. Potential use of human adipose mesenchymal stromal cells for intervertebral disc regeneration: a preliminary study on biglycan-deficient murine model of chronic disc degeneration. Marfia G, Campanella R, Navone SE, Zucca I, Scotti A, Figini M, Di Vito C, Alessandri G, Riboni L, Parati E. Arthritis Res Ther. 2014 Oct 8;16(5):457. doi: 10.1186/s13075-014-0457-5. PMID: 25293819; PMCID: PMC4223513.
20. Parametric response maps of perfusion MRI may identify recurrent glioblastomas responsive to bevacizumab and irinotecan. Aquino D, Di Stefano AL, Scotti A, Cuppini L, Anghileri E, Finocchiaro G, Bruzzone MG, Eoli M. PLoS One. 2014 Mar 27; 9(3):e90535. eCollection 2014.
21. Gold nanoparticles protected by fluorinated ligands for <sup>19</sup>F MRI. Boccalon M, Franchi P, Lucarini M, Delgado JJ, Sousa F, Stellacci F, Zucca I, Scotti A, Spreafico R, Pengo P, Pasquato L. Chem Commun (Camb). 2013 Oct 9;49(78):8794-6. doi: 10.1039/c3cc44572k. PMID: 23959517.